UNIVERSITÀ DEGLI STUDI DI PADOVA

DIPARTIMENTO DI SCIENZE CHIMICHE

DOTTORATO DI RICERCA IN SCIENZE MOLECOLARI INDIRIZZO SCIENZE CHIMICHE

CICLO XXVI

STRATEGIES FOR THE MODULATION OF CATALYTIC ACTIVITY OF Zn(II)-BASED ARTIFICIAL NUCLEASES

Coordinatore: Ch.mo Prof. Antonino Polimeno

Supervisore: Ch.mo Prof. Paolo Scrimin

Dottoranda: Marta Diez Castellnou

A mis padres

“Caminante no hay camino,

se hace camino al andar”

Antonio Machado

Table of Context

Chapter 3: Efficient phosphodiester cleaving nanozymes

Chapter 4: Mixed-monolayer nanozymes

Bibliography

Abstract

In the present thesis, entitled “Strategies for the modulation of catalytic activity of Zn(II)-based of artificial nucleases”, the results obtained in an extensive investigation on the reactivity of different catalytic systems for hydrolytic cleavage of phosphate diesters are reported.

Phosphate diesters have a remarkable importance since they constituted the backbone of essential biomolecules as DNA and RNA. Indeed, the high stability of those polianions towards the hydrolytic attack is due to the presence of the phosphodiester group. On the other hand, the hydrolytic cleavage of nucleic acids occurs in living organism is few milliseconds, thanks to nucleases which are the enzyme devoted to this task.

In the attempt to reproduce the activity of such enzymes, which are among the most efficient present in nature, I focused my attention on the design and synthesis of catalytic agents based on metal ions, namely Zn(II) ions, and studying their reactivity towards a RNA model, the 2-hydroxypropyl-*para*-nitrophenyl phosphate (HPNP).

In the first part of the thesis, the interesting results I obtained in the study of the reactivity of monometallic Zn(II)-based complexes towards HPNP are reported. The Zn(II) complexes used in this studied were **1** (mononuclear complex of 1,4,7-triazacyclononane, TACN) and **2,** (mononuclear complex of 1,4,7-trimethyl-1,4,7-triazacyclononane, TMTACN) which is the corresponding permethylated derivative.

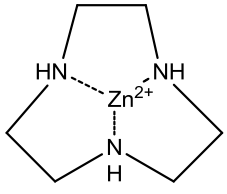

Complex 1. Zn(II)-TACN

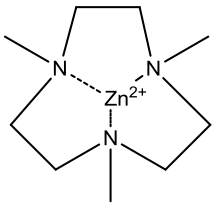

Complex 2. Zn(II)-TMTACN

I will show how the small differences in the structure of the two ligands affect the HPNP cleavage reaction with effects never reported before. The hypothesis that such differences may arise from different coordination geometries of the metal will be discussed.

The second part of the thesis is focused on the investigation of the effects that the local environment surrounding the metal complexes produces on their reactivity towards phosphodiester cleavage. In this view, I designed supramolecular systems based on functionalized gold nanoparticles. Such catalytic gold nanoparticles, known as *nanozymes*, were obtained by coating them with thiols bearing the a catalytic unit, namely the Zn(II) complex of the ligand TACN. Microenvironment modulation was obtained by changing the spacer between the catalytic unit and the anchoring part (thiol moiety).

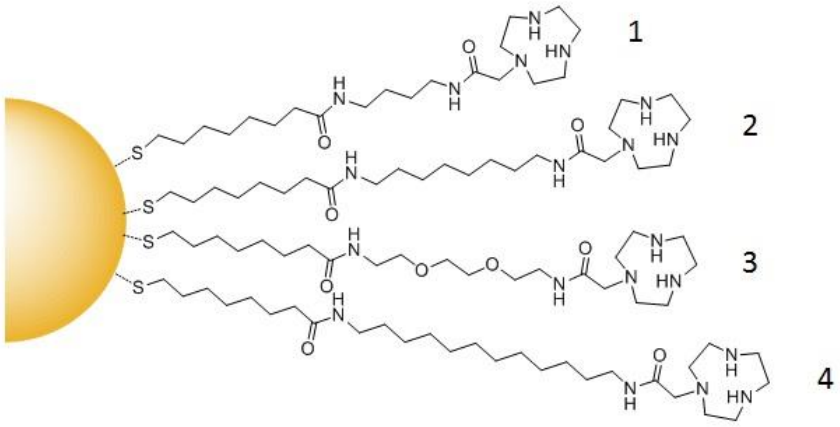

I will show that the increase the length of the alky spacer from four carbon atoms (thiol **1**) to twelve atoms (thiol **4**) strongly increases the nanozyme reactivity towards the hydrolytic cleavage of HPNP. On the other hand, longer but more polar oligo(ethyleneoxide) spacer in **3** does not have any effect on the nanozyme reactivity. The experiments reported will demonstrate that such a reactivity modulation depends on an enthalpy-driven stabilization of the transition state of the reaction and is strongly correlated to the polarity of the microenvironment, presumably the interface between the particle coating monolayer and the bulk water solution, where the reaction occurs.

Finally, in the last part of the present thesis, I shall report the results obtained by studying how the morphology of the gold nanoparticles-coating monolayer affects the reactivity of the nanozymes. Therefore, I prepared mixed-monolayer nanoparticles where the coating

contains simultaneously thiol **1** and the zwitterionic thiol (ZW), which bears a phosphorylcholine moiety, or the triethilenglycol-thiol (TEG, in different ratios). The main function of the latter is to improve water solubility to the nanozymes, but I reasoned that they could have an effect on the reciprocal organization and sorting of the molecules in the monolayer.

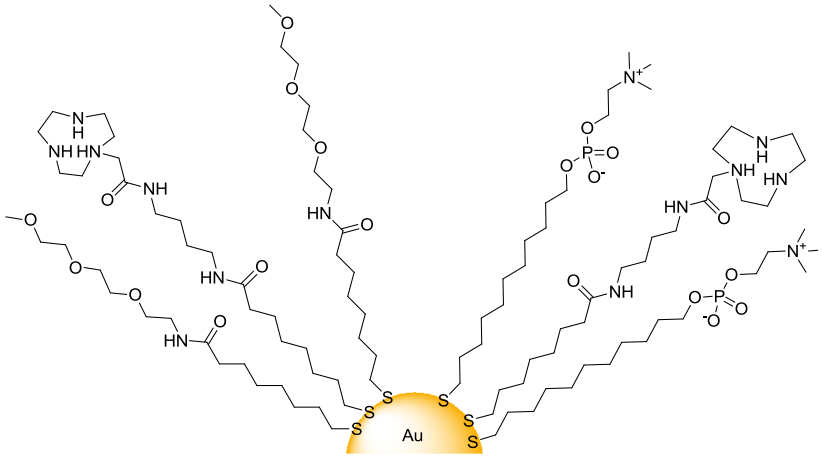

Indeed, preliminary experiments performed demonstrated that different distributions of the catalytic units in the nanoparticles surface, either in patches or random, were obtained when the two different inert thiols were used. Interestingly, such different distributions affect the substrate affinity of the catalytic system but not its activity.

In conclusion, we have performed a systematic approach to study of how the reactivity of Zn(II) ions in hydrolytic phosphate-cleaving catalysts can be modulated using different strategies, ranging to the modification of the ligand structure to the control of the local microenvironment or of the catalyst reciprocal proximity using monolayer protected nanoparticles.

Abstract

Questa tesi di dottorato riassume i risultati che ho ottenuto cimentandomi in un progetto di ricerca il cui obiettivo era l'individuazione di nuove strategie capaci di aumentare l'efficacia dei catalizzatori per l'idrolisi di diesteri fosforici. Questi catalizzatori, noti nella letteratura scientifica con il nome di "nucleasi artificiali", erano nel mio caso costruiti a partire da complessi dello ione Zn(II) con leganti poliamminci. La struttura dei complessi utilizzati ha spaziato da piccoli sitemi mononucleari a complessi sistemi catalitici supramolecolari basati su nanoparticelle di oro (nanozimi).

I diesteri fosforici sono di vitale importanza nella chimica biologica visto che formano parte dello scheletro di biomolecole essenziali come il DNA e il RNA. Queste macromolecole sono caratterizzate da un'alta stabilità contro la scissione idrolitica, utilie per garantire la preservazione dell'informazione genetica, che è dovuta proprio alla presenza dei residui fosfato. D'altra parte, l'idrolisi dei gruppi fosfodiesterei di DNA e RNA avviene negli organismi viventi in pochi millisecondi, grazie alle nucleasi, gli enzimi idrolitici preposti a questa reazione.

Il nostro interesse è quello di riprodurre l'attività di questi enzimi con sistemi di origine sintetica. In particolari, siamo convinti che il miglior candidato per costituire il nucleo "attivo" di sistemi idrolitici artificiali sia lo ione Zn(II). Conseguentemente abbiamo preparato una serie di complessi di Zn(II) caratterizzati da strutture e filosofie di assemblaggio anche molto diverse e ne abbiamo studiato la reattività nel promuovere la scissione idrolitica di un modello di RNA, il 2-idrossipropil-*p*-nitrofenil fosfato (HPNP).

Nella prima parte della tesi sono discussi gli interessanti risultato che ho ottenuto nello strudio della reattività di complessi monometallici di Zn(II) nella idrolisi dell'HPNP. I complessi studiati sono riportati in figura e sono semplici complessi monucleari dei leganti 1,4,7-triazaciclononano(TACN) e 1,4,7-trimetil-1,4,7-triazaciclononano (TMTACN).

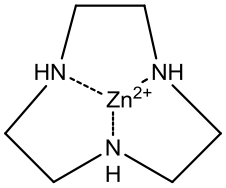

Complex 1. Zn(II) TACN

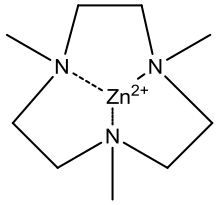

Complex 2. Zn(II) TMTACN

Gli studi effettuati dimostrano come le piccole differenze nella struttura dei due leganti portano a notevoli differenze nella reattività dei complessi. Nel corso della discussione sarà suggerito che tali effetti, mai descritti in precedenza, possano essere dovuti a diverse geometrie di coordinazione dello ione metallico.

Nella seconda parte della tesi mi sono dedicata a studiare gli effetti prodotti dall'ambiente locale in cui i complessi vengono a trovarsi sulla loro reattività come catalizzatori della scissione idrolitica di esteri fosforici. In quest'ottica, ho progettato una serie di sistemi supramolecolari basati su nanoparticelle d'oro funzionalizzate. Queste nanoparticelle catalitiche, conosciute come nanozimi, sono state ottenute ricoprendo i nuclei di oro con tioli dotati di un gruppo reattivo, in particolare di un complesso di Zn(II) del legante TACN. La modulazione del microambiente di reazione è stata ottenuta modificando la struttura dei tioli utilizzati, ed in particolare lo spaziatore inserito tra l'unità catalitica ed il gruppo tiolo preposto all'ancoraggio alla superficie d'oro-

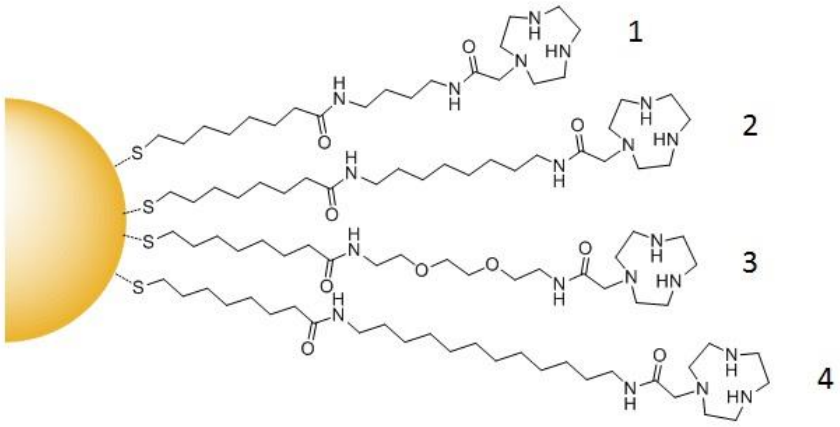

I risultati riportati dimostreranno che l'aumento della lunghezza dello spaziatore da quattro atomi di carbonio (tiolo **1**) a dodici atomi (tiolo **4**) produce un notevole aumento della reattività di questi nanozimi nell'idrolizzare l'HPNP. D'altra parte, l'inserimento di uno spaziatore di tipo oligo(ossietilenica) (tiolo **3**), più lungo ma anche più polare, non comporta alcun vantaggio in termini di reattività. La modulazione di reattività osservata dipende, secondo gli studi effettuati, da una miglior stabilizzazione, dovuta ad effetti di natura entalpica, dello stato di transizione della reazione. Tale stabilizzazione è fortemente correlata alla polarità locale del microambiente di reazione, presumibilmente l'interfaccia tra il monostrato e la soluzione acquosa.

Nell'ultima parte della tesi descriverò i risultati ottenuti studiando come la morfologia dello strato che ricopre le nanoparticelle d'oro influenzi la reattività dei nanozimi. In questa prospettiva, ho preparato nanoparticelle di oro (2 nm il diametro del nocciolo metallico) coperte in proporzioni diverse con monostrati misti composti dal tiolo **1** ed da un tiolo dotato di un gruppo fosfoilcolina (ZW) o di un residuo di trietileneglicole (TEG). La funzione primaria di questi ultimi tioli è apportare solubilità acquosa al nanosistema ma mi era sembrato possibile che essi potessero anche influenzare la disposizione delle unità catalitiche sulla particella.

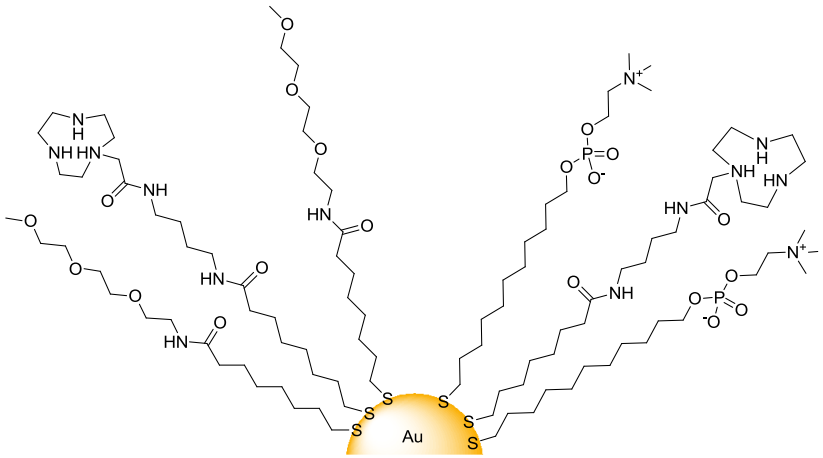

In effetti, gli esperimenti effettuati in via preliminare mostrano che l'uso dei due tioli porta a diverse distribuzioni delle molecole di ricoprimento che si dispongono in modo casuale o

formando “isole”. Queste diverse distribuzioni influenzano l’affinità dei nanozimi per il substrato HPNP ma non la sua attività idrolitica.

In conclusione, in questa tesi ho descritto i risultati ottenuti nell’effettuare uno studio simultaneo e sistematico di diverse possibili strategie capaci di modulare la reattività di agenti idrolitici artificiali basati sullo ione zinco(II). I risultati ottenuti potranno aprire la strada a nuovi sviluppi capaci di portare alla realizzazione di sistemi dotati di efficacia realmente comparabile a quella degli enzimi.

Chapter 1

GENERAL INTRODUCTION

1.1. Phosphorus in Nature

The general idea that life is mostly based in four elements C, H, N and O is inaccurate. Several other elements play fundamental roles, and one of the most important among them is phosphorus. Its role is often underestimated, maybe because of its low presence in the human body, being only 1 percentage in mass. Still, Nature has chosen this element to participate in essential functions for living organisms like, for example, the storage and transmission of the genetic information or the short term storage of the cellular energy by means of the phosphate diester group[1].

Phosphorus has an electronic configuration of [Ne] $3s^2$ $3p^3$ with five valence electrons and with *d* empty orbitals available. The coordination of the phosphorus in different compounds can be understood by using the hybridization orbitals theory of Linus Pauling[2]. The degeneration of the 3-level orbitals which produces five sp^3d hybrid orbitals partially occupied, which allows the phosphorous to form up to five sigma bonds with a basic structure of a trigonal bipyramid. Indeed, this is the situation found in the molecules of phosphorus pentafluoride (PF_5). Single-crystal X-ray studies of such molecule showed that PF_5 has two distinct types of P-F bonds: axial and equatorial being their length 1.58 Å and 1.52 Å, respectively.

Furthermore, such hybridization is also found in the phosphorane which is the intermediate in the cleavage reaction of phosphates (Figure 1a). However, phosphorus allows also the hybridization involving only the fully occupied *s* orbital and the partially occupied *p* orbitals giving four sp^3 hybrid orbitals which only three sp^3 orbitals available to form

sigma bonds in a triangular pyramid structure. This is the case of the formation of phosphines, where three oxygens form sigma bonds with the phosphorus. Still, phosphines can form another bond with one more oxygen atom giving the phosphate group which presents an additional double P-O bond of dative origin. The phosphorus provides two electrons from the fully occupied sp^3 orbital to the oxygen which accepts them, but also the oxygen provides two electrons to the phosphorus which accepts them in the low energy empty *d* orbitals, forming a double dative bond between the phosphorus and the oxygen. This results in the tetrahedral molecular geometry of the phosphate group where the length of the P-O double bond is shorter than the one of the other P-O single bonds[3] (Figure 1b).

Figure 1. a) Phosphorane intermediate with a hybridization sp^3d of the phosphorus. b) Phosphate group with a hybridization sp^3 of the phosphorus.

Notice that Nature has being very intelligent, there is not a better way to avoid nucleophilic attack than having the electrophile (the phosphorus) surrounded by negative charges of the oxygen atoms which discourage the approximation of the nucleophile by electrostatic repulsions, as in the case of phosphate mono- and diesters.

Such a highly resistance of the phosphate diester group toward the nucleophilic attack makes it an excellent building block for DNA and RNA, the molecules that have the important role to storage and carry the genetic information, respectively. Indeed, the presence of phosphates groups ensures a high stability to these two polianions in hydrolytic conditions, being the estimated half-life of DNA between hundreds of thousands and millions of years[4] and the one of RNA around one hundred years, both at pH 7 and 25 °C.

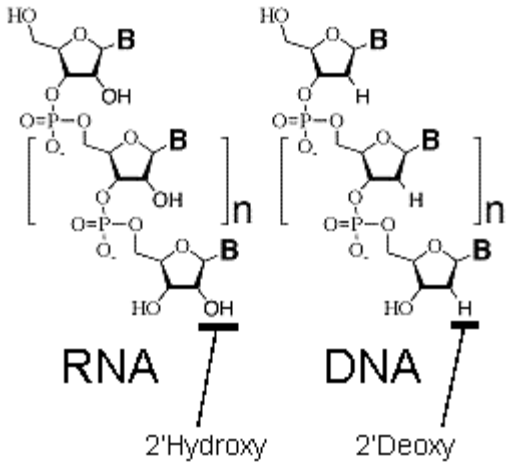

Figure 2. RNA and DNA backbones.

Nevertheless, the spontaneous degradation of DNA does not occur principally by a hydrolytic pathway. Indeed, it occurs mainly through different pathways like C-O cleavage, radical attack or nucleobase ring opening[4] (figure 3b). However, P-O cleavage is the only pathway followed in the case of enzyme catalyzed reaction.

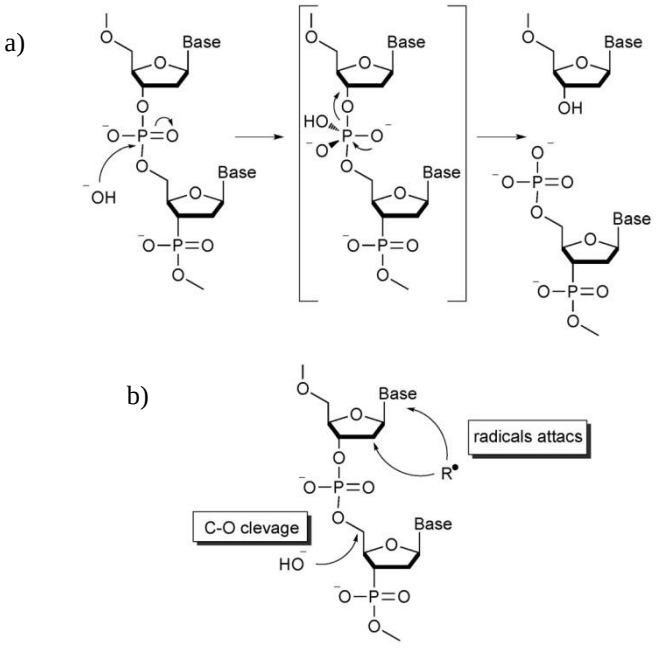

Figure 3. a) Reaction pathway for hydroxide promoted DNA hydrolysis and b) alternative DNA degradation pathways.

The hydrolytic mechanism of DNA cleavage in basic conditions is described in figure 3a. The phosphorus atom is attacked by a hydroxide ion acting as a nucleophile which leads to the formation of a pentacoordinated intermediate. The reaction evolves by the departure of the leaving group after breaking down the P-O bond in position 3'.

The difference in stability between DNA and RNA lies in the sugar moiety, that together with the phosphate group, constitutes the nucleic acids' backbone. In the case of the DNA, the absence of the OH group in position 2' in the ribose molecule makes it extremely stable in comparison with the RNA (Figure 2), where this OH group act as internal nucleophile in the cleavage reaction of the phosphate. Beside such differences, it must be underlined that the high stability of both these molecules makes difficult the characterization of their hydrolytic cleavage mechanism and, moreover, the direct measurement of their half-lifes is impossible. An accurate determination of the rate constants for the uncatalyzed hydrolytic cleavage of phosphate diesters is fundamental for a right assignment of the rate enhancements produced not only by enzymes, but also by man-made nucleases.

In the particular case of DNA, because of the enormous inertness of the phosphate group, the rate of hydrolytic cleavage is still under investigation by high temperature studies on model substrates. For example, the studies performed using the simple dimethylphosphate give $k = 2 \times 10^{-13} s^{-1}$ at pH 7 and 25 °C for the water attack on the phosphorus atom, which leads to an estimated half-life of more than 150 000 years. However, this phosphate model has shown intrinsic limitation since its cleavage proceeds almost quantitatively by C-O cleavage. A following study using neopentyl phosphate as substrate allowed a directly measurement of the rate P-O cleavage, since the C-O cleavage is inactivated by steric reasons, and provided a rate constant of 7×10^{-16} s^{-1} which corresponds to a half-life of more than 30 million years.

The higher intrinsic reactivity of the RNA allows more reliable studies using dinucleotide derivatives as the UpU dinucleotide[5]. In this case, the determined rate constant is $k = 2 \times 10^{-10}$ s^{-1} for the uncatalized reaction at pH 7 and 25 °C which corresponds to an estimated half-life of about 110 years. The mechanistic pathway for RNA cleavage is supposed to proceed via an intramolecular transesterification followed by hydrolysis of the phosphate cyclic intermediate[67].

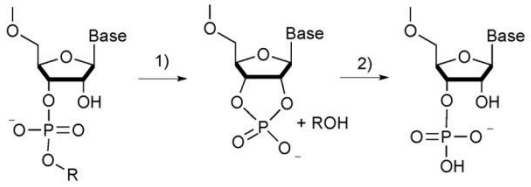

Figure 4. (1) Intramolecular transesterification and (2) hydrolysis of the cyclic phosphate.

However, the limitations of the proposed mechanism are exemplified by the isomerization process of RNA derivatives that can only be explained by a formation of a phosphorane intermediate (associative mechanism) as shown in figure 6[8].

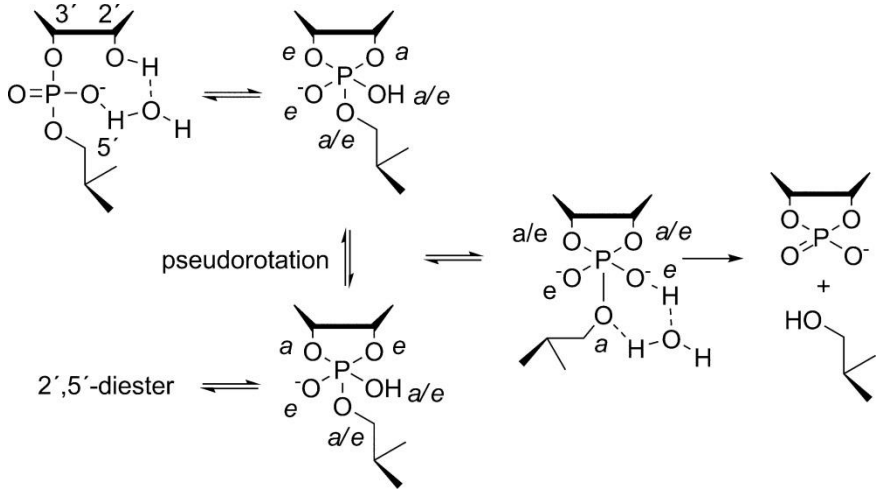

Figure 5. pH-independent cleavage and isomerization of RNA phosphodiester bonds.

In both mechanisms, the nucleophilic substitution at the phosphorus in the hydrolysis of phosphate esters can follow three limiting mechanisms (Figure 5): (i) a dissociative (D_N + A_N) mechanism in which the leaving group departure precedes the attack of the nucleophile with the formation of a discrete metaphosphate intermediate;(ii) an associative (A_N+D_N) mechanism in which the nucleophile attacks before the departure of the leaving group with the formation of a phosphorane intermediate;(iii) a concerted (A_ND_N) mechanism in which bond formation to the nucleophile and bond fission to the leaving group occur synchronously and no intermediates are observed.

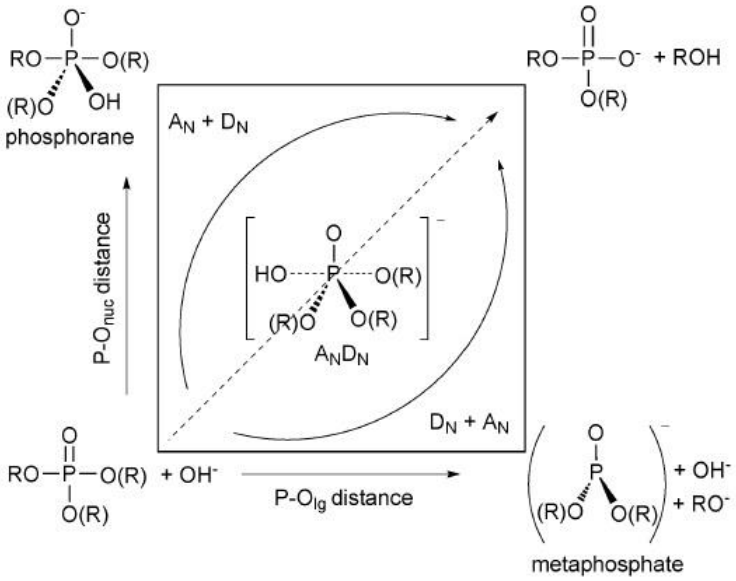

Figure 6. More O'Ferral-Jencks diagram showing the limiting mechanisms for phosphate esters hydrolysis.

The dissociative mechanism which goes through the formation of a metaphosphate intermediate is quite improbable since will lead to poorly coordinated phosphours. In general, the concerted mechanism with the structure of a transition state changing from loose to more tight (more associative) on moving from mono- to di- and to tri-esters is the accepted one for the phosphate esters hydrolysis.

Notwithstanding the stability of phosphate esters, their hydrolysis is speeded in Nature up to 10^{18}-fold accelerations thanks to the enzymes. With the aim to synthetize artificial nucleases able to reach the activity of the natural ones is fundamental to look deep into the active site of those enzymes to understand the sources of their efficiency in the hydrolysis of phosphate esters in DNA and RNA.

1.2. Metallohydrolases

The metallohydrolases[9] are part of a big family of proteins, the metalloenzymes, with one common feature, the need of a metal ion to carry out their biological function. In the active site of such enzymes is characteristic to find a series of amino acids, highly conserved, to bind the metal ion (Mn(II), Zn(II), Mg(II), etc.)needed to perform the hydrolytic reaction.

The hydrolysis of amides and phosphate esters is fundamental for living organisms (Figure 7). Proteins are degraded after the execution of their biological role to recover the building blocks (amino acids) to build new proteins (cell economy). Moreover, the lack of protein degradation can cause some seriousness illness. The same happens with nucleic acids, mRNA has to be degraded after protein synthesis to avoid over-expression of the resulting proteins, or DNA cleavage is necessary to ensure the genetic recombination during the meiosis.

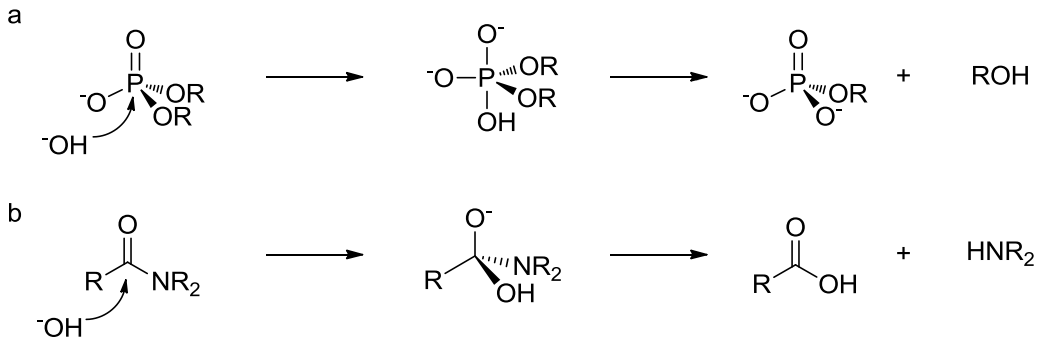

Figure 7. Base-promoted hydrolytic mechanism of a) phosphate diester and b) amides.

The efficiency of such enzymes is remarkable since they can reach acceleration up to 10^{17}-fold over the uncatalyzed reaction. Several studies reveal that certain amino acids are highly preserved in the active site of hydrolytic enzymes, the main reason is that their functional groups together with the metal ions are the responsible of enzymes efficiency.

The peptidases, the enzymes that hydrolysis peptide bonds, are classify depending of the mechanistic pathway followed to cleavage the peptide bonds. The first one composed by the enzymes that exploit the functional group of amino acids, as serine or cysteine which are, for example, the chymotrypsin and papain, respectively. In the second one, we can

find the enzymes, like the pepsine, that carry their activity due to a general acid/based mechanism thanks to the carboxylic groups of aspartic or glutamic acids. The last one is constituted by enzymes, like carboxypeptidases but also phosphatases and nucleases, that take advantage of the Lewis acidic character of metal ions such as Zn(II), Mn(II), Fe(II) or Mg(II) to enhance the electrophilic nature of the C atom of the carboxylic group (or the P atom of the phosphate group) and, at the same time, reduce the pK_a of metal-bound water molecule making it a more available nucleophile. Furthermore, the activity of these metal ions can be assisted by the functional groups of the amino acids presented in the enzymes' active sites. Additionally, more than one metal ion can participate in the hydrolytic reaction.

1.2.1.Monometallic Metallohydrolases

This category is principally constituted by peptidases that uses only one metal ion, prevalent Zn(II), for their hydrolytic activity.

The best studied monometallic metallohydrolases are carboxypeptidase A and thermolysin (Figure 8a). Although their evolution have been different, both enzymes uses Zn(II) ion in a very similar fashion to catalyze the hydrolysis of peptide bonds. Thanks to the crystal structure of the carboxypeptidase A, it has been observed that Zn(II) is coordinated to two imidazole groups of two histidine residues (His-69 and His-196) and to the carboxylic group of Glu-72. The coordination sphere is completed by a water molecule that acts as a nucleophile. Also the structure of the thermolysin has been studied, finding a lot of similarities of the functional group in the active site (Figure 8b).

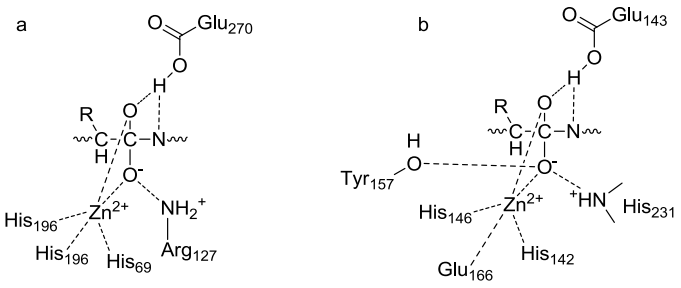

Figure 8. Transition state proposed for the enzymatic hydrolysis of peptide bonds catalyzed by a) carboxypeptidase A and b) thermolysin.

The same mechanism is performed by both enzymes where the Zn(II) has two important roles, the generation of the nucleophile which is the metal-bound hydroxide and the stabilization of the negative charge generated in the carboxylic oxygen in the transition state. The positively charged amino acid residues, Arg-127 (carboxypeptidase A) and His-231 (thermolysin) also participate in such stabilization. The Glu 270 and 143 residues preserved in both enzymes work first as a general based since they accept the proton from the nucleophile, and then as a general acids by protonation of the leaving group.

1.2.2.Bimetallic Metallohydrolases

Our attention is focused on the enzymes able to catalyze the hydrolytic reactions thanks to the presence of two metal ions in their active sites. The number mechanistic studies on such enzymes increases every year. There are examples of enzymes that are able to hydrolyze the C-N bond of the urea or of the guanidine group presented in the amino acid Arg. There are also enzymes that hydrolyze the P-O bond of phosphate mono-, di- and tri-esters, like RNA or DNA. Since the choice is large only one example of phosphatase and one of nucleases, which are related with the objective of this thesis, will be discussed.

1.2.2.1. Alkaline phosphatase of E. Coli

Alkaline phosphatases (AP)[9,10] are non-specific phosphomonoesterases found in both eukaryotic and prokaryotic organisms. In particular, the one of E. Coli has been studied more in detail. It is a homodimeric protein of 94 kDa that contains two Zn(II) ions and one Mg(II). In the active site, the Zn(II) are found in a distance of 4.1 Å and are essential for the enzyme's activity, while the Mg(II) enhance the reactivity of the enzyme but it is not fundamental. One of the Zn(II) ions is pentacoordinated to His-331, His-412, the two oxygen atoms of the Asp-327 and to the oxygen of the phosphate substrate, while the other Zn(II) is tetracoordinated to His-370,to one oxygen atom of Asp-51, to another oxygen atom of Asp-369 and to phosphate through one oxygen atom. The reaction evolves by the formation of a phosphoenzyme intermediate thanks to the presence of the amino acid Ser-102 (Figure 9).

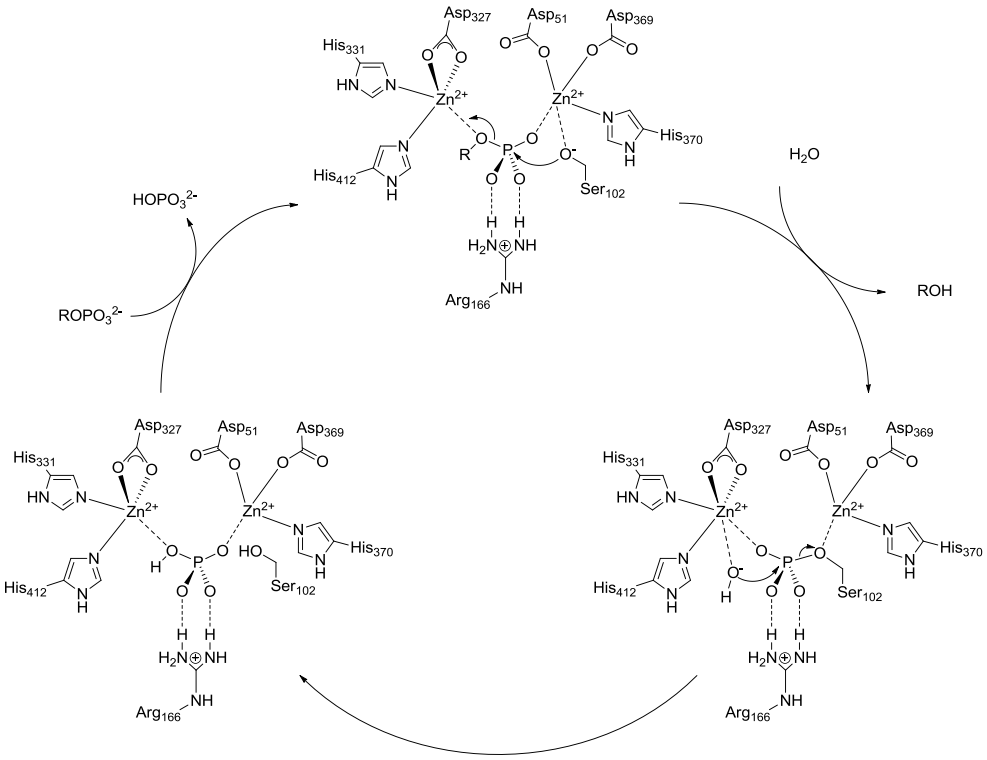

Figure 9. Hydrolytic mechanism proposed for the alkaline phosphatase within the active site.

In the course of the reaction, both Zn(II) ions activate the nucleophile alternatively. In the first step, one Zn(II) activates the hydroxyl group of the Ser-102 which attacks the phosphate group forming the phosphoenzyme intermediate while, in the second step, the other Zn(II) activates a water molecule that hydrolyses the intermediate. In every step the function of the metal ions is different but complementary: while one activates the nucleophile the other one stabilizes the negative charge of the leaving group. Furthermore, both metal ions stabilize the pentacoordinated transition state of both the steps, supported by the formation of H-bonds with the residue Arg-166. The important role played by the residues Ser-102 and Arg-166 was demonstrated by mutant of AP where those amino acids were substituted being the mutant AP much less reactive than the native form.

1.2.2.2. DNA polymerase I

The protein DNA polymerase I participates to the process of DNA replication. It is able to perform three different activities: synthesis of DNA, cleavage of DNA in position 3'-5' (reverse) but also in position 5'-3' (forward) by the used of three different domains present in the same enzyme. The exonuclease activity (DNA degradation) of this enzyme allows it to remove possible errors during the DNA synthesis. All these enzymatic activities need the presence of metal ions with valence II.

The active site of the reverse exonuclease activity, the hydrolysis of DNA in position 3'-5', has been deeply studied by X-ray cristalography. Such studies reveal the presence of two coordination sites for divalent metal ions (Mg(II), Mn(II), Zn(II) or Co(II)) which are essential for the enzymatic activity. One metal (A) is bound to the enzyme, while the second one (B) is only bound in the presence of the substrate with an intermetallic distance of 3.9 Å. Both metal ions are coordinated to the same oxygen atom of the substrate and to the same amino acid residue Asp-355. The metal ion A is also coordinated to oxygen atom of Asp-501 and to another oxygen atom of Glu-357, while the metal ion B is also coordinated to one oxygen atom of Asp-424 (not shown). Both metal ions stabilize the transition state and are essential for the hydrolytic mechanism, the metal A assisting the nucleophilic attack while metal B assisting the leaving group departure, in one single step.

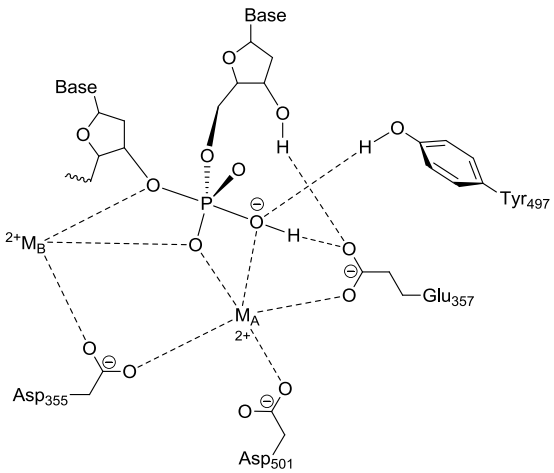

Figure 10. Proposed transition state in the DNA hydrolysis 3'-5' catalyzed by DNA polymerase I.

1.3. Artificial nucleases

The previous paragraphs highlight the important role that metal ions play in the hydrolysis of phosphate esters. In the last decades, the synthesis of small metal binding catalysts have been developed with the aim of rivalling enzyme's activity and have been very useful in the study of the possible activation modes played by these metal ions which are briefly summarized in figure 11[11,12].

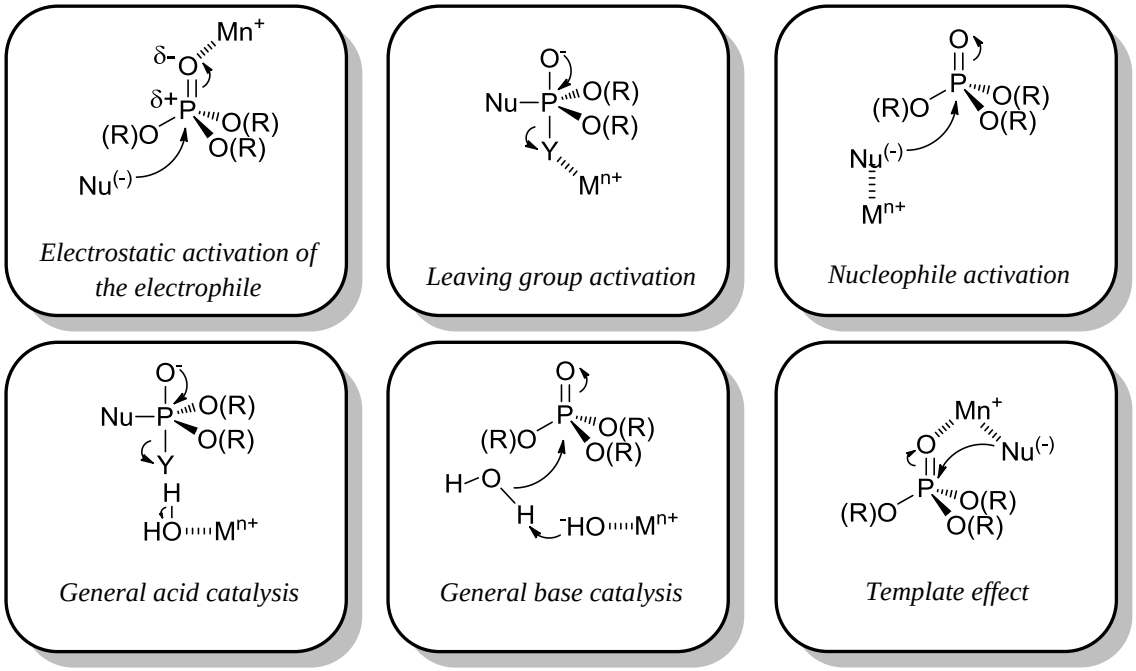

Figure 11. Possible activation modes provided by metal ions for acceleration of the hydrolysis of phosphate esters.

The roles of the metal ion in the catalysis of phosphate diesters can be divided in two principal groups: direct and indirect modes. The three direct modes are:

1. *Electrostatic activation of the electrophile:* acting as Lewis acid, metal ions activates the phosphate group by removing electrondensity from the phosphorus making the nucleophilic attack easier. This point is also important in the stabilization of the transition state
2. *Leaving group activation:* the coordination of metal ion to the alcoholic oxygen of the leaving group decreases its pK_a which facilitates the departure of the alkoxyde.

3. *Nucleophile activation:*water/alcohol molecules are more acidic when coordination to metal ions which ensure a higher concentration of hydroxide/alkoxyde at neutral pH close to the phosphodiester group.

Moreover, the indirect modes include the *general acid/base catalysis*(4/5)[12] of the water/hydroxide molecules bound to the metal ion. Finally, the *template effect* (6) where the metal ion is coordinated to both, the substrate and the nucleophile decreasing their electrostatic repulsion which brings two negatively charged species in closed proximity to react. Obviously, these activation modes can be combined giving more complicated catalytic processes, especially in the case of bimetallic complexes which often are more effective than the monometallic ones.

In the particular case of monometallic complexes, a possible reaction pathway is described in figure 12 where four main steps can be distinguish: I) the acid dissociation of a metal coordinated water molecule characterized byK_a; II) the coordination of the substrate to the metal ion (K); III) the nucleophilic attack of the metal-bound hydroxide to the substrate (k') and IV) the departure of the leaving group (k'').

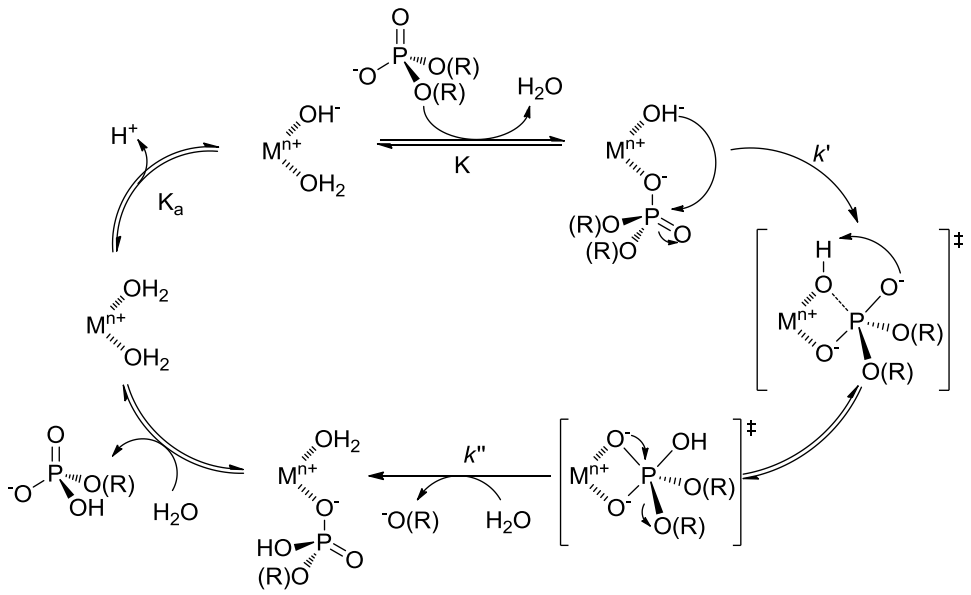

Figure 12. Reaction pathway for the hydrolysis of phosphate ester catalyzed by a metal ion.

An interesting study using inert complexes of Co(III) by Chin and coworkers[13], shown the contribution of each possible activation to the enhance of hydrolytic reactivity of metal-based catalyst. Being the acceleration due to lewis acid activation of one metal ion only two orders of magnitude (10^2) while intramolecular nucleophile activation has a most important contribution (10^8-fold), followed by leaving group activation (10^6-fold)

1.3.1.The election of the metal ion

The right election of the metal ion can be only done after taking into account different parameters as the chemical behavior of these metal ions in solution or the principles that govern their interactions with different ligands. With the aim to understand how experimental conditions influence the phosphate hydrolysis promoted by metal ion-based catalysts is important to describe the behavior of metal ions in aqueous solution, where most of them exist as cationic aquo-complexes $[M(H_2O)_x]^{n+}$, which tend to form aquo-hydroxy complexes $[M(H_2O)_{x-1}(OH)]^{(n-1)+}$ according to the pK_a values of the metal bound water molecules. The positive charge of the metal ion facilitates the loss of a water proton as a consequence the pK_a of metal-bound water molecules is lower than the pK_a of water molecules. The number of water molecules, hydroxyl ions and/or other ligands (neutral or charged) that can be directly bound to the same metal ion forming the inner-sphere is determined by its coordination number. Moreover, the geometry of the inner-sphere depends on the ionic radius and oxidation state of the metal ion. In addition to the inner-sphere, it is possibleto find an outer-sphere of water molecules interacting through H bonds with water/hydroxide molecules of the inner-sphere. Hence, the inner-sphere has a directly effect in the nucleophile and leaving group activations while the outer-sphere explains the "indirect" general acid/base catalysis previously described. In addition, a rapid ligand-exchange kinetics is desirable since it favors the binding of reactants and the releasing of products.

Furthermore, the electrostatic activation of the electrophile depends of the lewis acid character of the metal ion. The development of lanthanide-based catalyst has attracted a lot of attention in the last decades, and interesting results have being obtained, due to the high lewis acidity of those metal ions and the absence of redox chemistry. Noticeably,

nucleotides cleavage can occur not only by a phosphate hydrolysis pathway but also by an oxidation of the C-H bonds which is not desirable since is not the mechanism follow by nucleases. This led us to rule out metal ion of active redox species as Cu, Co or Mn, although their inherent lewis acid activity.

As a summary, a good metal ion for phosphate cleavage should meet the following criteria: a) high lewis acid character; b) absence of relevant redox chemistry in physiological conditions; c) rapid ligand-exchange kinetics. But, also, it should be safe and cheap. The metal ion that best accomplish this criteria is Zn(II).

Zn(II) belongs to the group 12 of the periodic table, it is a peculiar transition metal ion featuring filled *d* orbitals but empty outer shell s orbitals. The primary consequence of this electronic configuration is that Zn(II) has no ligand field stabilization energy and, as a result, it can easily adapt, without any additional energy cost, its coordination geometry. This feature also allows a rapid ligands exchange[11]. Moreover it does not present redox chemistry in physiological environment. However, its Lewis acid character is not as strong as that of the other metal ions as lanthanides and Cu(II). However, lanthanides are toxic even at low concentrations while Zn(II) is not, while Cu(II) is easily reduced to Cu(I) which in turn easily oxidized to Cu(I).

The bibliography of metal-based artificial nucleases with cations diverse than Zn(II) is extensive, especially in the case of lanthanides and Cu(II). However, based on the Zn(II) characteristic previously described we have focus our attention to create Zn(II)-based catalyst for phosphate cleavage. This is the main reason to justified the description of mono- and bi-metallic catalyst afterwards, although few example of other metal-based catalyst will be commented.

Nevertheless, it is also possible to catalyze the hydrolysis of phosphate esters with metal-free catalyst, although the rate acceleration of these systems are lower than the metallic ones, appealing results have been obtaining especially with RNA and its derivatives. This systems are particularly attractive to study the self-regulation of RNA molecules.

1.3.2.The election of substrates

Because of the high hydrolytic stability of DNA and RNA, but at the same time their vulnerability to nucleases contamination or degradation via oxidative pathway, it is difficult to use these substrates to perform kinetic and mechanistic investigation. Hence, to perform such studies chemists prefer to use small molecules of phosphate derivatives. In the particular case of DNA, the most commonly accepted model is bis *para*-nitrophenyl phosphate (BNP, Figure 13a). Despite the presence of two good leaving groups, this molecules is quite stable, being the rate of the uncatalyzed reaction 1.6×10^{-11} s^{-1}, which corresponds to a half-life of more than 1300 years. In the case of RNA, the most employed model is the 2-hydroxypropyl-*para*-nitrophenyl phosphate (HPNP, Figure 13b) which contains a hydroxyl nucleophile in position 2' as the RNA. As a consequence of the presence of this internal nucleophile the intrinsic reactivity of HPNP is higher, even at room temperature, than the one of BNP which allows an accurate mechanistic investigation of its hydrolysis.

Figure 13. Structures of the a) DNA-model substrate bis *para*-nitrophenyl phosphate (BNP) and b) RNA-model substrate 2-hydroxypropyl-*para*-nitrophenyl phosphate (HPNP).

The use of the *para*-nitrophenol as phosphate substituents in both substrates is not purposeless: indeed, this substituent is a good leaving group which is the responsible of the high reactivity of the two molecules toward nucleophiles. Moreover, once cleavage the *para*-nitrophenolate can be easily follow by UV spectroscopy since it has an absorbance maximum at 400 nm (for *para*-nitrophenol the maximum is at 320 nm) which facilitates the following of the cleavage reaction. However, *p*-nitrophenolate is a much better leaving group than alkoxides present in nucleotides, this allows us to rule out the leaving group

activation as limiting step in the hydrolysis of model phosphodiesters but not in DNA and RNA. This point is very important when mechanistic information obtained for those substrates is extended to the natural substrates where the departure of the leaving group can play a fundamental role.

1.4. Zn(II)-based artificial ribonucleases

Since in 1965, the first cleavage of RNA by free Zn(II) ions was reported, Zn(II)-based catalysts for the hydrolysis of RNA and its analogues have received a lot of attention. However, the mechanistic details of the phosphodiester hydrolysis catalyzed by metal ions is still unclear and several point remain open to suggestions/discussion. In the presence of metal ions, only the transesterification of the cyclic phosphorane (RNA-) intermediate is detected while the isomerization process to give the 2',5'-phosphodiester is not observed, while it occurs, in the absence of metal ions, in neutral or acidic conditions. The literature on synthetic ribonucleases is extensive[14–17], as a consequence, we will discuss only the most relevant examples that go from small monometallic complexes to big supramolecular assemblies.

1.4.1 Monometallic complexes

The most efficient catalysts are based in the use of neutral ligands because anionic ligands, although they usually gives more stable complexes, have substantially no activity. In 2007, Morrow and coworkers[18] reported an interesting work using as Zn(II) ligands: 1,5,9-triazacyclododecane and 1,4,7-triaza-10-oxacyclododecane (Figure 14). The second order rate constants obtained for the hydrolytic reaction of these complexes towards HPNP are 1.8×10^{-2} M^{-1} s^{-1} and 2.8×10^{-2} M^{-1} s^{-1}, respectively. They showed preferentially tripodal coordination while the related tetradentate ligand 1,4,7,10-tetraazacyclododecane is essentially inactive ($k_2 = 1.5 \times 10^{-3}$ M^{-1} s^{-1}).

Figure 14. Structures of the Zn(II) complexes of a)1,5,9-triazacyclododecane and b) 1,4,7-triaza-10-oxacyclododecane.

The catalytic reactivity of monometallic complexes can be enhanced by the presence of organic groups that can assist the reaction by formation of H-bond with the substrate. A good example of this synergic effect reported by Anslyn and coworkers[19]. The complexes of a pyridyl derivative which bears two guanidinium or methyl ammonium substituents (Figure 15a), the contribution of the H-bond donors to the catalytic activity is remarkable since the complex bearing the guanidium groups is 3300 times more efficient than its dimethyl counterpart (Figure 15a-i), and the complex with the methyl ammonium is 370 times more efficient than the dimethyl counterpart.

i: R = H
ii: R = NH-C(NH_2)=NH_2^+
iii: R =NH_3^+

i: R = H
ii: R = NH_2

Figure 15. Zn(II) complexes of a) pyridyl derivates bearing i) methyl, ii) guanidinium, or iii) methyl ammonium substituents; b) tris(pyridine-2-ylmethyl)amine (TPA) ligand bearing as substituents i) hydrogens ii) amino groups.

Another interesting example of the simultaneous action of H-bond donors and metal ion activation are the Zn(II) complexes of a series of tris(pyridine-2-ylmethyl)amine (TPA) based ligands, where the 2-amino derivative cleaves HPNP two orders of magnitude faster than the unsubstituted reference compound (Figure 15b-i). Indeed, the effect of amino groups is comparable to the presence of an additional metal ion in the increase of the reaction rate, as highlight by the following examples. The Zn(II) complex of *N*,*N*-bis(6-

aminopyridine-2-ylmethyl)-2-aminoethanol cleaves HPNP as faster as the bimetallic Zn(II) complex of *N,N,N',N'*-tetrakis(pyridine-2-ylmethyl)-1,3-diaminopropan-2-ol [20](Figure 16).

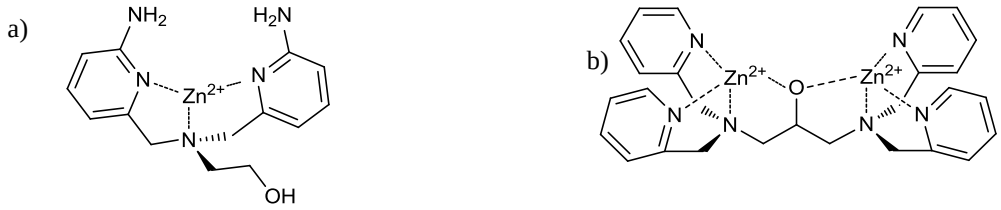

Figure 16. Zn(II) complexes of a) N,N-bis(6-aminopyridine-2-ylmethyl)-2-aminoethanol ligand and b) N,N,N',N'-tetrakis(pyridine-2-ylmethyl)-1,3-diaminopropan-2-ol.

1.4.2 Bimetallic complexes

As previously mentioned, the addition of a second metal ion enhances the activity of hydrolytic catalysts due to a double lewis acid activation of the substrate, a situation that can be found in several enzymes' active sites. The appropriate distance between two metal ions to observe double lewis acid activation is around 3–4 Å. Such distance can be obtained when both the metal ions share a common donor atom within the ligand structure. Two interesting investigation that have used this strategy are following described.

First, the dinuclear Zn(II) complex of 1,3-bis(1,4,7-triazacyclononan-1-yl)propan-2-ol where two TACN-Zn(II) complexes are connected by a μ-alkoxo bridge (Figure 17), shows two orders of magnitude acceleration in the cleavage of HPNP compared with the mononuclear analogue[21]. At pH 7.60, the second order rate constants are 25×10^{-2} M^{-1} s^{-1} and 0.13×10^{-2} M^{-1} s^{-1} for the di- and mononuclear catalyst, respectively. Remarkably, the lack of the hydroxyl group in the bimetallic ligand cancels the cooperativity between the two metal ions.

Figure 17. Zn(II) complexes of a) 1,3-bis(1,4,7-triazacyclononan-1-yl)propan-2-ol and b) 1-hydroxyethyl-1,4,7-triazacyclononane.

The most interesting case is the greater activity obtain by the Zn(II) complex of *N,N,N',N'*-tetrakis(6-aminopyridine-2-ylmethyl)-1,3-diaminopropan-2-ol (Figure 18) reported by Williams and coworkers[22] in 2006 which combines double lewis acid activation and H-bond interactions of the amino substituents. This catalyst is 700 times more efficient than the monometallic structural analog. Half of the acceleration produced comes from the enhancement of binding affinity and, the other half from intracomplex reactivity enhancement. Moreover, the Michaelis-Menten parameters obtained for the cleavage of HPNP catalyzed by this complex at pH 7.4 and 25 ◦C, are k_{cat}= 0.017 s^{-1} and K_M 0.32 mM which means a rate acceleration with respect to the uncatalized reaction of almost 10^5-fold. Notice, that this catalyst is the actual benchmark for HPNP hydrolysis performed by small bimetallic complexes. Furthermore, this catalyst is as efficient in cleaving UpU derivatives as it is in cleaving HPNP.

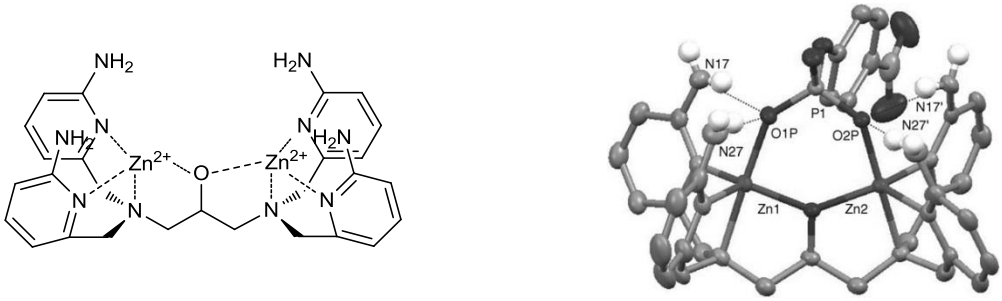

Figure 18. Zn(II) complex of N,N,N',N'-tetrakis(6-aminopyridine-2-ylmethyl)-1,3-diaminopropan-2-ol.

Notwithstanding the great rate enhancement reached by this last catalyst in the cleavage of phosphodiester derivatives, the goal of achieve enzymes' activities is still far. The main reason is likely the environment of the enzymes' active sites which has a dielectric constant lower than the aqueous media where normally enzymes are found. The electrostatic stabilization between the positive metal ions and the negative substrate is maximized in low polarity environments as demonstrated by Brown and coworkers[23–25]. They have demonstrated that even a poorly organized catalyst, as the Zn(II) bimetallic complex of 1,3-bis(1,5,9-triazacyclododenan-1-yl)propane (Figure 19), is surprisingly a great catalyst for the cleavage of HPNP in light alcohol as methanol or ethanol. Acceleration obtained is 12 order of magnitude over the uncatalized reaction, almost approaching enzymes' activity. Notice that the very same catalyst in aqueous solution is

practically inactive since the lackness of the μ-oxo brigde eliminates preorganization of metal ions necessary to the double lewis acid activation. The second order rate constant for this system is 2.75×10^5 M^{-1} s^{-1}, which is several orders of magnitude faster than any acceleration previously performed by small molecules in aqueous solution.

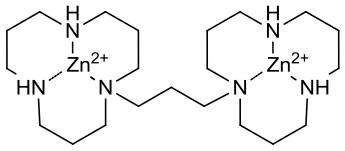

Figure 19. Zn(II) bimetallic complex of 1,3-bis(1,5,9-triazacyclododenan-1-yl)propane.

The fundamental outcome of this work is that, even though H-bonds interactions and double lewis acid activation produce notable contributions accelerating the cleavage of phosphate diester, the environment that surrounds the reaction is crucial. This is not trivial because it means that small molecular entities will never reach enzymes' activity since they cannot imitate the low polarity conditions found in light alcohols while working in water.

The challenge of mimicking the low polarity environment of enzymes' active sites with artificial nucleases can be only accomplished if the supramolecular chemistry enters in action. Nature has create big molecules, like proteins are, not by chance, hand-made catalyst should adopt the same strategy.

1.4.3 Supramolecular architectures

One of the first examples of using supramolecular architectures to obtain cooperation between metal ions to accelerate the cleavage reaction of phosphate diester was reported by Reinhoudt and coworkers[26]. A calix[4]arene scalffold was substituted with one, two or three 2,6-bis(aminomethyl)pyridine units on the upper rim (Figure 20). In the presence of Zn(II) ions, the system achieved remarkable rate acceleration on the transesterification of HPNP, being the trimetallic complex the most active since it reached a 32 000-fold

acceleration over the uncatalized reaction at pH 7 and 25 °C in a mixed medium composed by water and CH_3CN 1:1.

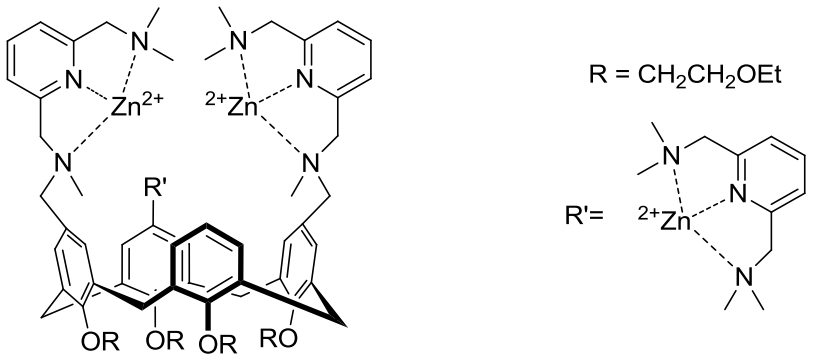

Figure 20. Zn(II) complex of the calix[4]arenes bearing 2,6-bis(aminomethyl)pyridine metal binding units.

There are two main reasons for efficiency of this system, both of them due to the calixarene scaffold. The first one is that, it provides a hydrophobic cage for the binding of the nitrophenyl moiety of the HPNP. The second one is the flexibility of the upper rim that allows the modification of the Zn(II)-complexes gap to achieve the best intermetallic distance for the reaction requirements. Indeed, the modification of the lower rim with an ether brigde produce a rigid system that is about 8 times less reactive than its flexible analog.

The three metallic system was 35-fold more reactive than its monometallic counterpart. However, the binding constants for the substrate are lower than for the bimetallic counterpart (5.5×10^4 M^{-1}), which makes thinking that the third metal chelating unit does not play a direct role in the transesterification reaction, especially when the reactivity increase from the three metallic complex with the respect to the bimetallic system was very small.

The system was also efficient in the cleavage of ribonucleotides showing remarkable differences in the activity of the trimetallic complex compared to the bimetallic one. Interesting enough, the reactivity of the trimetallic complexes towards dinucleotide UpU and GpG was higher than towards ApA. Such behavior is justified by supposing that one of the three Zn(II) units binds the acidic amide group on U or G and, as a consequence, acts as recognition unit while the remaining two acts as catalyst.

Another interesting example to reach selective cleavage towards ribonucleotides substrates was reported by Lönnberg and coworkers[27]. They created bi- and trinuclear Zn(II) complex from connecting 1,5,9-triazacyclododecane ([12]aneN$_3$) groups as nucleating moeities with different spacers. In figure 17 are reported the best performing systems. The dinuclear complex (Fig 21a) cleaves dinucleotides containing uridine (ApU or UpA) since one of the azacrown moieties anchors the catalytic system to the uracil base and the other one acts as a catalyst. However, this system is not able to cleave UpU derivatives since both azacrown units are bound to the uracil bases leaving no metal complex units available for phosphate cleavage. This issue is resolved by the use of the trinuclear complex reported in figure 21b.

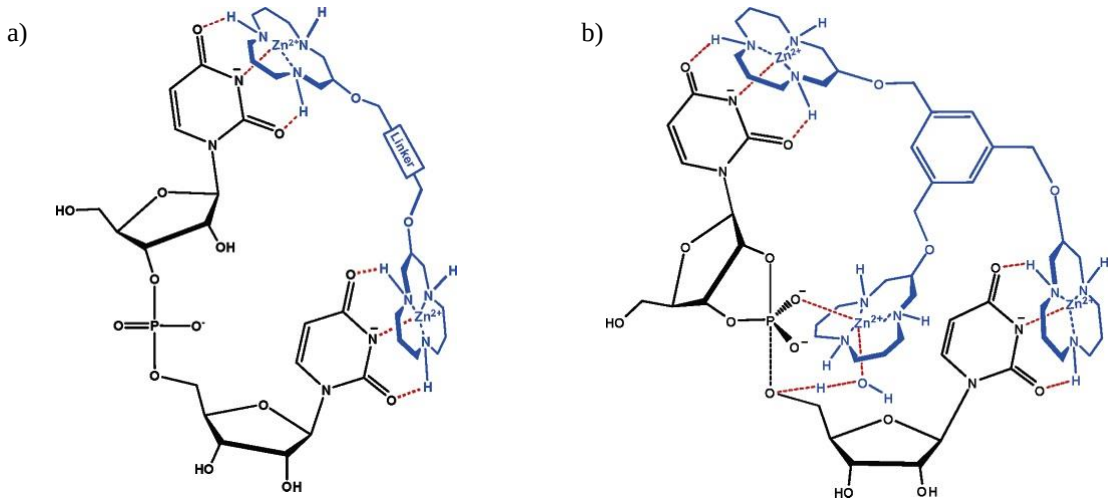

Figure 21. a) bi- and b) trinuclear Zn(II) complex from connecting 1,5,9-triazacyclododecane ([12]aneN3)

The use of peptides as scaffolds to create bimetallic systems was studiee by Scrimin and Kawai, independently. Scrimin and coworkers[28] used a heptapetide oligomers (figure 22a) that folds in a 3_{10}-helical conformation due to the presence of several α-disubstituted amino acids. As a consequence, the two 1,4,7-triazacyclononane ([9]aneN$_3$) moieties face each other at a distance of one pitch of the 3_{10}-helix (6 Å). This systems accelerates 50 times the transesterification of HPNP over the background reaction at pH 7 and 40 °C and its 3 times more reactive than the monometallic counterpart. Notably, this system is also active in the cleavage of plasmid DNA (this reactivity will be mentioned later on).

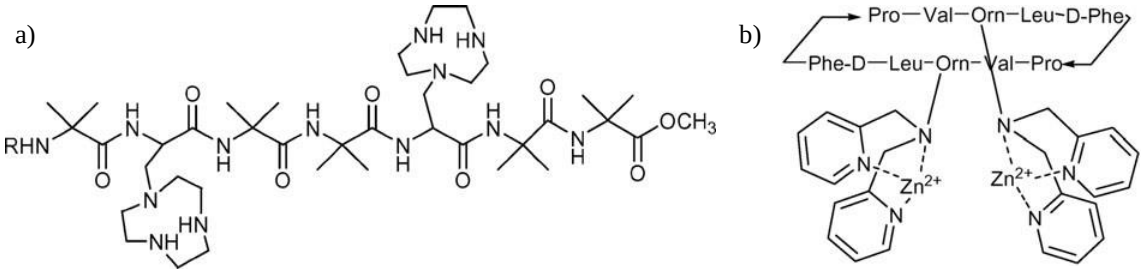

Figure 22. a) heptapeptide bearing two 1,4,7-triazacyclononane metal binding units and b) cyclic peptide-based catalyst.

Kawai and coworkers[29] used a cyclic peptide as scaffold to append two bis(pyridinylmethyl)amine units (Figure 22b). The Zn(II) complex of such a ligand is able to cleave HPNP with a 6500-fold acceleration at pH 7 (unfortunately, the temperature at which the experiments were performed was not reported by the authors) in a mix medium (80% CH_3CN/water). The bimetallic complex was 300-fold more reactive than the monometallic model. Furthermore, the role played by the cyclic peptide is highlighted by the fact that the same metal binding units linked by a propane spacer produced only an 80-fold acceleration of the reaction.

Moving to more complexes systems, the use of gold-nanoparticles to self-organized molecules on their surface was cleverly explored by Scrimin and coworkers[30]. They functionalized the gold-nanoparticles with a mixture of alkyl thiols and 1,4,7-triazacyclononane ([9]aneN_3) derivative thiols in the ratio 1 : 1.2 (Figure 23). The activity of such a system reaches a maximum when all metal binding unit are saturated by Zn(II) ions and the catalytic units can cooperate between them in the trasesterification of HPNP. Michaelis-Menten parameters, k_{cat} = 4.2 × $10^{-3}s^{-1}$ and K_M = 0.93 mM at pH 7.4 and 40 °C, reveals that this system is one of the most active ever described. This example was the first generation of "nanozymes" that in the current thesis work was improved to a second generation.

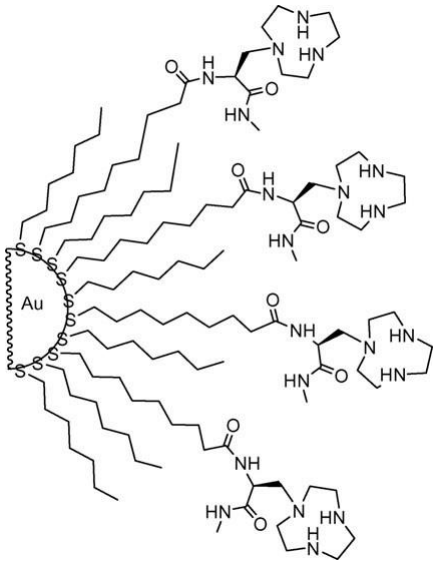

Figure 23. First generation "nanozymes"

1.4.4 Sequence-selective artificial ribonucleases

Although based in Cu(II), it is worthy mention the work of Strömberg and coworkers[31] on the synthesis of sequence-selective RNA catalyst. They studied the reactivity of a peptide nuclei acid (PNA)-based system (PNAzymes, Figure 24) that carry a Cu(II)-binding unit, the 2,9-dimethylphenanthroline group, towards the hydrolysis of RNA. The system is site and sequence specific because the target is cleaved at the non paired region (RNA bulge) which is formed after binding to the PNAzyme by Watson-Crick interactions. Moreover, in substrate excess conditions the PNAzyme demostrated to undergo turnover which demonstrates a true enzyme behavior.

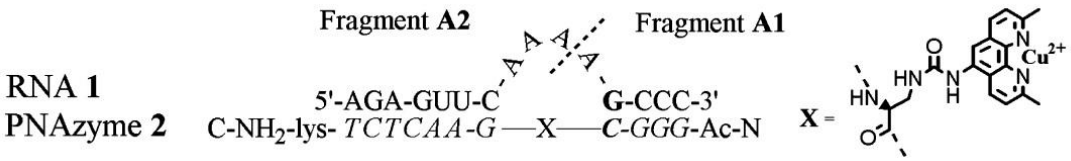

Figure 24. Illustration of the site and sequence specific cleavage performed by PNAzymes.

1.5 Zn(II)-based artificial desoxyribonucleases

Previously we discussed the problems in using DNA and its oligonucleotides to perform mechanistic studies, so that the use of DNA models is extensively accepted. One of the most common DNA model is the bis *para*-nitrophenyl phosphate. However, there is form of DNA which is amenable for cleavage studies: the supercoiled plasmid DNA found in bacteria cells which contains several thousand base pairs. This particular DNA form can be used in reactivity studies because it enhanced the detection of rare cleavage events. Indeed, one single strand scission unravels the supercoiled DNA (form I) to a relaxed circular one (form II), while a second scission on the complementary strand, within about twelve base pairs from the first one, generates a linear DNA molecule (form III). These three DNA forms can be easily separated and quantified by gel electrophoresis (Figure 25), which allows easy detection of even a small number of scission events.

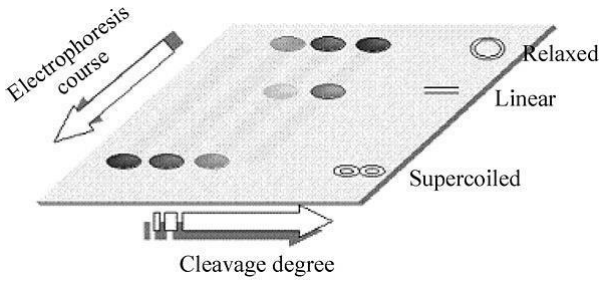

Figure 25. Schematic analysis of the plasmid DNA cleavage by electrophoresis gel.

1.5.1 Monometallic complexes

Mancin and coworkers[32] performed a systematic study of the influence of ligand structure on the reactivity of monometallic Zn(II)-based complexes towards the hydrolysis of the DNA-model substrate, BNP. They compared tri- and tetradentate polyamine ligands and the conclusion was that tretradentate ligands were ineffective catalysts due to the saturation of four of the five binding position of the metal ion, not leaving space to the coordination of the substrate and the nucleophile, a water/hydroxide molecule. Between tridentate ligands, cyclic ligands which have a facial or tripodal coordination shown to be more reactive than linear ligands. Certainly, this is the coordination geometry that Zn(II) has in

the active site of hydrolytic enzymes. The two ligands (Figure 26) that produce the most reactive complexes are 1,4,7-triazacyclononane ([9]aneN$_3$) and the 1,5,9-triazacyclododecane ([12]aneN$_3$), similar case than with HPNP.

Figure 26. Zn(II) complexes of a) 1,4,7-triazacyclononane, and b) 1,5,9-triazacyclododecane.

One strategy to enhance the reactivity of monometallic complexes towards hydrolysis of BNP is the insertion of the nucleophile on the ligand structure. Chin and coworkers[33] reported a series of Cu(II) and Zn(II) ligands that incorporates an alcohol group to act as nucleophile. In the case of the Zn(II)-based catalyst (figure 27a), the rate enhancement obtained is one order of magnitude with respect to the non hydroxide analog. Unlikely, the product of the transesterification is a stable phosphorylated ligand which means that such complexes are not catalytic. Figure 27 shows the best performing ligand, due to the presence of two hydrogen bond-donating amino groups and the hydroxypropyl arm as a nucleophile. The Zn(II) complex achieve one million-fold acceleration in the cleavage of BNP over the background reaction at pH 7 and 25 °C.

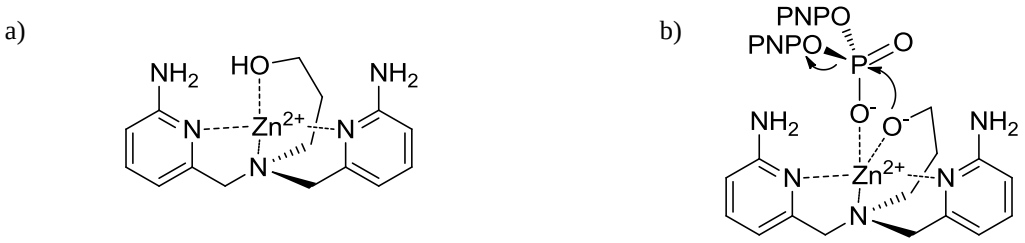

Figure 27. a) Zn(II) complexes of 3-(bis((6-aminopyridin-2-yl)methyl)amino)propan-1-ol b) proposed reaction mechanism for the hydrolysis of BNP (H-bond not shown for clarification).

A possible solution to this problem was recently reported by Williams and coworkers[34]. The introduction of a hydrated aldehyde into the ligand structure provides turnover to the catalyst. Interesting enough, they proposed that the hydroxide acting as a nucleophile is the one not coordinated to the metal ion. In the ligand presented in figure 28 the amine

subtituents were substituted for methyl groups, which allow us thinking that this catalyst can be further improved.

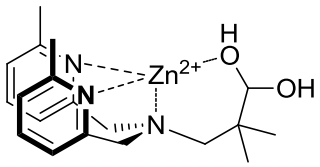

Figure 28. Zn(II) complex of a pyridyl derivative bearing a germinal diol.

1.5.2 Bimetallic complexes

In 1995, Breslow and coworkers[35,36] reported for the first time the hydrolytic activity of a series of Zn(II) complexes towards different phosphate esters, including BNP. Such complexes were prepared by connecting a tridentate macrocyclic ligand with different spacers. The outcome of the work was that when flexible linkers were used, the reactivity of the bimetallic system was the same as that of the monometallic analog. However, when rigid spacers were used better activity was reached. In particular, the best performing system was the one with a 4,4'-biphenyl linker (Figure 29) which cleaved BNP with a pseudo-first order rate of 6.4×10^{-6} s^{-1}, an acceleration of about 2000 times over the backgroup reaction at pH 8.36 and 55 °C (20% DMSO).

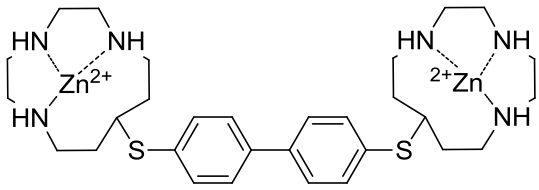

Figure 29. Bimetallic Zn(II) complex of 1,4,7-triazacyclododecane connecting by a 4,4'-biphenyl linker.

Another example of the used of rigid spacers to connect metal binding moieties was reported by Lippard and coworkers[37]. The Zn(II) complex prepared using a 2,7-bis[2-pyridy- lethyl)aminomethyl]-1,8-naphthyridine ligand (BPAN, Figure 30) was able to cleave BNP with a 9200-fold acceleration over the uncatalyzed reaction at pH 7 and 40 °C. However the acceleration over the monometallic model was only 1.8-fold.

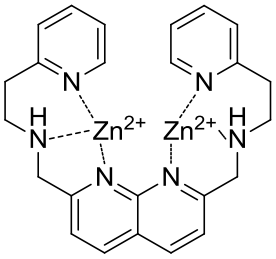

Figure 30. Bimetallic Zn(II) complex of 2,7-bis[2-pyridy- lethyl)aminomethyl]-1,8-naphthyridine (BPAN).

The use of 1,4,7-triazacyclononane ([9]aneN_3) as ligand for connecting Zn(II) by different semi-rigid spacers as 2,20-dimethylbipyridine, 1,10-bi- methylphenantroline and 2,3-bimethylquinoxaline was reported by Bencini and coworkers[38]. The complex of quinoxaline derivative ligand (figure 31) was the most reactive in the transesterification of BNP at pH 7 and 35 °C with a pseudo-first order rate of 2.1×10^{-8} s^{-1} which means an 350-fold acceleration over the background reaction.

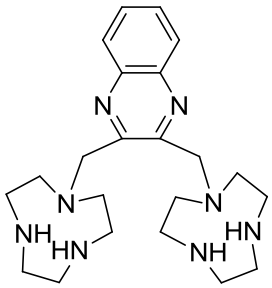

Figure 31. Metal ligand of two 1,4,7-triazacyclononane connected by a quinoxaline linker.

Such complexes are very poor reactive systems when DNA is the substrate. An interesting strategy to improve their reactivity consists to increase the affinity of these artificial nucleases through conjugation with DNA binding units, like the use of intercalators.

1.5.3 Supramolecular architectures

Mono and dimetallic Zn(II) complexes are very poor reactive systems when DNA is the substrate. An interesting strategy to improve their reactivity consists to increase the affinity of these artificial nucleases through conjugation with DNA binding units, like the use of intercalators.

The first example of the use of an intercalator to enhance the binding of a bimetallic Zn(II) complex (in this particular case the authors also used Cd(II)) was reported by Barton and coworkers[39]. They used a ruthenium-based intercalator to prepare the catalytic system (figure 32) which was quite efficient in cleaving DNA. After 5 h at 37 °C and pH 8.5, 40% of the supercoiled form was degraded in the presence of 7mM of catalyst, which corresponds with an estimated rate constant of 3×10^{-5} s^{-1}.

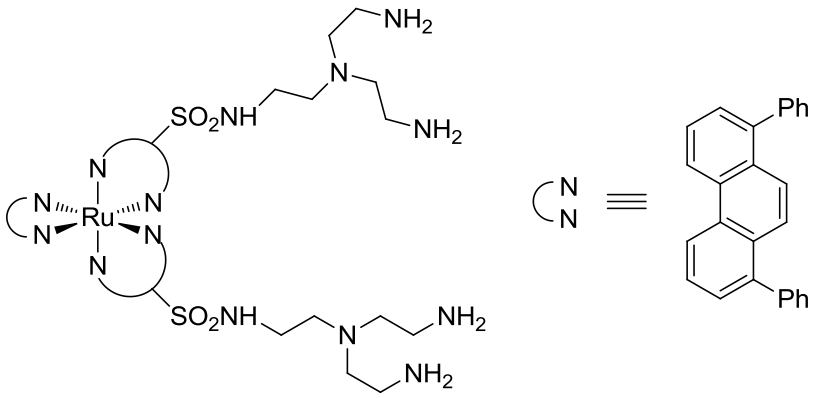

Figure 32. DNA hydrolytic agent containing ruthenium intercalator.

Not always the use of an intercalator enhances the reactivity of the catalytic systems as nicely demonstrated by Tonellato and coworkers[40]. The authors prepared a series of cis–cis- triaminocyclohexane–anthraquinoneintercalator conjugates- ligands, linked by alkyl spacers of different length (Figure 33). The study of the reactivity of such ligands with Zn(II) towards supercoiled DNA showed that when the spacer is the C8alkyl, the complex is 15-fold more efficiently than the Zn–triaminocyclohexane complex lacking the anthraquinone moiety. However, in the case of the shortest spacer (C4) no cleavage was observed which point out the incorrect position of the reactive group. This work indicates

the importance of DNA cleaving efficiency on the accurate position of the reactive group which depends on the spacer length.

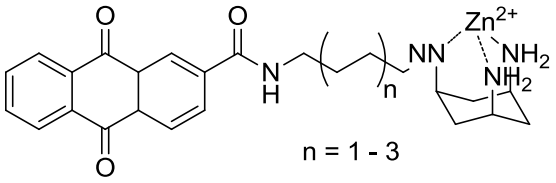

Figure 33. Anthraquinone Zn(II)-TACH complex conjugates.

Another reason for the scarce reactivity of bimetallic complexes towards DNA is the fixed distance between metal ions in pre-organized ligands which leaves no freedom for adaption to the reaction requirements. One strategy to reduce this structural limitation is the use of supramolecular self-assembly systems, such a metallic nanoparticles or micelles.

The first example reported of catalytic gold-nanoparticles able to cleavage BNP and plasmid DNA was reported by Mancin and coworkers[41]. They synthetized gold-nanoparticles functionalized with thiols bearing the metal-binding moiety BAPA, bis-(2-amino-pyridinyl-6- methyl)amine (Figure 34). Although the reactivity of the Zn(II)-based nanoparticles was not very high (rate constant of 2×10^{-6} s^{-1} at 37 °C, pH 7 and 15 μM complex concentration) the nanoparticles were found to promote double strand cleavage with direct conversion of the supercoiled DNA to the linear form.

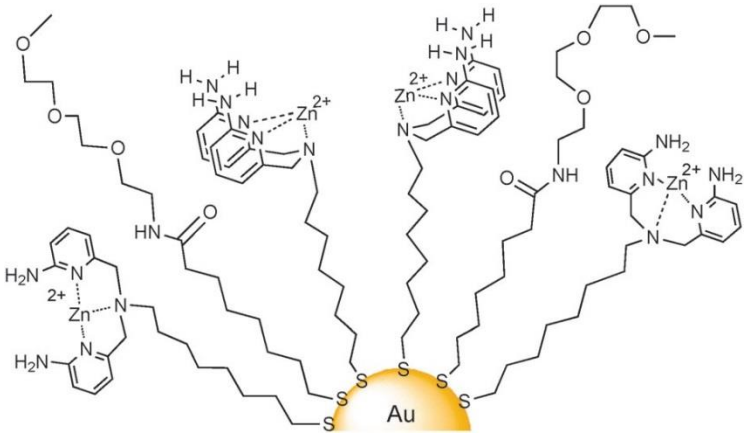

Figure 34. DNA hydrolytic catalyst based on functionalized gold nanoparticles.

The reactivity of mono and dimeric lipophilic Zn(II) complexes of the 1,4,7,10-tetraazacyclododecane ([12]aneN$_4$) derivatives in micelles or vesicles (Figure 35) was studied by König and coworkers[42]. Both supramolecular assemblies are very active towards BNP, but moderate reactivity was reached toward plasmid and also single strand DNA. The high reactivity obtained is explained on the basis of high local concentration of metal ions able to cooperate and on the decreased polarity at the interface between the reactive systems and water, which enhance the nucleophilic attack on the phosphodiester substrate. However, the use of tetradentate ligands is quite surprising since they are less reactive than the tridentate ones, maybe this fact is overcome since one of the N donor is a terciary amine.

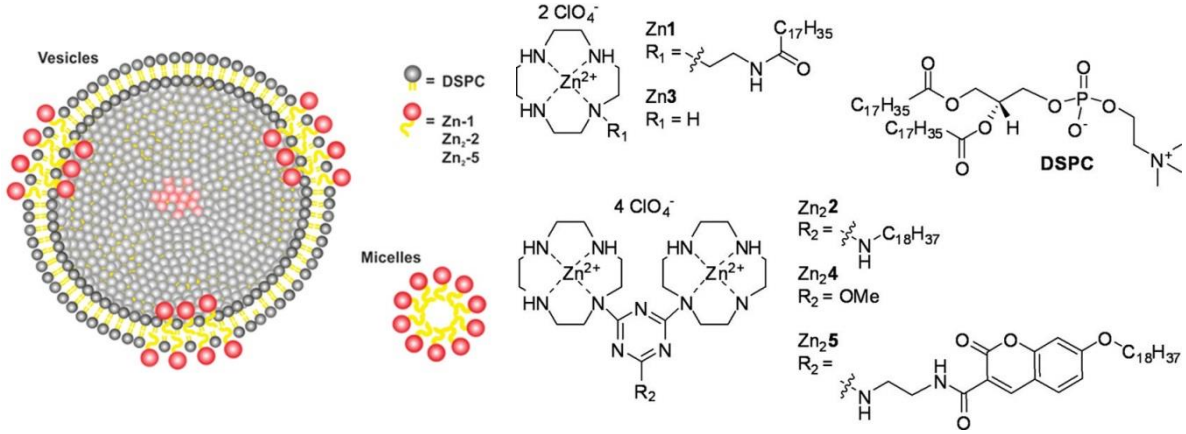

Figure 35. Zn(II)-complexes and Vesicular/Micellar catalystic systems

Previously, it was mentioned that the heptapeptide-based catalyst (figure 32 a and b) reported by Scrimin and coworkers[28] is able not only to cleavage HPNP but also to perform the cleavage plasmid DNA. Indeed, the system cleaves the second substrate with a first order rate constant of 1.0×10^{-5} s^{-1} at pH 7.0, 37 °C and 3.6 μM complex concentration. Although the intermetallic distance (6 Å) is larger than the one found in hydrolytic enzymes, the system is about 20 times more reactive than its monometallic model. The high cooperativity observed is justified by the authors who proposed that the heptapeptide-based catalyst binds to DNA by inserting the two macrocycles within three adjacent phosphate groups (figure 36c). This situation forces the central phosphate to

interact with both metal ion complexes and, as a consequency, the system takes advantage of cooperativity between the two catalytic centers.

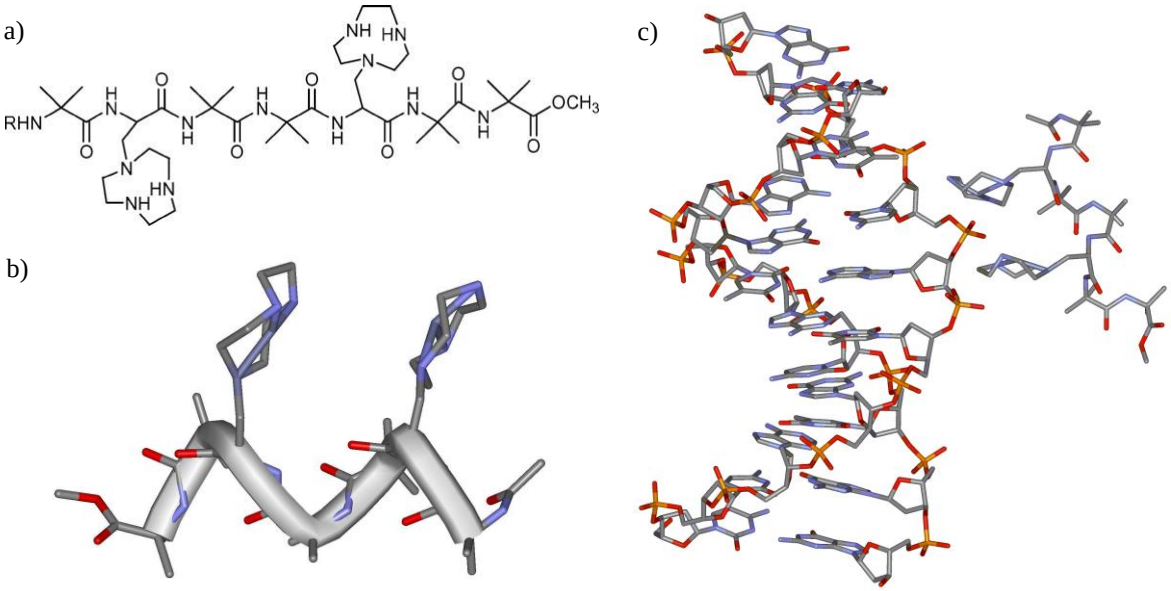

Figure 36. a) Linear structure and b) tridimensional configuration of the heptapeptide-based ligand. c) Supramolecular interaction with DNA.

1.5.4 Sequence-selective artificial desoxyribonucleases

Without doubt, the most efficient sequence-selective system for DNA have been created by Komiyama and coworkers[43,44]. They prepared a protocol namely chemistry-based DNA cutter (ARCUT, Figure 37) which consists of: 1) a Ce(IV)-EDTA complex which performs the DNA hydrolysis, and 2) a pair of pseudo-complementary peptide nucleic acids (pcPNA). The system is based in the unusual selectivity of the Ce(IV)-EDTA complex for cleaving single stranded DNA (ssDNA), which is 100-fold higher than for double stranded DNA (dsDNA). The EDTA-complexed cerium, because of its lower Lewis acidity has less affinity for DNA than the free ion and, consequently, requires the chelate binding by at least three DNA phosphate groups, a situation that can be only found in ssDNA due to its higher flexibility.

In the ARCUT protocol, the first step in the generation of gaps in the dsDNA which are formed by invasion of two pseudo-complementary PNA strands (pcPNA), whose

sequences are selected in order to bind laterally shifted base sequences in the target. The second step is the incubation with Ce(IV)-EDTA complexes which cleave the two single strand portions previously formed.

Nicely, this system does not present any kind of sequence selectivity restrictions since it can be adapted to the DNA sequence substrate. Moreover, the cleavage event does not occur in the presence even of a single base mismatch.

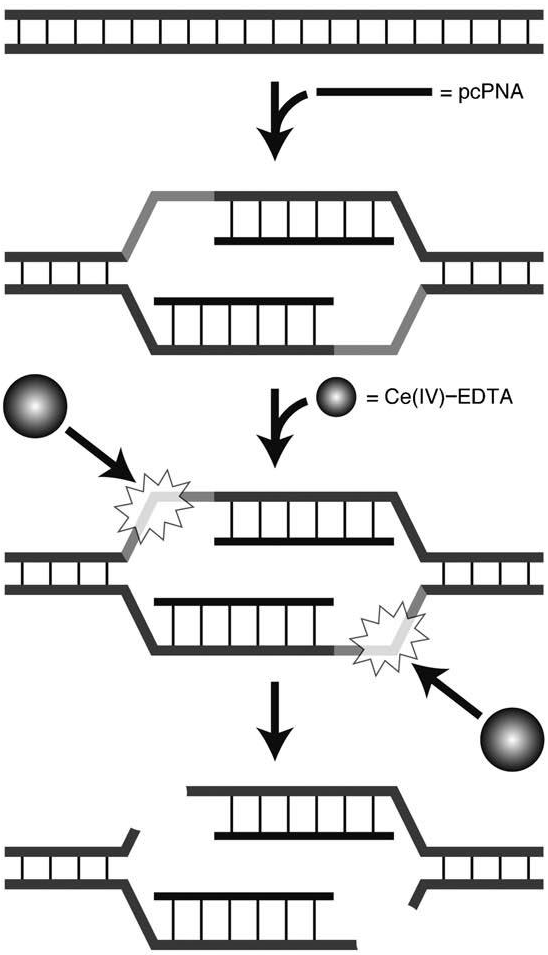

Figure 37. Schematic representation of the chemistry-based DNA cutter (ARCUT) protocol.

1.6 Nanotechnology

In 1959, Richard Feynman gave a seminar at the American Physical Society meeting at Caltech entitled "There's Plenty of Room at the Bottom" in which he hypothesized with the possibility of direct manipulation of individual atoms and molecules to achieve better chemical systems than those at that time. This lecture is considered to be the germ of the actual nanotechnology since inspired the conceptual beginnings of the field decades later.

Nanotechnology is defined as the manipulation of matter with at least one dimension sized from 1 to 100 nanometers (figure 38). Certainly, such a degree of operation was not possible without the development of the powerful tools and techniques at the nanometer size, as the atomic force microscope (AFM), the scanning tunneling microscope (STM) or the transmission electron microscope (TEM), that allows us to monitor the matter at the atomic scale.

The field of nanotechnology is as broad, from polymer science to metal noble nanoparticles, as fascinating, since allow us a better knowledge of the forces that govern the nature at the nanometer scale. Hence, we focus our attention in the synthesis, characteristics and possible applications of gold nanoparticles since is the subject of the present thesis.

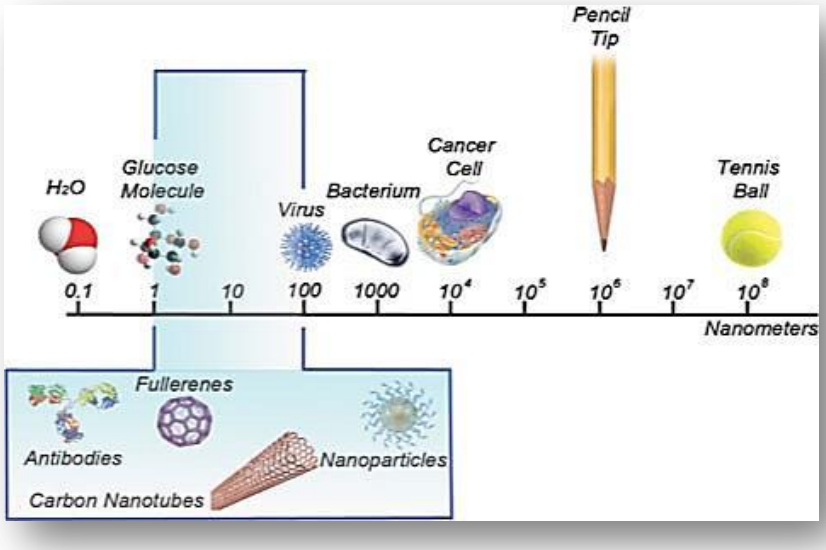

Figure 38. Nanometer scale.

1.7 Gold-nanoparticles

1.7.1 Synthesis

The first study of the nucleation and growth processes in the synthesis of colloidal gold was reported by Turkevich and coworkers[45] in 1969. In this method, sodium citrate was used as reducing agent of the tetrachloroauric acid and as capping agent of the prepared spherical gold nanoparticles. However, the control of the monodispersity was low.

Decades later, in the early 90s, Brust and Schiffrin[46] reported a new synthetic method to produce gold nanoparticles in organic liquids, like toluene. In the first step of this method, gold(III) ions are transferred to the organic solution by using the tetraoctylammonium bromide (TOABr) as transfer agent, then the gold(III) ions are reduced with sodium borohydride in the present of alkanethiols, which form strong Au-S bonds that stabilized the gold nanoparticles.

Later on, Peng[47] and Scrimin[48], independently, reported a 2-step synthesis in which the reduction of the gold(III) ions is done in the presence of amines as stabilizing agents. We adopted the Scrimin method to synthesize the gold nanoparticles used in the present thesis and for this reason, we will describe this synthetic method accurately (Figure 39).

In the first step of the synthesis an aqueous solution of tetrachloroauric acid is mixed with toluene using tetraoctylammonium bromide to transfer the gold(III) ions obtaining areddish-orange organic solution. Then dioctylamine is added, which has two functions, the first one is to reduce the gold from III to I (a colourless solution is obtained) and second one is to stabilize the gold-nanoparticles once formed. Furthermore, the amount of dioctylamine dictates the dimensions of the colloidals. Sodium borhydride is used to reduce the gold(I) ions to gold. In the second step, the desired thiols are added to the solution of dioctylamine-stabilyzed gold nanoparticles.

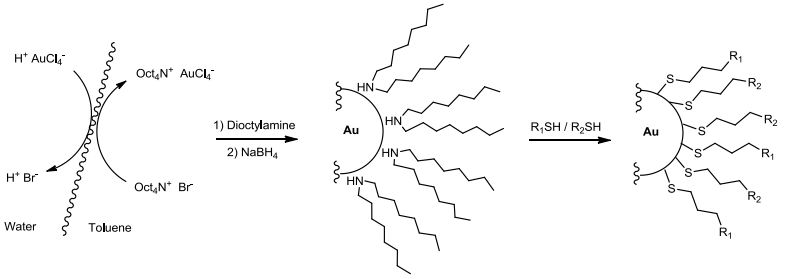

Figure 39. Schema of the two-step gold-nanoparticles synthesis.

The advantages of this method with respect to the Brust-Schiffrin one lie on the use of the amine as stabilizing agent. First, the ratio of gold:dioctylamine allow us to control the size of the sample. Second, the thiols are added in the second step in mild conditions, which allow to preserve the functionalities these molecules. Third one, no excess of thiols is needed which allow a better ratio control in the formation of mixed-monolayer nanoparticles.

All these synthetic methods present the inconvenience of scale-up and automatize, for these reason, in the last years different methodologies have been developed based in milli- and micro-fluids. Unlikely, this technology is still far for being applicable to large scale synthesis.

1.7.2 Properties

It is fascinating to see how by using the right conditions and reagents we obtain highly self-organized systems starting by a mixture of component, gold(III) ions and the thiols.

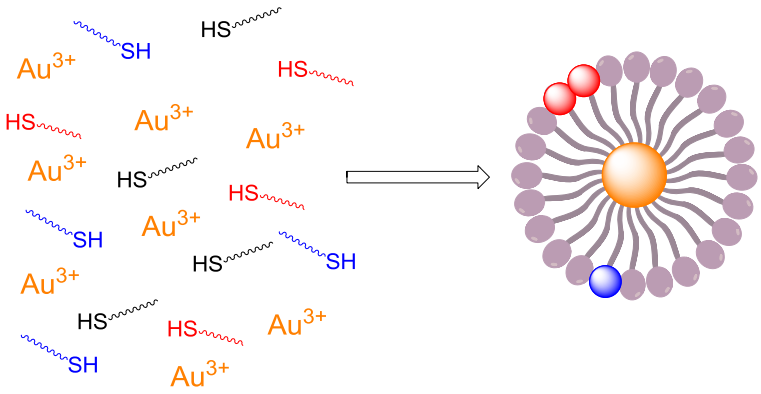

Figure 40. Schema of the self-organization of gold nanoparticles

Within the nanoparticle we can distinguish at least three levels of organization: 1) the gold core, 2) the Au-S bonds at the nanocore surface and 3) the organic monolayer formed by the stabilizing molecules.

At the nanoscale dimension the properties of gold are totally different from the bulk material. Indeed, gold-nanoparticles do not present a goldish colour, they present instead a range of colours depending on the core dimension due to the shifting and broadening of the plasmonic band at 520 nm towards longer wavelengths (Figure 41)[49].

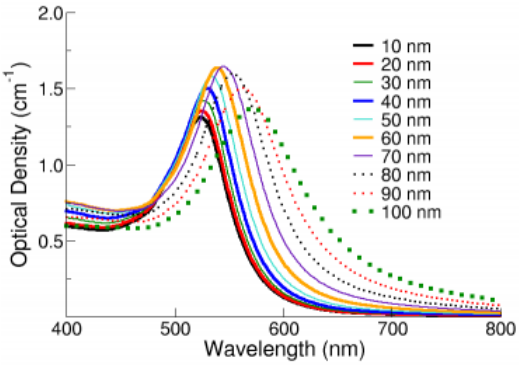

Figure 41. Extinction spectra of gold nanoparticles with diameters ranging from 10 – 100 nm.

Such optical properties of the gold nanoparticles depend on their small size and metallic nature. A gold nanoparticle can be pictured as a lattice of positive gold ions surrounded by a cloud of mobile conduction electrons. When an external light (electric) field is applied, it perturbs the mobile conduction electrons inducing surface polarization charges (the cloud is displaced to one side). The electrostatic attraction between the positive gold ions and the negative electrons (Coulomb law) provides a restoring force that originates a collective oscillation of the electron cloud. In this way, depending on the metal first, and then on the size and shape of the nanoparticle, it can strongly absorb light at a specific resonance frequency.

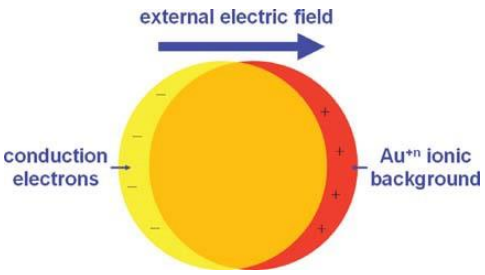

Figure 42. Schematic representation of a dipolar plasmon oscillation in a gold nanoparticle.

Another interesting property of the gold core is that it acts as a fluorescence quencher, the smaller is the diameter size the strong is the quenching[50]. Both properties of gold core, plamon and fluorescence quenching, have been cleverly applied to produce detection tests based on gold nanoparticles.

The second level of organization corresponds to the gold core surface where the sulfur atoms are bound to the gold atoms (Figure 43). Thanks to the first X-ray crystal structure of monolayer-protected clusters (MPC) it was possible to see that the interaction between the molecules and the gold core is through a thiolate-Au(II)-thiolate motiv. Gold (I) atoms come out from the lattice of gold (0) atoms forming staples to interact to the sulfur atoms after losing their proton[51].

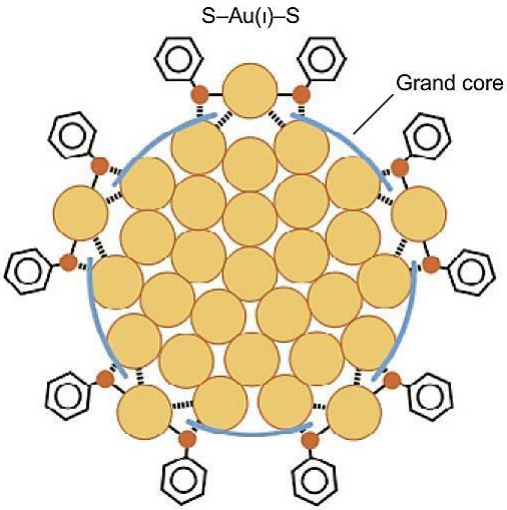

Figure 43. Schematic representation of a monolayer-protected gold cluster.

The last level of organization is the formation of the organic monolayer, which principal properties are: multivalency, multifunctionality, self-organization and cooperativity. Indeed, the gold core serves as a scaffold and can be coated with different numbers functional thiols (multivalency and multifunctionality). By choosing the right thiol structures we can tune they organization on the monolayer creating patches, stripes or random distribution (self-organization). And, finally the molecules are in close proximity which allow them the possibility to cooperate.

1.7.3 Applications

Due to the small size of gold nanoparticles, within the virus range, their applications in biology increase every year. They can be used as drug/gene delivery systems and also for sensing of small ion to big molecules as DNA.

An example of gene delivery was reported by Rotello and coworkers[52] who synthetized 2-nm gold nanoparticles functionalized with thiols bearing a photoactive group which is an *o*-nitrobenzyl ester derivative. Near-UV irradiation releases the positively charged amine from the nanoparticle surface, as a consequence, the nanoparticle remain negatively charged because of the carboxylic groups (Figure 44b). DNA bound to positive nanoparticles can be delivered into the cell, once inside the system is irradiated, the nanoparticles become negative and the DNA is released in the cytosol. Then it can go into the cell nucleus (Figure 44a).

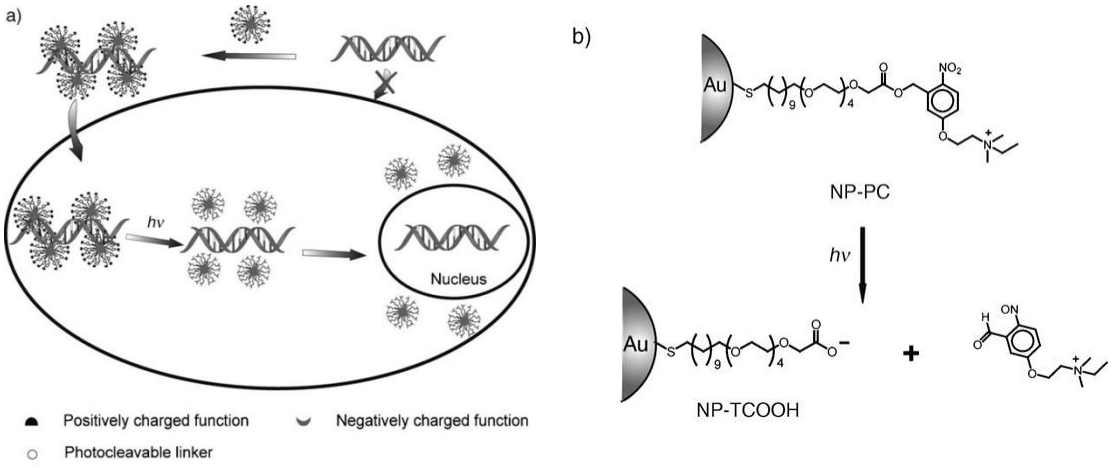

Figure 44. a) Schematic representation of the release of DNA within the cell. b) Schematic illustration of the light-induced cleavage of the photoactive group.

One interesting DNA assay based on quenching ability of gold nanoparticles was reported by Libchaber and coworkers[53]. In this approach, a fluorescence dye is close to the nanoparticle surface due to the hairpin structure of the DNA attached to the nanoparticle so its fluorescence is quencher. In the presence of the target DNA, which hybridized with the complementary DNA, the hairpin structure opens up and, as a consequence, the fluorescence dye is far enough from the gold core to emit light (figure 45).

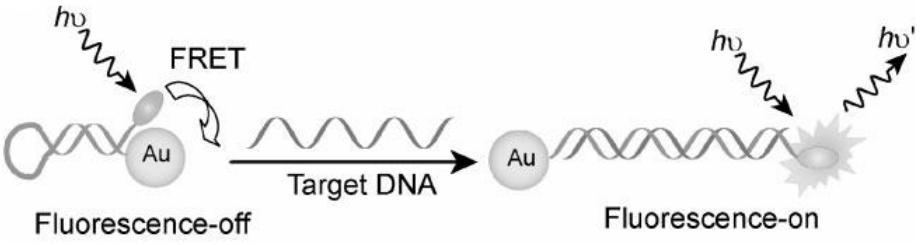

Figure 45. Schematic representation of DNA-detection assay.

On the other hand, gold nanoparticles have attracted a lot attention to self-organized catalytic units on their surface because of their dual behavior. They can be considered as homogenous catalyst since the active site is in direct contact with the bulk solution but at the same time as heterogenous catalyst since the nanoparticles can be easy recover by filtration.

Jacobsen and coworkers[54] created a new generation of catalysts by the incorporation of chiral salen ligands into self-assembly monolayer (SAM) on 3.4 nm-diameter gold nanoparticles, mixed with alkanethiols (Figure 46a).

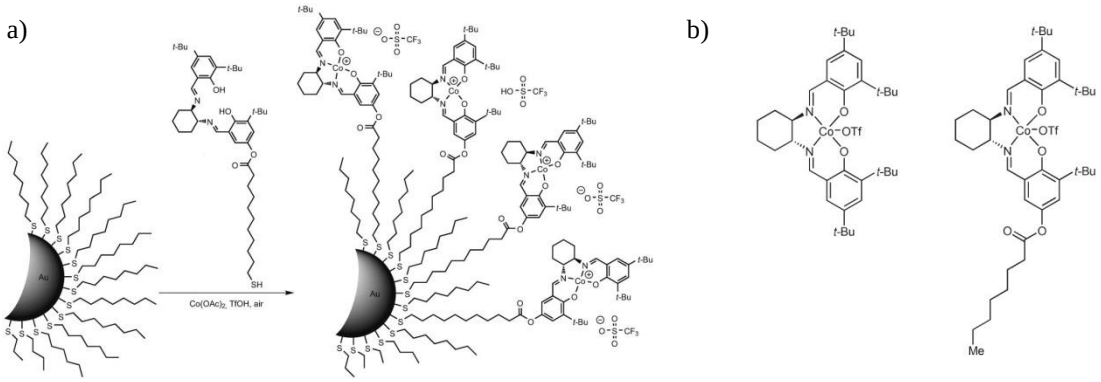

Figure 46. a) Nanoparticle-based catalyst and b) monomer analogs.

They study their catalytic activity in the hydrolytic kinetic resolution (HKR) of hexane-1-oxide. They observed high selectivity and rate accelerations (Figure 47) in comparison with the homogeneous monomeric catalyst (Figure 46b). Moreover, the system show turnover (seven cycles) because it was possible to recovery the nanoparticles by filtration, re-oxidate the catalytic units an repeat the catalytic cycle without losing enantioselectivity and reactivity.

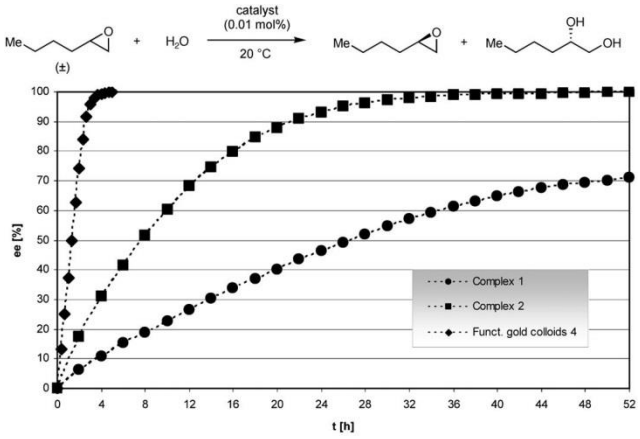

Figure 47. Comparison between the catalysts.

Chapter 2

PHOSPHATE CLEAVAGE BY SMALL ENTITIES

2.1 Overview

A deeply understanding of the roles play by the metal ion, in this particular case by Zn(II), in promoting the hydrolytic cleavage of phosphate esters can be achieved by the use of small mono- or bi-metallic complexes[55]. In particular, we have studied the catalytic activity of mono-metallic complexes towards the hydrolysis of HPNP and BNP, a RNA model substrate and a DNA model substrate, respectively.

Mono-metallic complexes produces acceleration sensibly lower than the related bi-metallic complexes because they huge benefit arising from metal centers cooperation but, these simple models allow more detailed study of the phosphate cleavage reaction since they provide the most simplified system possible.

Notably, since Zn(II) belongs to the group 12 of the periodic table, it is a peculiar transition metal ion featuring filled *d* orbitals but empty outer shell s orbitals. The primary consequence of this electronic configuration is that Zn(II) has no ligand field stabilization energy and, as a result, it can easily adapt, without any additional energy cost, its coordination geometry.

In this chapter, we show how using different ligands for the formation of two complexes (**1** and **2**) which modify the coordination of Zn(II) affects the HPNP cleavage reaction with effects never reported before. In a separate project, we also investigate the possible effects of the introduction of a hydrated aldehyde inpyridine-based ligand (complex **3**) to obtain turnover in the cleavage reaction of BNP.

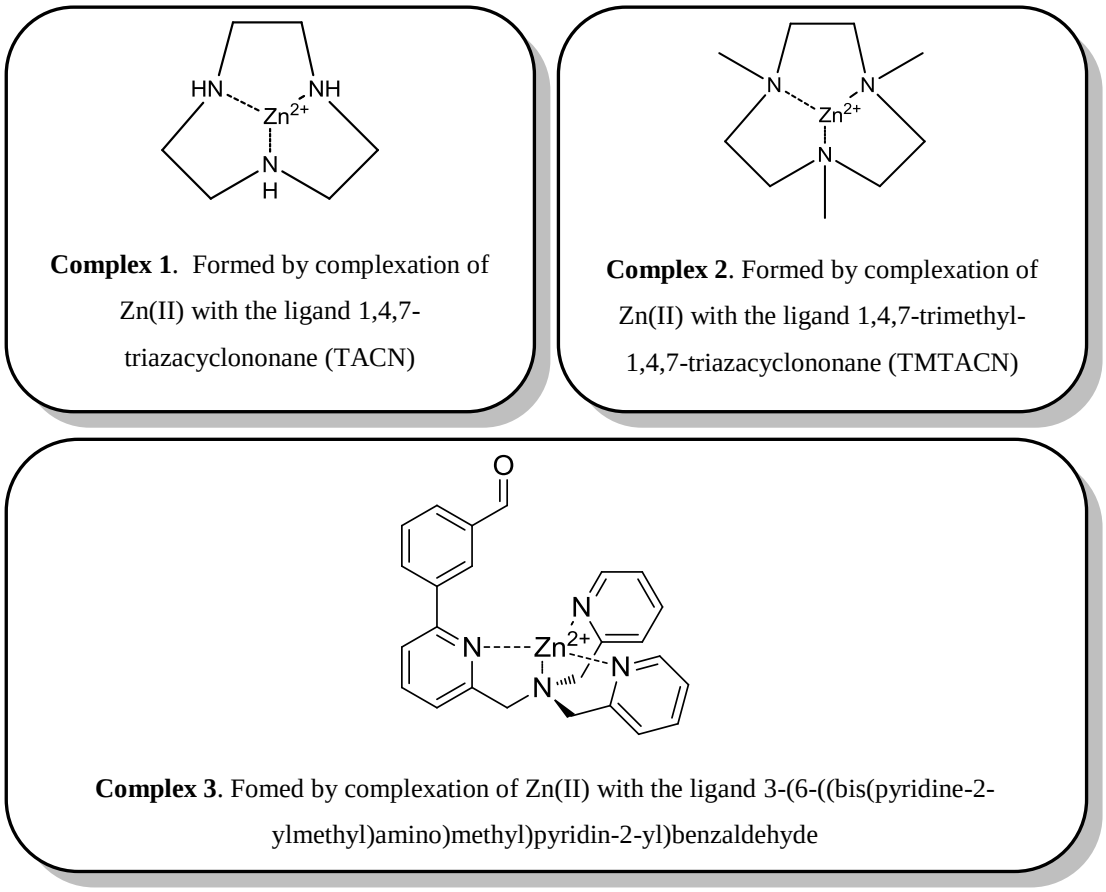

Complex 1. Formed by complexation of Zn(II) with the ligand 1,4,7-triazacyclononane (TACN)

Complex 2. Formed by complexation of Zn(II) with the ligand 1,4,7-trimethyl-1,4,7-triazacyclononane (TMTACN)

Complex 3. Fomed by complexation of Zn(II) with the ligand 3-(6-((bis(pyridine-2-ylmethyl)amino)methyl)pyridin-2-yl)benzaldehyde

Figure 48. Zn(II) complexes studied in the present chapter.

2.2 HPNP cleavage by mono-metallic Zn(II) complexes

The reactivities of Zn(II) complexes with 1,4,7-triazacyclononane (TACN, Complex **1**) and its methyl derivative 1,4,7-trimethyl-1,4,7-triazacyclononane (TMTACN, Complex **2**) towards the hydrolysis of phosphates were expected to not show strong differences apart from the ones related to the use of tertiary amines instead of secondary amines as ligands donor groups.

However, it was very surprised to find quite a different behavior of the Zn(II) complexes with TACN and TMTACN, complex **1** and **2**, respectively. This behavior can be only explained by a different coordination sphere of the Zn(II) with these different ligands.

2.2.1 Kinetics studies

The reactivity of the Zn(II) complex **1** and **2** was analyzed towards the cleavage reaction of the RNA model 2'-hydroxy-p-nitrophenyl phosphate (HPNP). The binding constant of phosphate diester to mononuclear Zn(II) complexes are quite low, in the molar range, and, consequently, the catalytic process follows usually a second order rate law. To simplified the kinetic studies we decided to work in the "so-called" pseudo-first order conditions, where the concentration of substrate is much lower than the catalyst one. In this condition the catalyst concentration may be considered constant though the whole reaction and the reaction depends only on the substrate concentration.

$$substrate + catalyst \rightarrow product + catalyst$$

$$v = k_2[substrate][catalyst]$$

Experimental conditions:
[substrate]= $2 \cdot 10^{-5}$M
[catalyst]= $5 \cdot 10^{-5}$M - $4 \cdot 10^{-4}$M

$$v = k_{\psi}[substrate] \qquad (1)$$

Finally, the pseudo-first and the second order rate constants are related by the following equation:

$$k_w = k_2[cat] + a \qquad (2)$$

Of course, such second rate constant does not indicate the occurrence of a true bimolecular process but is still related to a Michaelis-Menten-like mechanism working in non saturation conditions. Hence, $k_2 = k_{cat}/K_M$ but the two relevant values of k_{cat} and K_M cannot be measured independently.

2.2.2 Dependence of reaction rate with pH

The rate constants obtained show a strong influence of the pH with both complexes but, interestingly enough, the behavior of the two complexes is completely different. In the case of complex **1**, the profile follows a bell-shape characteristic of penta-coordinated Zn(II) complexes with two metal bound water molecules. Indeed, the first deprotonation has a positive influence in the reaction rate, due to the generation of a OH group bound to the metal ion that promotes the deprotonation of the OH group of the substrate. On the other hand, the second deprotonation has a negative influence since the formation of a second hydroxide strongly bound to the metal ion saturates the coordination sphere of Zn(II), as a consequence, inactivates the catalyst because of the impossibility to replace an OH group with the substrate to form the complex substrate-catalyst.

Remarkably, the profile of complex **2** does not follow the expected bell-shape. Bellow pH 9.5 the reactivity is similar and even lower to that of complex **1**. In this interval, k_2 is slightly increasing suggesting that a deprotonation with the formation of a more reactive species is occurring also in this case, but that the reactivity of this species is similar or slightly lower than that of the monodeprotonated species formed by complex **1**. However, when the pH reaches the value of 9.5, a strong reactivity increase is observed and k_2 reaches values 4-fold greater than the maximum one reached by complex **1**.

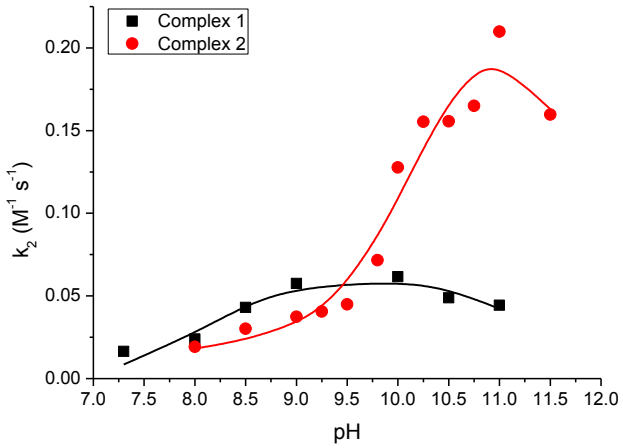

Figure 49. pH rate profile of the second order rate constant for the cleavage of HPNP by complex **1** **(**TACN-Zn(II), black) and by complex **2 (**TMTACN-Zn(II), red). Conditions: [HPNP] = 2.0×10^{-5} M, [buffer] = 5.0×10^{-2} M. Solid lines are from fitting of equation (3) for complex **1** and equation (4) for complex **2**.

To get more insight on this peculiar behavior, we fitted the data reported in figure 48 for complex **1** with the equation (3) which was written (vide infra) for a species with three deprotonation states where only the second one is reactive. Interpolation provided hence the values of 8.10 and 11.3 respectively for the first and second pK_a, which can be attributed to the two water molecules coordinated to the metal ion. Moreover, the second order rate constant for the reaction of the active species of the catalyst and the substrate is 0.062 M^{-1} s^{-1}.

$$k_{\varphi} = k_2' \left(\frac{[TACN{\cdot}Zn(II)]_{total}}{\frac{[H^+]}{K_a^1} + 1 + \frac{K_a^2}{[H^+]}} \right) \qquad (3)$$

The values obtained are in line with the literature reports for this complex; as an instance a k_2 and pK_a^1 values of 0.065 M^{-1} s^{-1} and 8.1 respectively were reported by Mancin[32] and Scrimin[56], independently. On the other hand, the formation of the bis-deprotonated species and the consequent drop of the catalysts reactivity have never been reported for complex **1**, but this behavior is well-known for similar complexes of tridentated ligands, as 1,5,9-triazacyclododecane-Zn(II).

When applied to the data relative to the complex **2**, fitting of the data with equation 3 gives unacceptable results. On one hand, the fit of the data in the region bellow pH 9.5 is quite poor. On the other, the fitting provides a pK_a value around 10 for a the first deprotonation and above 12 for the second. Such results would imply an unlikely shift of the reactivity-pH bell-shaped profile toward much higher pH values with respect to complex **1** without giving any explanation for the reactivity behavior bellow pH 9.5.

We hence decided to fit the data with equation 4, which was written starting from a reactivity model that involves three deprotronations, with both the first and the second leading to an increase of reactivity.

Some consideration must be made about such a model, which have been so far used very rarely and only in the case of bimetallic complexes. The deprotonation of the metal bound water molecules lead to the formation of a strong ligand (the hydroxide ion) which car

hardly been displaces by the substrate. Hence, if after two deprotonation events the system is still reactive, this means that there is space enough on the metal ion to accommodate both the two hydroxides and the substrate and, consequently, that the coordination number is higher than 5, as commonly accepted for such systems. Indeed, this is possible since Zn(II) is a d^{10} metal ion with no ligand field stabilization energy, which can adapt both its coordination geometry and number to the ligands requirements. In this case, we suppose that it may be necessary to have three water molecules to complete the coordination sphere of Zn(II), and that is undisclosed the possibility of mechanistic behavior for complex **2**.

In this situation, the first deprotonation of a metal-bound water molecule produce an active catalyst with a reactivity similar to that of complex **1**, but it is the second deprotonation of the complex substantially increases the catalytic activity, as highlight for the strong reactivity increase around pH 10 reported in figure 48.

Indeed, fitting of the data obtained for complex **2** with equation 4 was satisfactory and provides the values of 7.27, 10.18 and 11.8 respectively for the first, second and third pK_a. Furthermore, it gives us also the values of the second order rate constantsfor the two active species, being 0.020 and 0.244 M^{-1} s^{-1}, respectively.

$$k_\varphi = \left[\frac{k_2'}{\left(\frac{[H^+]}{K_a^1} + 1 + \frac{K_a^2}{[H^+]} + \frac{K_a^2 K_a^3}{[H^+]^2}\right)} + \frac{k_3'}{\left(\frac{[H^+]^2}{K_a^1 K_a^2} + \frac{[H^+]}{K_a^2} + 1 + \frac{K_a^3}{[H^+]}\right)} \right] [TMTACN \cdot Zn(II)]_{total} \qquad (4)$$

Interestingly, when the reactivity of the monodeprotonated species is examined, complex 1 is slightly more reactive than complex 2, as previously reported for Cu(II) complexes of these ligands. Such lower reactivity was attributed to the electron-donating effect of the tertiary amines, which reduce the Lewis acidity of the metal ion more effectively than secondary amines. However, when the bis-deprotonated species is taken in consideration, complex **2** becomes much more reactive than complex **1** and its species is one order of magnitude more reactive than the corresponding monodeprotonated.

Table 1. Collected kinetic parameters form pH rate profiles.

Complex	pK_a^1	pK_a^2	pK_a^3	k_2^{max}(M^{-1} s^{-1})	$k_2'^{max}$(M^{-1} s^{-1})
1	8.10	11.30	-	0.062	-
2	7.27	10.18	11.80	0.020	0.244

(Conditions: [HPNP] = 2.0×10^{-5} M, [buffer] = 5.0×10^{-2} M).

2.2.3 Discussion

The profiles of second order rate constants versus pH of complex **1** and **2** (figure 48) highlight a total different behavior of these complexes towards the hydrolysis of HPNP, which can be only explained by a different mechanism of cleavage. Notably, around pH 10 where the second deprotonation occurs for both complex, in the case of complex **1** the reactivity decreases as expected for Zn(II) based catalyst coordinated to two water molecules. However, the reactivity of catalyst complex **2** suffers a remarkable increase. The catalyst is still active which demonstrates that a water molecules is still bound to the metal ion to be displaced by the substrate.

We proposed in the previous paragraph that the different cleavage pathways could indicate a different coordination sphere of the Zn(II). In this case, complex **1** should force the metal ion to have coordination 5 but while, complex **2** should induce Zn(II) to have coordination 6, as it occurs in the hydrated metal ion.

Our theory is justified by the crystal structure obtain by Spiccia and coworkers[57] for the TMTACN-Zn-PO_4^{3-} (Figure 49). Inspection of figure 3 indeed confirms that the Zn(II) ion is coordinated to the three nitrogens from the ligand TMTACN, two water molecules and one oxygen from the phosphate group.

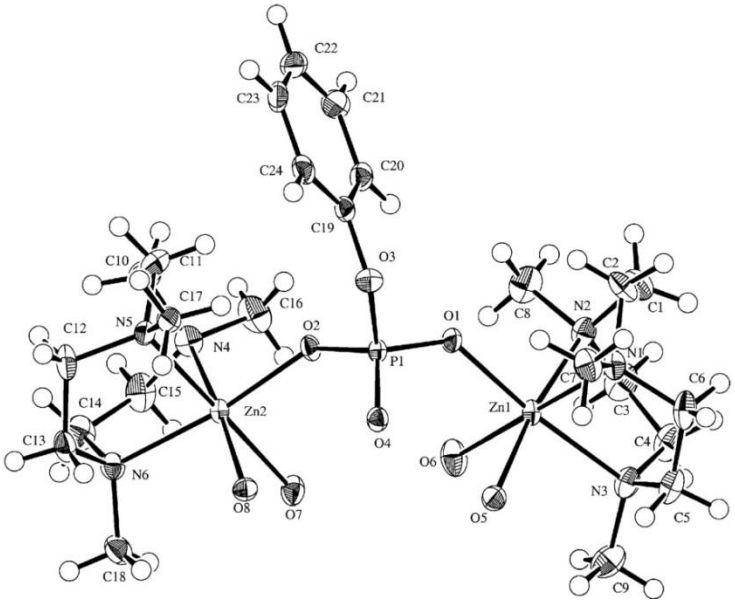

Figure 50. ORTEP plot of $[Zn_2(Me_3tacn)_2(H_2O)_4(PhOPO_3)]^{2+}$ cation with atomic labeling scheme.

To get more information on the possible coordination modes of the two complexes and their influence on their reactivity we performed some structure computational optimization of complex **1** and **2** and their potential complexes with HPNP.

Figure 51 shows active species of complex **1** coordinated to the HPNP, in which the Zn(II) ion is in a pentacoordinated configuration with the three nitrogen atoms from the ligand TACN, one oxygen from the hydroxide and one oxygen from the phosphate derivate. Remarkably, in the substrate-catalyst complex the metal-bound hydroxide is in close proximity to form H-bond interaction to the substrate hydroxide which act as a nucleophile. In such situation, the metal-bound hydroxide can activate the nucleophilicity of the 2'-OH group by a general acid/base mechanism.

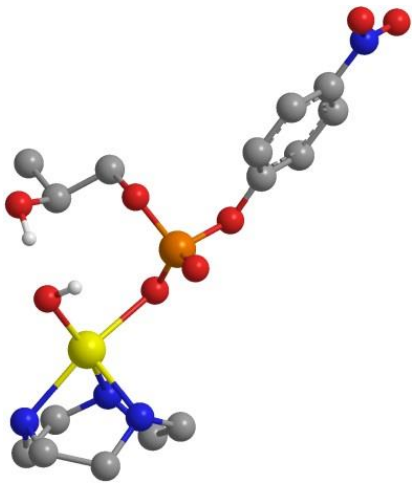

Figure 51. DFT minimization of the structure of active species of complex **1** coordinated to the HPNP ([TACN-Zn(II)(OH)(HPNP)]). Hydrogen atoms form the ligand and the substrate have been removed for clarification, except the ones of the hydroxide groups.

In the simulation of the complex **2** the nitrogen atoms from the ligand slightly coordinated the Zn(II) which means that the metal ion is almost "out" from the ligand, leaving enough free space and the possibility to the Zn(II) coordinate three molecules of water. In principle, the coordination 6 never found before for such a ligands with Zn(II) was improbable but, Zn(II) in water solution is found as a hexaacqua complex in and octoedrical coordination. We hypothesis that the ligand TMTACN substitutes 3 water molecules maintaining the octoedrical coordination around the metal ion.

Figure 52 shows the mono-deprotonated active species of complex **2** coordinated to the HPNP ([TMTACN-Zn(II)(OH)(H2O)(HPNP)]). Nicely, it shows that even when one water molecule is substituted by the sterical hindrance substrate (HPNP), there is still space for one water molecule and one hydroxide to be coordinated to the Zn(II) ion.

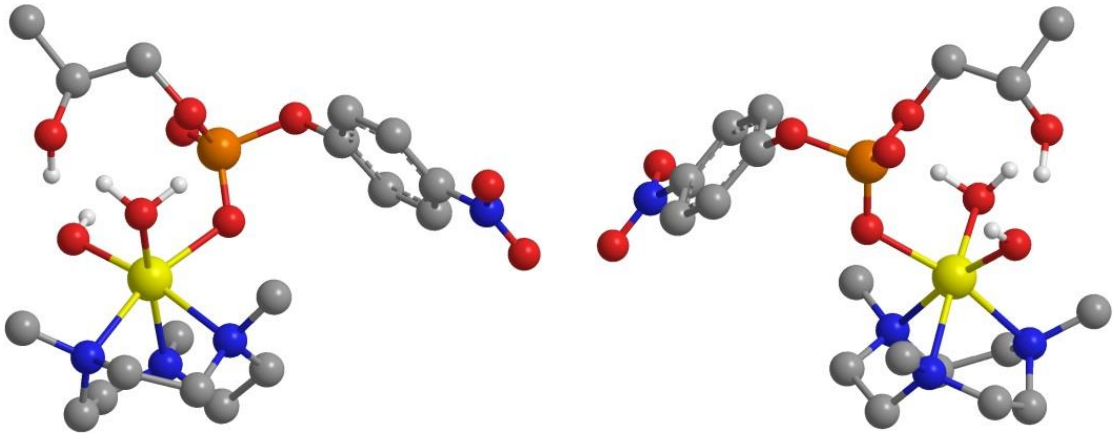

Figure 52. Two different views of the DFT minimization of the structure of the mono-deprotonated active species of complex **2** coordinated to the HPNP ([TMTACN-Zn(II)(OH)(H_2O)(HPNP)]). Hydrogen atoms form the ligand and the substrate have been removed for clarification, except the ones of the hydroxide groups and the metal-bound water molecule.

An enlargement of the previous imagines (figure 53) shows a network of H-bonds between the substrate and the metal-bound water and hydroxide molecules. Such interactions stabilize the formation of the substrate-catalyst complex and, moreover, activate the nucleophile.

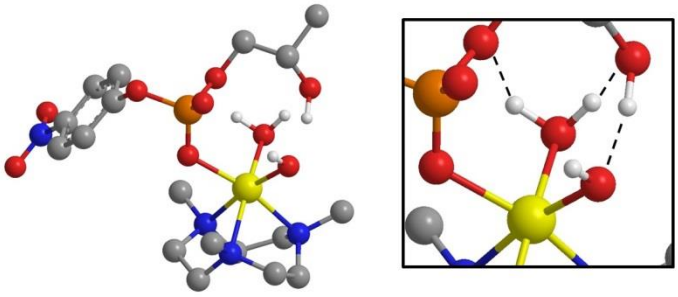

Figure 53. Enlargement of structure optimization of the mono-deprotonated active species of complex 2 coordinated to the HPNP showing the H-bond network.

The hexa-coordination can explain the increased of activity after the second deprotonation of the complex but, it cannot explain the increase of one order of magnitude between the two active species of complex 2. As commented before, at higher pHs the HPNP will be

deprotonated and, therefore, its intramolecular nucleophile will be activated. Anyway, this phenomenon is under investigation because something more should occur to explain the remarkably increase on reactivity.

As conclusion we have demonstrated that small modification in the structure of the ligands, as the insertion of methyl groups in the nitrogens binding Zn(II), modified the coordination sphere of the metal ion and, as a consequence, the catalytic pathway of the hydrolysis of HPNP.

2.2.4 Experimental procedures

2.2.4.1 Reagents

The Zn(II) ligands 1,4,7-triazacyclononane (TACN) and 1,4,7-trimethyl-1,4,7-triazacyclononane (TMTACN) were purchased to Sigma Aldrich and used without further purification.

Zn(II) acqueous solutions were prepared using $Zn(NO_3)_2$ analytical grade product and mQ water. Metal ion concentration in stock solutions were measured by atomic absorption spectroscopy using Perkin Elmer 1100 instrument.

Buffers used for kinetic experiments were used as supplied by the manufacturers: 2-morpholinoethanesulfonic acid (MES, Fluka), 4-(2-hydroxyethyl)-1-piperazineethanesulfonic acid (HEPES, Sigma), 4-(2-hydroxyethyl)-1-piperazinepropanesulfonic acid (EPPS, Sigma), 2-[N-cyclohexylamino]ethanesulfonic acid (CHES, Sigma),), 3-[cyclohexylamino]1-propanesulfonic acid (CAPS, Sigma).

2.2.4.2 Kinetics measurements

The reactions were started by adding 20μL of 1mM water solution of substrate (HPNP) to a 1-mL solution containing the appropriate buffer (0.05 M), increasing amounts of $Zn(NO_3)_2$ and of ligands TACN or TMTACN. Substrate conversion was monitored by following the absorption of p-nitrophenoxide at 400 nm using a Varian Cary 50 Spectrophotometer equipped with a thermostat cell-holder (figure 54). Pseudo-first order rate constants were obtain by fitting the increase of absorbance to the following equation (5):

$$Abs = A1 - A2 * e^{-k_w * x} \qquad (5)$$

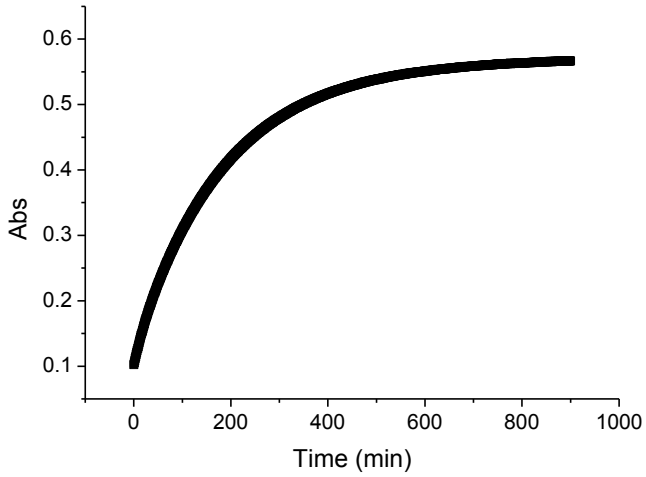

Figure 54. Example of the increase of abs vs time.

Pseudo-first order rate constants have a linear dependence with the catalyst concentration (figure 55) and allow us to obtain the second order rate constant of the reaction by fitting the data to equation 6:

$$k_w = k_2[cat] + a \qquad (6)$$

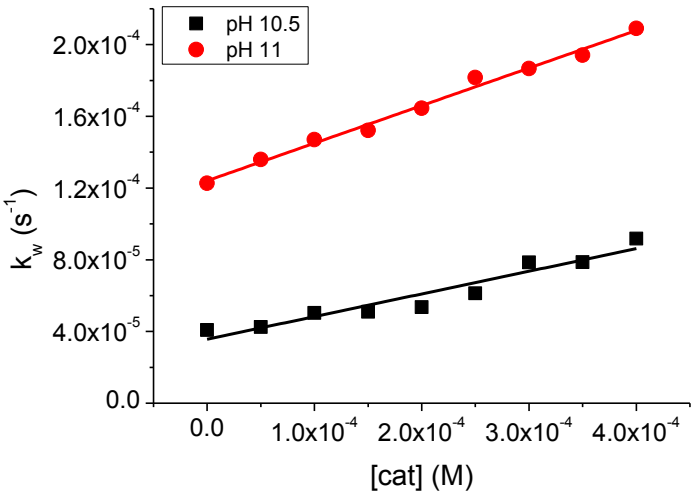

Figure 55. Example of the linear dependence of the pseudo-first order constant with the concentration of catalyst.

The following table 2 contains the values of the second order rate constant obtaining for the complex **1** and **2** at different pHs always keeping the temperature constant at 40 °C. The data here reported were used to construct the figure 49.

Table 2. Second order rate constant values for the HPNP cleavage in the presence of complex **1** or complex **2** at 40 °C.

pH	k_2[a] (M^{-1} s^{-1})	k_2[b] (M^{-1} s^{-1})
7.3	0.0165 ± 0.0007	
8	0.0244 ± 0.0016	0.0192 ± 0.0027
8.5	0.0430 ± 0.0056	0.0302 ± 0.0036
9	0.0575 ± 0.0129	0.0374 ± 0.0048
9.25		0.0406 ± 0.0041
9.5		0.0449 ± 0.0030
9.8	0.0632 ± 0.0078	0.0716 ± 0.0040
10	0.0616 ± 0.0054	0.1277 ± 0.0050
10.25		0.1554 ± 0.0072
10.5	0.0488 ± 0.0052	0.1556 ± 0.0077
10.75		0.1650 ± 0.0119
11	0.0444 ± 0.0060	0.2099 ± 0.0117
11.50		0.1597 ± 0.0161

a) Values for complex **1**. b) Values for complex **2**. (Conditions: [HPNP] = 2.0×10^{-5} M, [buffer] = 5.0×10^{-2} M).

The mechanistic pathway of complex **1** is detailed next and was used to obtaining equation (3) by applying mass balance to the catalytic mechanism of cleavage of HPNP by TACN-Zn(II) complex

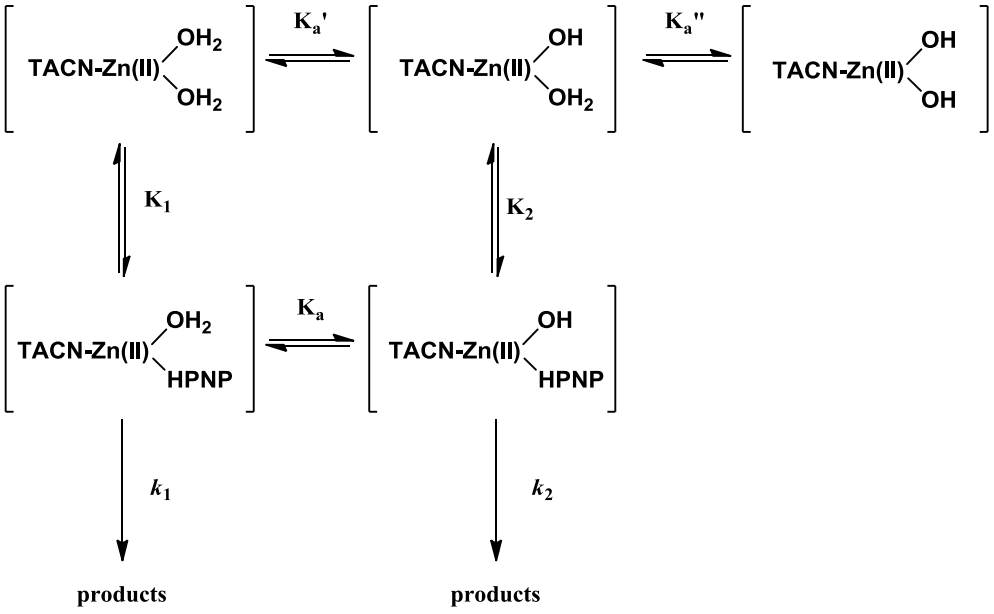

Figure 56. Scheme of the mechanism followed by the complex **1**.

Mass balances

The total amount of TACN-Zn(II) in solution is the sum of the 3 different species:

$$[TACN \cdot Zn(II)]_{total} = [TACN \cdot Zn(II) - (H_2O)_2] + [TACN \cdot Zn(II) - (OH)(H_2O)] + [TACN \cdot Zn(II) - (OH)_2] \quad (7)$$

This species are related between each other by the equilibrium of deprotonation:

$$K_a^1 = \frac{[TACN \cdot Zn(II) - (OH)(H_2O)][H^+]}{[TACN \cdot Zn(II) - (H_2O)_2]} \quad (8) \qquad K_a^2 = \frac{[TACN \cdot Zn(II) - (OH)_2][H^+]}{[TACN \cdot Zn(II) - (OH)(H_2O)]} \quad (9)$$

If we include equations 8 and 9 in the mass balance 7, we obtain the equation 10 which is a relation between the total amount of TACN-Zn(II) complex towards the active catalytic species $[TACN \cdot Zn(II) - (OH)(H_2O)]$:

$$[TACN \cdot Zn(II)]_{total} = \frac{[H^+]}{K_a^1}[TACN \cdot Zn(II) - (OH)(H_2O)] + [TACN \cdot Zn(II) - (OH)(H_2O)] + \frac{K_a^2}{[H^+]}[TACN \cdot Zn(II) - (OH)(H_2O)]$$

$$[TACN \cdot Zn(II)]_{total} = \left(\frac{[H^+]}{K_a^1} + 1 + \frac{K_a^2}{[H^+]}\right)[TACN \cdot Zn(II) - (OH)(H_2O)] \quad (10)$$

On the other hand, the reaction rate observed (k_φ) is measure by the consumption of HPNP with time:

$$k_\varphi = \frac{-d[HPNP]}{dt} = k_1[TACN \cdot Zn(II) - (H_2O)(HPNP)] + k_2[TACN \cdot Zn(II) - (OH)(HPNP)] \quad (11)$$

Where $k_1 \ll k_2$ and the concentration of catalyst-substrate complex is related to the concentration of active species$[TACN \cdot Zn(II) - (OH)(H_2O)]$by K_2:

$$k_\varphi = \frac{-d[HPNP]}{dt} = k_2(K_2[TACN \cdot Zn(II) - (OH)(H_2O)][HPNP]) \quad (12)$$

In pseudo-first order conditions: $[TACN \cdot Zn(II) - (OH)(H_2O)][HPNP] \approx [TACN \cdot Zn(II) - (OH)(H_2O)]$

$$k_\varphi = k_2'[TACN \cdot Zn(II) - (OH)(H_2O)] \quad (13)$$

Where k_2' includes the complex formation constant K_2.

Finally, we substituted equation 10 in 13 and we obtain the relation between the observed reaction rate k_φ towards the concentration of protons (equation 3) which allow us to calculate the first and second pKa of the complex TACN-Zn(II) catalyst and also the second order reaction rate between the active species and the substrate.

$$k_\varphi = k_2'\left(\frac{[TACN \cdot Zn(II)]_{total}}{\frac{[H^+]}{K_a^1} + 1 + \frac{K_a^2}{[H^+]}}\right) \quad \textbf{(3)}$$

While the mechanistic pathway of complex **2** includes another water molecule bound to the Zn(II). Equation (4) was obtain by applying mass balance to the catalytic mechanism of cleavage of HPNP by TMTACN-Zn(II) complex:

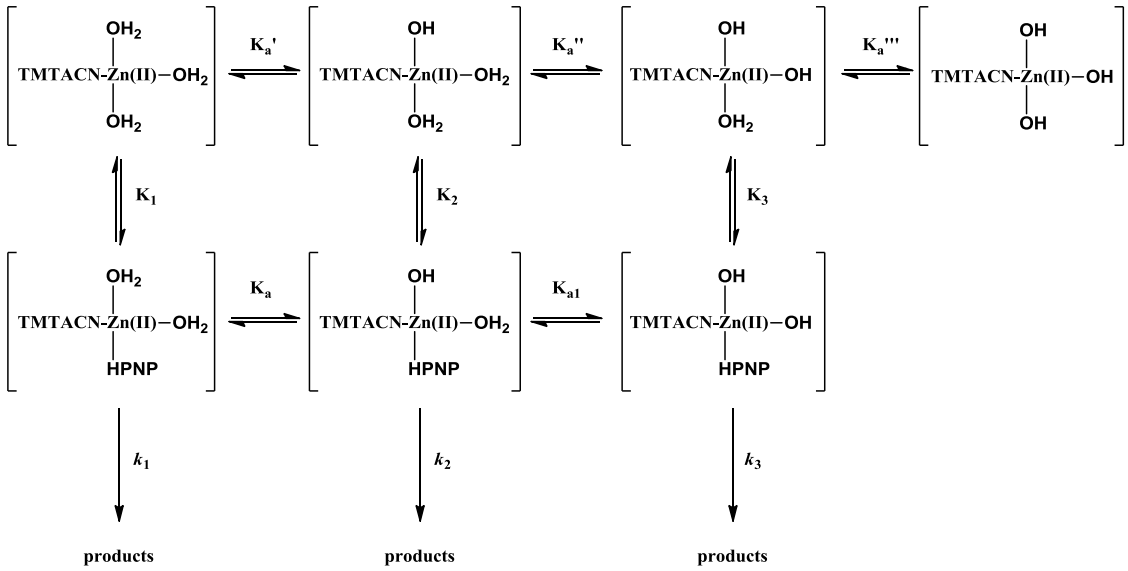

Figure 57. Scheme of the mechanism followed by the complex **2**.

Mass balances

The total amount of TMTACN-Zn(II) in solution is the sum of the 3 different species:

$$[TMTACN \cdot Zn(II)]_{total} = [TMTACN \cdot Zn(II) - (H_2O)_3] + [TMTACN \cdot Zn(II) - (OH)(H_2O)_2] + [TMTACN \cdot Zn(II) - (OH)_2(H_2O)] + [TMTACN \cdot Zn(II) - (OH)_3] \quad (14)$$

This species are related between each other by the equilibrium of deprotonation:

$$K_a^1 = \frac{[TMTACN \cdot Zn(II) - (OH)(H_2O)_2][H^+]}{[TMTACN \cdot Zn(II) - (H_2O)_3]} \quad (15) \qquad K_a^2 = \frac{[TMTACN \cdot Zn(II) - (OH)_2(H_2O)][H^+]}{[TMTACN \cdot Zn(II) - (OH)(H_2O)_2]} \quad (16)$$

$$K_a^3 = \frac{[TMTACN \cdot Zn(II) - (OH)_3][H^+]}{[TMTACN \cdot Zn(II) - (OH)_2(H_2O)]} \quad (17)$$

If we include equations 15 and 16 in the mass balance 14, we obtain the equation 18 which is a relation between the total amount of TMTACN-Zn(II) complex towards the active catalytic species $[TMTACN \cdot Zn(II) - (OH)(H_2O)_2]$:

$$
\begin{aligned}
&[TMTACN \cdot Zn(II)]_{total} \\
&\quad = [TMTACN \cdot Zn(II) - (H_2O)_3] + [TMTACN \cdot Zn(II) - (OH)(H_2O)_2] \\
&\quad + [TMTACN \cdot Zn(II) - (OH)_2(H_2O)] \\
&\quad + \frac{K_a^3}{[H^+]}[TMTACN \cdot Zn(II) - (OH)_2(H_2O)] \\
&\quad = [TMTACN \cdot Zn(II) - (H_2O)_3] + [TMTACN \cdot Zn(II) - (OH)(H_2O)_2] \\
&\quad + \left(1 + \frac{K_a^3}{[H^+]}\right)[TMTACN \cdot Zn(II) - (OH)_2(H_2O)]
\end{aligned}
$$

$$
\begin{aligned}
&[TMTACN \cdot Zn(II)]_{total} \\
&\quad = \frac{[H^+]}{K_a^1}[TMTACN \cdot Zn(II) - (OH)(H_2O)_2] \\
&\quad + [TMTACN \cdot Zn(II) - (OH)(H_2O)_2] \\
&\quad + \left(1 + \frac{K_a^3}{[H^+]}\right)\frac{K_a^2}{[H^+]}[TMTACN \cdot Zn(II) - (OH)(H_2O)_2]
\end{aligned}
$$

$$[TMTACN \cdot Zn(II)]_{total} = \left(\frac{[H^+]}{K_a^1} + 1 + \frac{K_a^2}{[H^+]} + \frac{K_a^2 K_a^3}{[H^+]^2}\right)[TMTACN \cdot Zn(II) - (OH)(H_2O)_2] \quad (18)$$

If we include equations 16 and 17 in the mass balance 14, we obtain the equation 19 which is a relation between the total amount of TMTACN-Zn(II) complex towards the active catalytic species $[TMTACN \cdot Zn(II) - (OH)_2(H_2O)]$:

$$[TMTACN \cdot Zn(II)]_{total}$$
$$= \frac{[H^+]}{K_a^1}[TMTACN \cdot Zn(II) - (OH)(H_2O)_2]$$
$$+ [TMTACN \cdot Zn(II) - (OH)(H_2O)_2]$$
$$+ [TMTACN \cdot Zn(II) - (OH)_2(H_2O)] + [TMTACN \cdot Zn(II) - (OH)_3]$$
$$= \left(\frac{[H^+]}{K_a^1} + 1\right)[TMTACN \cdot Zn(II) - (OH)(H_2O)_2]$$
$$+ [TMTACN \cdot Zn(II) - (OH)_2(H_2O)] + [TMTACN \cdot Zn(II) - (OH)_3]$$

$$[TMTACN \cdot Zn(II)]_{total}$$
$$= \left(\frac{[H^+]}{K_a^1} + 1\right)\frac{[H^+]}{K_a^2}[TMTACN \cdot Zn(II) - (OH)_2(H_2O)]$$
$$+ [TMTACN \cdot Zn(II) - (OH)_2(H_2O)] + \frac{K_a^3}{[H^+]}[TMTACN \cdot Zn(II)$$
$$- (OH)_2(H_2O)]$$

$$[TMTACN \cdot Zn(II)]_{total} = \left(\frac{[H^+]^2}{K_a^1 K_a^2} + \frac{[H^+]}{K_a^2} + 1 + \frac{K_a^3}{[H^+]}\right)[TMTACN \cdot Zn(II) - (OH)_2(H_2O)] \quad (19)$$

The reaction rate observed (k_φ) is measure by the consumption of HPNP with time

$$k_\varphi = \frac{-d[HPNP]}{dt}$$
$$= k_1[TMTACN \cdot Zn(II) - (H_2O)_2(HPNP)] \quad (20)$$
$$+ k_2[TMTACN \cdot Zn(II)$$
$$- (OH)(H_2O)(HPNP)]$$
$$+ k_3[TMTACN \cdot Zn(II) - (OH)_2(HPNP)]$$

Where $k_1 \ll k_2\ and\ k_3$, andthe concentration of catalyst-substrate complexes is related to the concentration of active species $[TMTACN \cdot Zn(II) - (OH)(H_2O)_2]$ and $[TMTACN \cdot Zn(II) - (OH)_2(H_2O)]$ by K_2 and K_3, respectively:

$$k_\varphi = \frac{-d[HPNP]}{dt} = k_2(K_2[TMTACN \cdot Zn(II) - (OH)(H_2O)_2][HPNP]) + k_3(K_3[TMTACN \cdot Zn(II) - (OH)_2(H_2O)][HPNP]) \quad (21)$$

In pseudo-first order conditions,
$[TMTACN \cdot Zn(II) - (OH)(H_2O)_2][HPNP] \approx [TMTACN \cdot Zn(II) - (OH)(H_2O)_2]$ and
$[TMTACN \cdot Zn(II) - (OH)_2(H_2O)][HPNP] \approx [TMTACN \cdot Zn(II) - (OH)_2(H_2O)]$:

$$k_\varphi = k_2'[TMTACN \cdot Zn(II) - (OH)(H_2O)_2] + k_3'[TMTACN \cdot Zn(II) - (OH)_2(H_2O)] \quad (22)$$

Where $k_2'\ and\ k_3'$ includes the complex formation constant $K_2\ and\ K_3$, respectively.

Finally, we substituted equations 18 and 19 in equation 22 and we obtain the relation between the observed reaction rate k_φ towards the concentration of protons (equation 4) which allow us to calculate the first, second and third pKa of the complex TACN-Zn(II) catalyst and also the second order reaction rate between the active species and the substrate, k_2' and k_3'.

$$k_\varphi = k_2' \frac{[TMTACN \cdot Zn(II)]_{total}}{\left(\frac{[H^+]}{K_a^1} + 1 + \frac{K_a^2}{[H^+]} + \frac{K_a^2 K_a^3}{[H^+]^2}\right)} + k_3' \frac{[TMTACN \cdot Zn(II)]_{total}}{\left(\frac{[H^+]^2}{K_a^1 K_a^2} + \frac{[H^+]}{K_a^2} + 1 + \frac{K_a^3}{[H^+]}\right)}$$

$$k_\varphi = \left[\frac{k_2'}{\left(\frac{[H^+]}{K_a'} + 1 + \frac{K_a''}{[H^+]} + \frac{K_a'' K_a'''}{[H^+]^2}\right)} + \frac{k_3'}{\left(\frac{[H^+]^2}{K_a' K_a''} + \frac{[H^+]}{K_a''} + 1 + \frac{K_a'''}{[H^+]}\right)}\right][TMTACN \cdot Zn(II)]_{total} \quad \textbf{(4)}$$

2.3 BNP cleavage by mono-metallic Zn(II) complexes

The cleavage of DNA models like bis *p*-nitrophenyl phosphate (BNP) is more challenging than the cleavage of HPNP, since BNP does not have a hydroxyl group that can act as internal nucleophile. As a consequence, in the cleavage of DNA-like compounds more complex strategies must be developed to achieve effective reactivity. In most cases, this problem has been solved by using metal-ion-coordinated nucleophiles capable to improve the nucleophilic attack at the phosphorus. As mention in the introduction, Chin and others have successfully employed this strategy using Cu(II) complexes of a bis(piridinylmethyl) ligand bearing an alcoholic arm and obtaining 17-fold more reactivity in the cleavage of BNP compared to that of metal-bound hydroxide.[33] However, the inconvenient of this strategy is that in the final product the phosphate remains covalently bound to the ligand's nucleophile and, consequently, the metal complex promoted reaction undergoes no or very slow turnovers (figure 58).

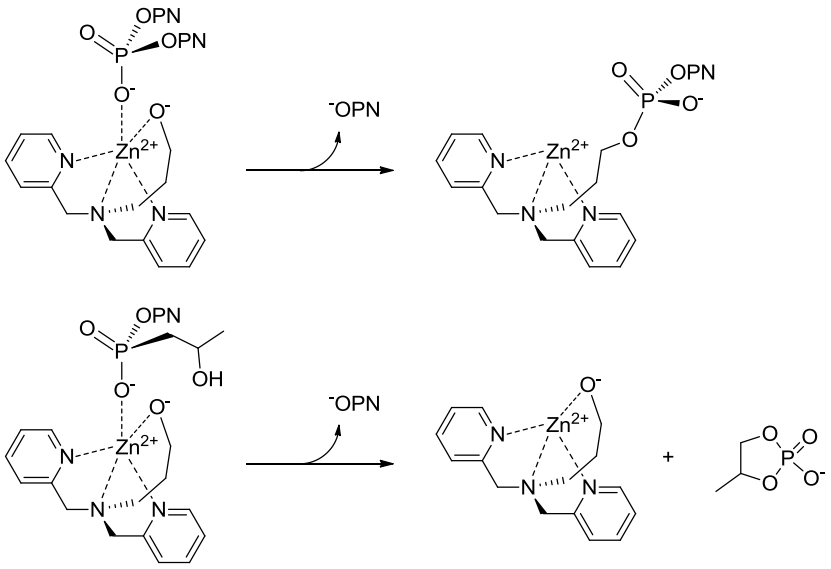

Figure 58. The same catalyst towards the hydrolysis of BNP shows not turn-over, something that does not happen with HPNP.

A substantial improvement of this strategy has been brought about by the use of an aldehyde group in the catalyst instead of an alcoholic group as intracomplex nucleophile. Indeed, the aldehyde is in equilibrium in water with its hydrated germinal diol form. The diol not only is quite an active nucleophile (the second OH group is electrowithdrawing and, consequentely, facilitates the nucleophile deprotonation) but also provides a straightforward way to recycle the phosphorylated inactive nucleophile which decompose when the carbonyl form is restored.

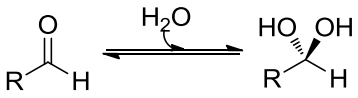

Figure 59. Equilibrium between an aldehyde and a germinal diol.

In this view, we tested the reactivity of a pyridil-based ligand (figure 60), which forms complex **3** with Zn(II) which was provided by the Zonta's group (University of Padova) where it was developed for stereoselective recognition of amino acids[58].

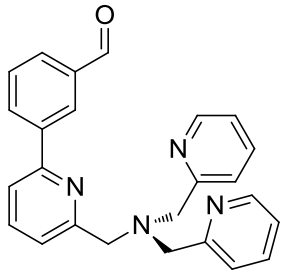

Figure 60. Ligand 3-(6-((bis(pyridine-2-ylmethyl)amino)methyl)pyridin-2-yl)benzaldehyde used to prepared complex **3**.

The aldehyde presented in this ligand is in close proximity to complexed Zn(II) ion but, even in the hydrated form, cannot coordinated to it. Metal coordination of the nucleophile is usually necessary to place the nucleophile in the correct position and in close proximity to the phosphoryl group. However, such a coordination is also expected to decrease the nucleophile activity. We reasoned that the geometry of the complex **3** could have allowed the hydrated form to attack the metal bound phosphate with high reactivity because the

absence of interaction with the metal ion and allowing catalyst turnover thanks to the reversibility of the hydration equilibrium.

The catalytic cycle proposed for complex **3** is reported in figure 61 and starts with the coordination of the BNP, then a molecule of water hydrates the aldehyde group forming the geminal diol. One of the OH group of the diol acts as a nucleophile by attacking the phosphate in BNP which gives the penta-coordinated transition state. Finally, the leaving group $^{-}$ONP is released and the catalyst is regenerated by the formation of the initial aldehyde group.

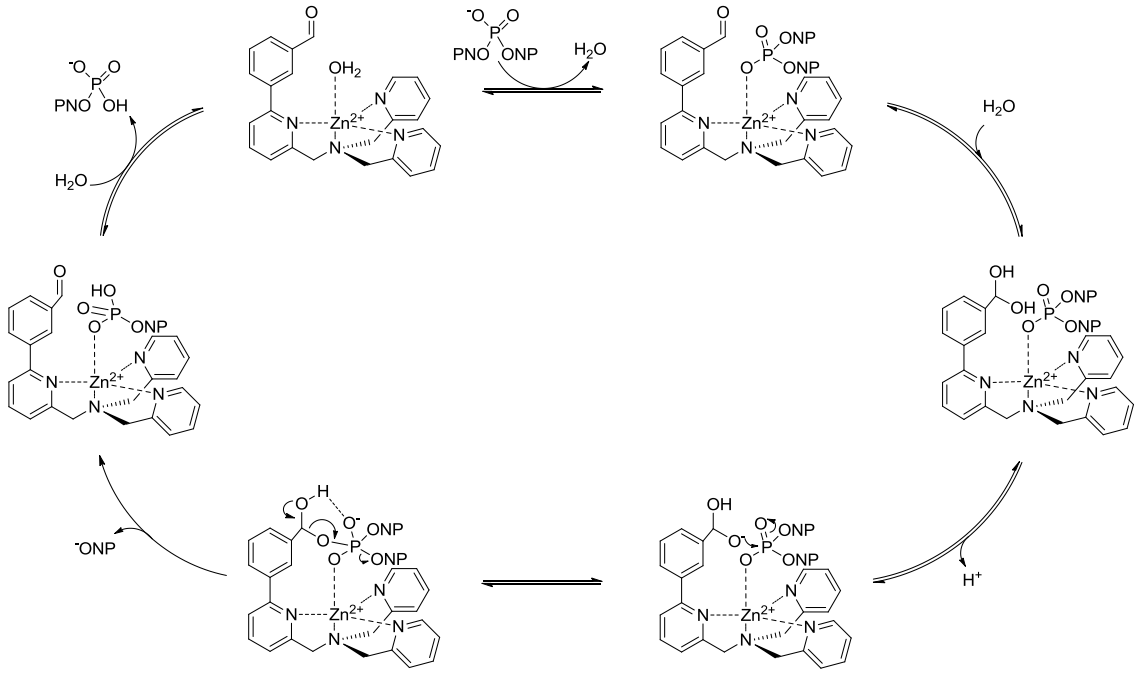

Figure 61. Schema of the catalytic cycle proposed for the complex **3** in the cleavage of BNP.

2.3.1 Kinetics studies and discussion

We studied the hydrolytic cleavage of BNP in aqueous solution promoted by complex **3** by measuring the reaction rate in pseudo-first order conditions where the concentration of **3**-Zn was in a range 0.1 mM – 0.5 mM and that of BNP was 0.02 mM in buffered solutions ([buffer] = 0.05 M). Since the ligand is not soluble in water, stock solutions were prepared in methanol and mixed with an equimolar amount of $Zn(NO_3)_2$. Once formed, the complex **3** becomes soluble in aqueous solution.

However, no acceleration of the rate of BNP cleavage was observed even if the reaction were performed at different pHs and temperatures.

Subsequent experiments performed using HPNP as a substrate were performed with success, obtaining a second order rate constant of 0.002 $M^{-1}s^{-1}$ for the hydrolysis of HPNP with complex **3** at 25 °C and pH 8. This result demonstrates that the metal center is fully accessible to phosphate diesters and the presence of the benzaldehyde moiety does not affect his reactivity.

One possible explanation to this disappointing lack of catalytic activity is the flexibility of the complex **3**. Indeed a better inspection of the possible catalyst structure reveals that the C-C bond between the phenyl containing the aldehyde substituent and the pyridine residue is free to rotate. Particularly when the substrate is bound to the metal ion in the available axial position, the steric hindrance could favor as more stable the conformation where the aldehyde group is far away from the Zn(II). In this situation, the catalyst will be inactive, since no nucleophile is available to attack the phosphoryl group.

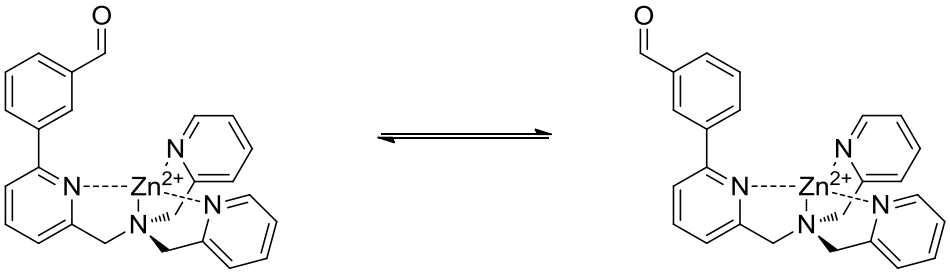

Figure 62. Conformation equilibrium of complex **3**.

Chapter 3

EFFICIENT PHOSPHODIESTER CLEAVING NANOZYMES

3.1 Overview

The use of gold nanoparticles as scaffolds to self-organized molecules on their surface has attracted a lot of attention in the last decades. In particular, our attention has been focused to create phosphodiester cleaving gold-nanoparticles (nanozymes) due to the spontaneous formation of bimetallic catalytic sites on the nanoparticle surface.

The nanozymes reported here are able to hydrolyze a RNA model substrate, the 2'-hydroxy-*p*-nitrophenyl phosphate (HPNP) with an efficiency never reported before thanks to a modification of the structure of the nanoparticle-coating molecules.

This structure modification produces a polarity decrease of the reaction site environment and, as a consequence, a higher stabilization of the transition state that accelerates the hydrolysis of the phosphate derivative.

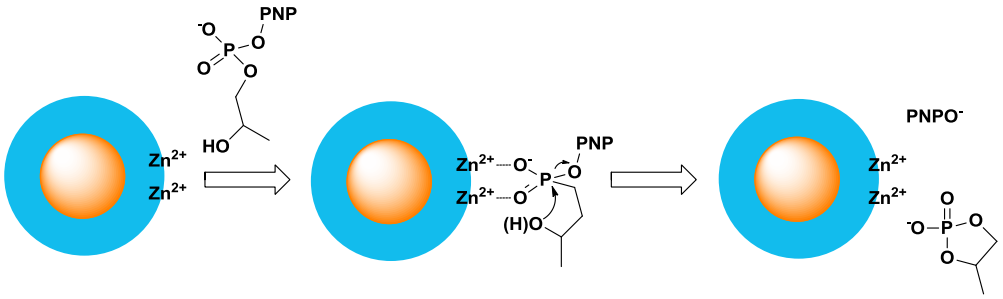

Figure 63. Mechanism of HPNP cleavage by nanozymes

3.2 Modification of the structure of the nanoparticle-coating molecules

The modular structure of the molecules that form the nanoparticle coating allows their easy modification and, hence, tuning the properties of the nanoparticles.

As discussed earlier, the hydrolytic (or solvotic) cleavage of phosphate diesters promoted by metal ions is by far more efficient when the reaction occurs in low polarity solvents, with respect to water, as methanol or ethanol. The microenvironment provided by the nanoparticle protecting monolayer offers the possibility to create low polarity reaction sites even in water. Indeed, Prins and coworkers[59], demonstrated that the reaction occurs on the interface between the nanoparticle surface and the bulk aqueous solution, consequently, one may speculate that the proper modification of the coating molecules can shift the reaction site deeper in the monolayer, producing and environment polarity decrease and, hence, an increase of the hydrolytic efficiency of the nanozymes.

Thiol **1** (Figure 64), bearing the 1,4,7-triazacyclononane metal chelating moiety, was previously used to prepare nanoparticles for the cleavage of HPNP in the presence of Zn(II). This molecule has a modular structure divided in three parts: i) the first module is composed by a derivative of thioctanoic acid, it ensures the functional group necessary for nanoparticle grafting and contributes to monolayer stability thanks to interchain dispersion interaction; ii) the second module is a 1,4-butandiamine spacer that connects the first module with the third one; iii) the third part is a 1,4,7-triazacyclononane derivative that provides the thiol with metal chelating and catalytic ability. We reasoned that the modification of this thiol by insertion of different spacers as second module, namely two long alkyl chains (thiol **2** and **4**) or an oligoethylene glycol (thiol **3**), could allow us the tunning of the monolayer properties and, in particular, the realization of more hydrophobic or hydrophilic reaction sites.

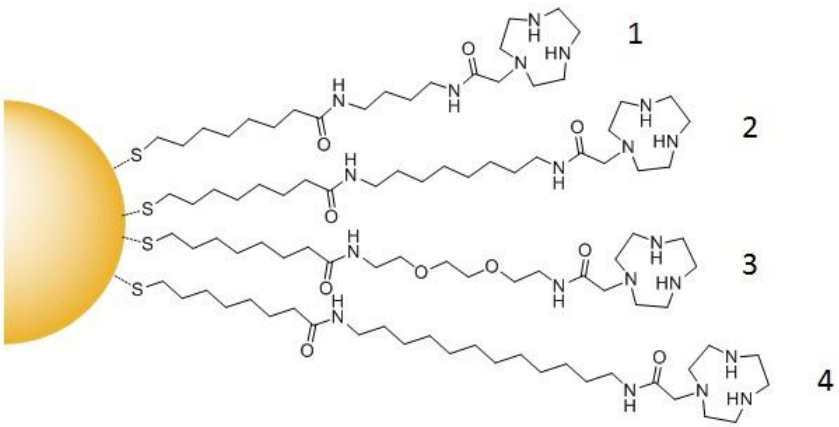

Figure 64. Metal chelating thiols used, represented in their nanoparticle-bound form.

3.3 Gold nanoparticles synthesis and characterization

3.3.1 Synthesis and characterization of MPGN

We used the thiols **1-4** to prepare monolayer protected gold nanoparticles (MPGN) according to a previously reported two-step procedure[48]. The nanozyme samples were:

- $MPGN_1$: AuNPs 100% TACN-C4
- $MPGN_2$: AuNPs 100% TACN-C8
- $MPGN_3$: AuNPs 100% TACN-TEG
- $MPGN_4$: AuNPs 100% TACN-C12

The best technique to measure the size of nanoparticles with a diameter smaller than 5 nm, as it is in our case, is Transmission Electron Microscopy (TEM). This microscopy uses a beam of electrons that is transmitted through the sample deposited on a ultra-thin copper grid and kept in ultra-high vacuum. Electrons interacting with the nanoparticles as the beam passes through are absorbed or scattered. The imagine, hence, is formed by collecting the electrons transmitted through the sample.

TEM imagines obtained with a 120 kV instrument where analyzed with Image-J software to measure the diameters distribution and average value. Analysis of different samples of small nanoparticles (Figures 65, 69, 73 and 77) yields an average diameter for the MPGN of 1.6±0.4 nm (with the exception of $MPGN_{\mathbf{1}}$ which are slightly smaller).

The thermogravimetric analysis (TGA) is a thermal analysis method in which changes in weight of selected materials are measured as a function of increasing temperature. In our case, this technique is useful to determine the amount of organic material (monolayer) in a sample of nanoparticles. In fact, the molecules forming the monolayer are completely pyrolized or oxidized and only the metal core remains unaltered at high temperature. The average formula for $MPGN_{\mathbf{2\text{-}4}}$ is $Au_{140}RS_{50}$, as calculated on the basis of TGA analysis (Figures 70, 74 and 78) using the spherical approximation, where RS indicate the thiol molecules forming the protecting monolayer. This value well compares with that of $Au_{140}RS_{53}$ calculated by Murray and co-workers for nanoparticles with a diameter of 1,62 nm using a truncoctahedron shape[*] and with the $Au_{144}RS_{60}$ nanoparticle characterized by mass spectroscopy. Formula for $MPGN_{\mathbf{1}}$ (Figure 66) is $Au_{54}RS_{41}$, in agreement with the $Au_{80}RS_{38}$ calculated by Murray and coworkers[60] for nanoparticles with a diameter of 1,30 nm using a truncoctahedron shape and with the AuRS characterized by mass spectroscopy by Dass and coworkers[61].

NMR analysis (Figures 67, 71, 75 and 79) indicates monolayer formation (broadening of all signals), as confirmed by diffusion-filtered experiments (Figures 68, 72 and 76). The characteristic broad signals observed in the spectrum of a nanoparticle arise from several copies of the same organic molecules grafted to a slow-tumbling object. When a molecule is bound to supramolecular systems, as nanoparticles, the relaxation time increased which caused the broadening of its NMR signals since there is not enough time to the molecule to relax its spins before the new frequency pulse.

Moreover, NMR analysis is useful to quantify the purity of the sample, since the absence of sharp peaks (apart from solvents) confirms the non-presence of organic molecules not attached to the gold surface.

$MPGN_1$ (thiol 1, TACN-C4)

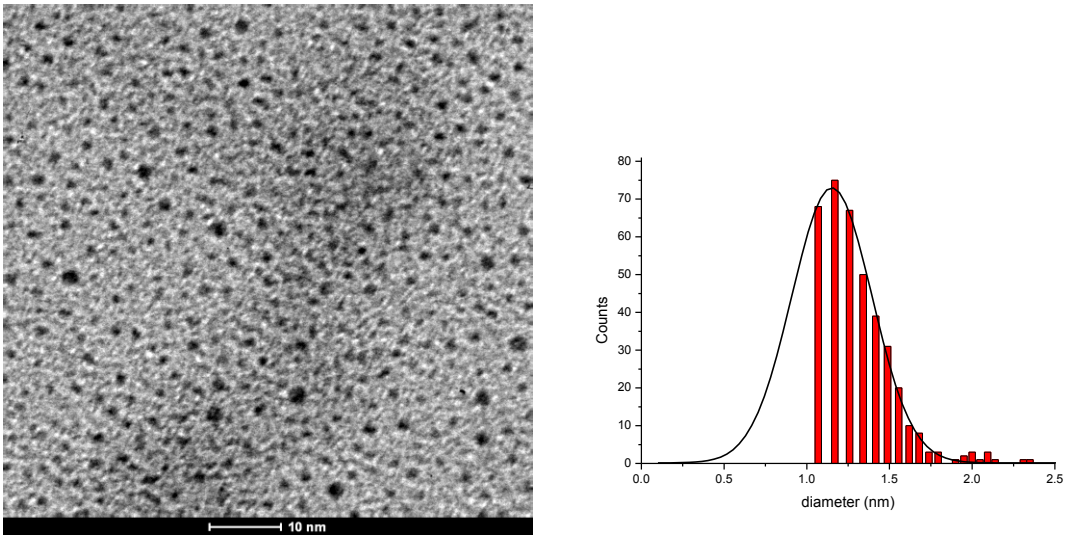

Figure 65. Sample TEM image of $MPGN_1$ and size distribution: average diameter = 1.2 nm (σ= 0.3 nm).

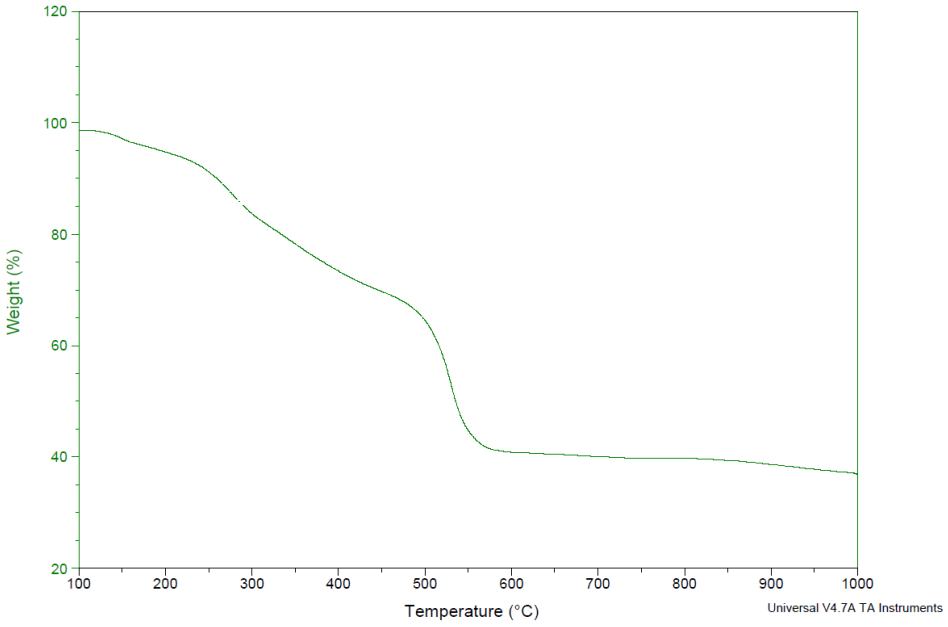

Figure 66. TGA analysis of a sample of $MPGN_1$ under air atmosphere.

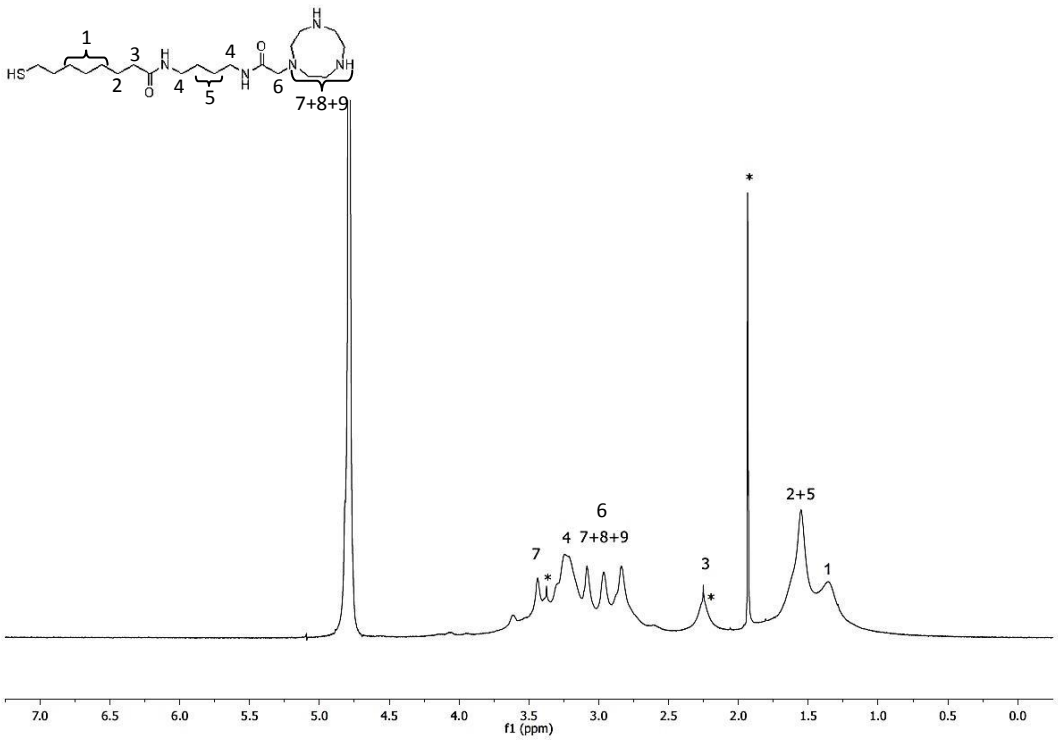

Figure 67. 1H-NMR (300 MHz) spectrum of the $MPGN_1$ in D_2O (* unknown impurities).

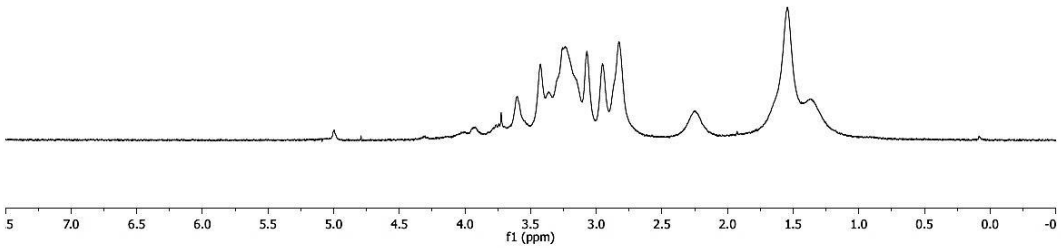

Figure 68. Diffussion-filtered 1H-NMR (300 MHz) spectrum of the $MPGN_1$ in D_2O.

$MPGN_2$ (thiol 2, TACN-C8)

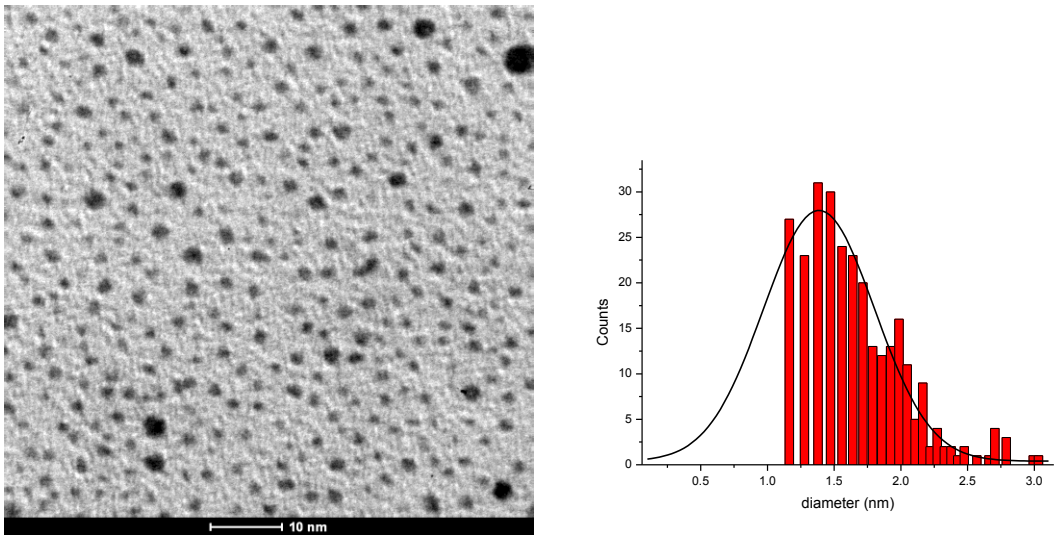

Figure 69. Sample TEM image of $MPGN_2$ and size distribution: average diameter = 1.4 nm (σ= 0.4 nm).

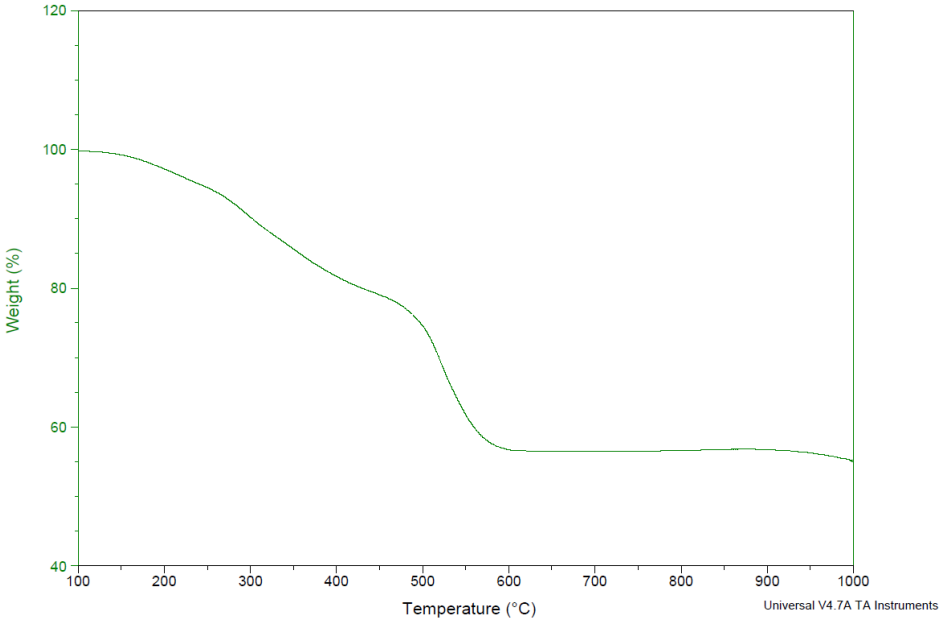

Figure 70. TGA analysis of a sample of $MPGN_2$ under air atmosphere.

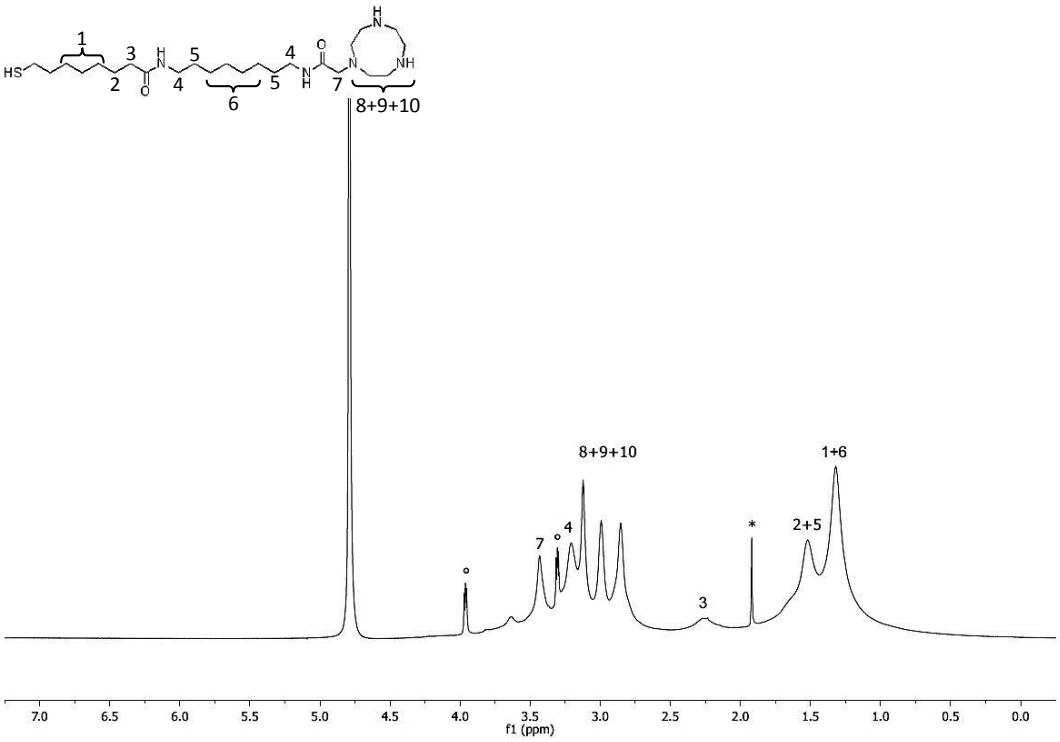

Figure 71. 1H-NMR (300 MHz) spectrum of the $MPGN_2$ in D_2O (* unknown impurities).

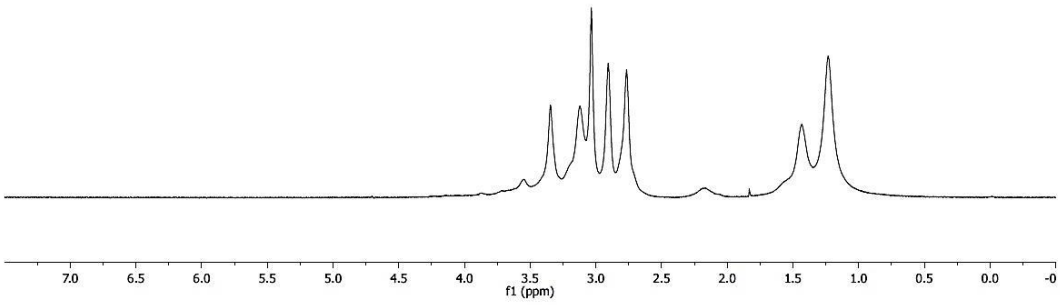

Figure 72. Diffussion-filtered 1H-NMR (300 MHz) spectrum of the $MPGN_2$ in D_2O.

$MPGN_3$ (thiol 3, TACN-TEG)

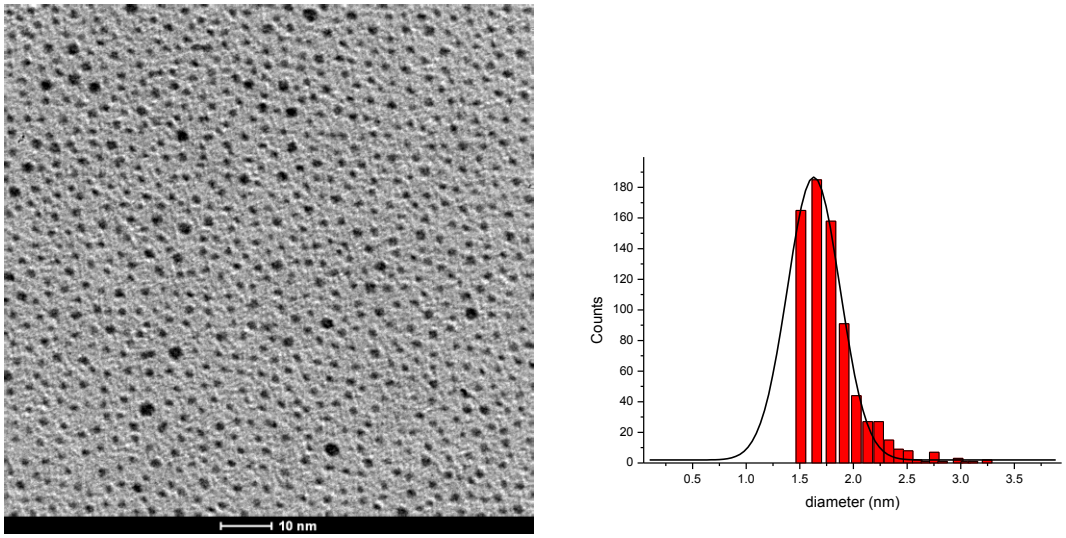

Figure 73. Sample TEM image of $MPGN_3$ and size distribution: average diameter = 1.6 nm (σ= 0.3 nm).

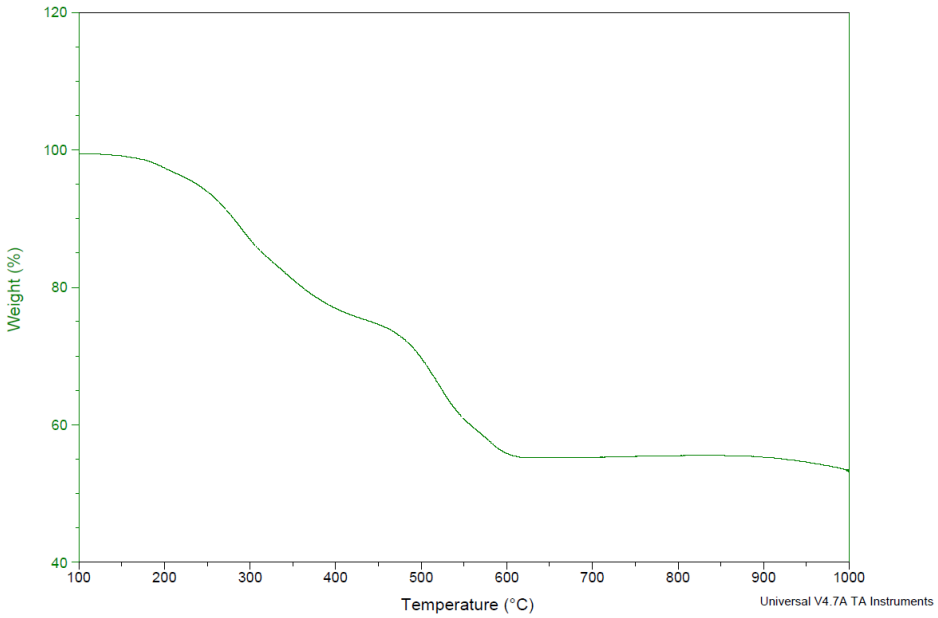

Figure 74. TGA analysis of a sample of $MPGN_3$ under air atmosphere.

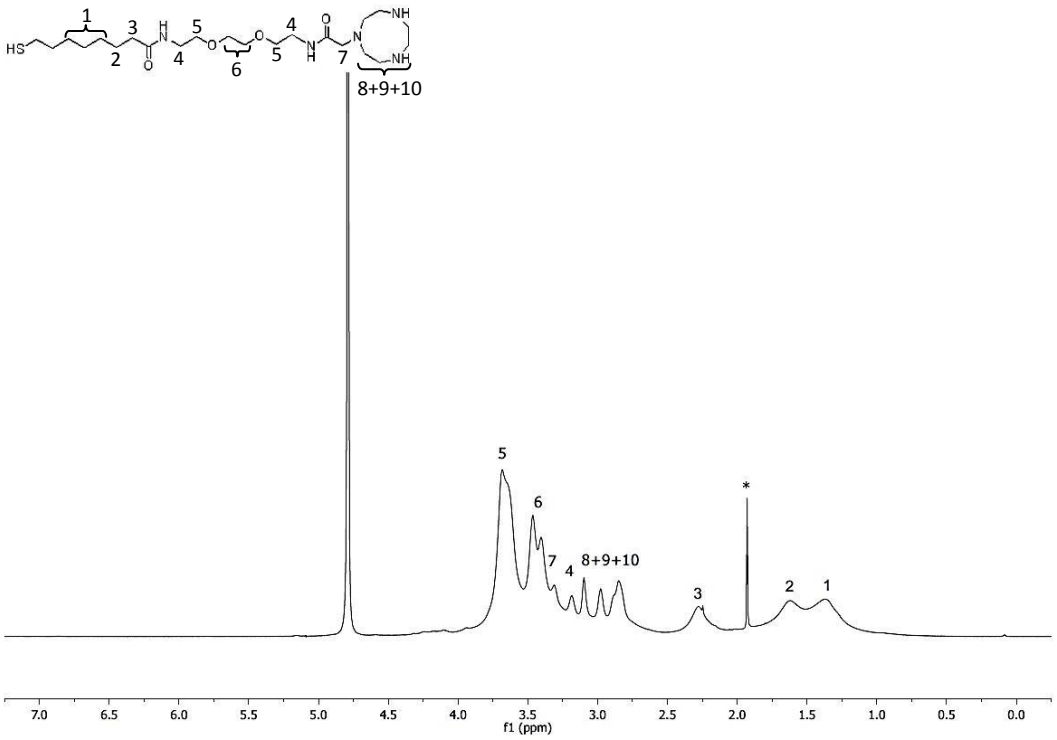

Figure 75. 1H-NMR (300 MHz) spectrum of the $MPGN_3$ in D_2O.

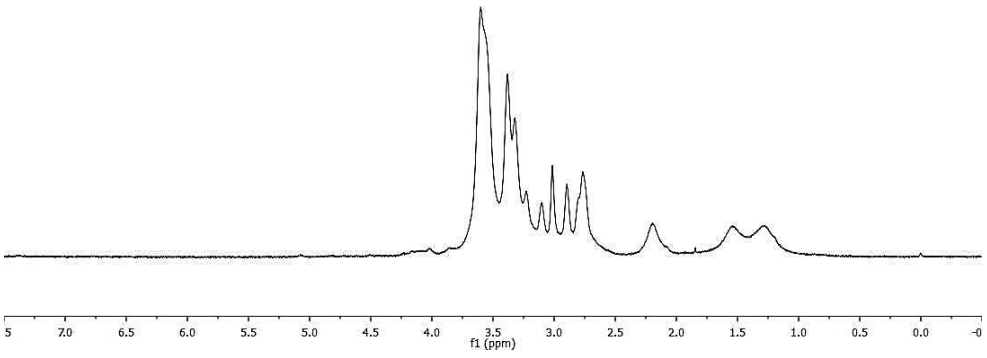

Figure 76. Diffussion-filtered 1H-NMR (300 MHz) spectrum $MPGN_3$ in D_2O.

$MPGN_4$ (thiol 4, TACN-C12)

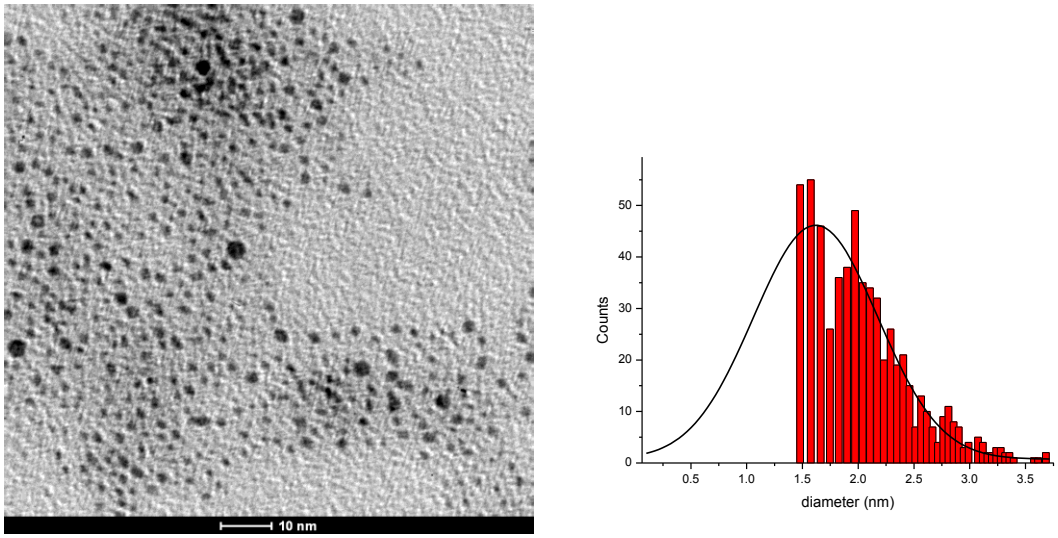

Figure 77. Sample TEM image of $MPGN_4$ and size distribution: average diameter = 1.6 nm (σ= 0.6 nm).

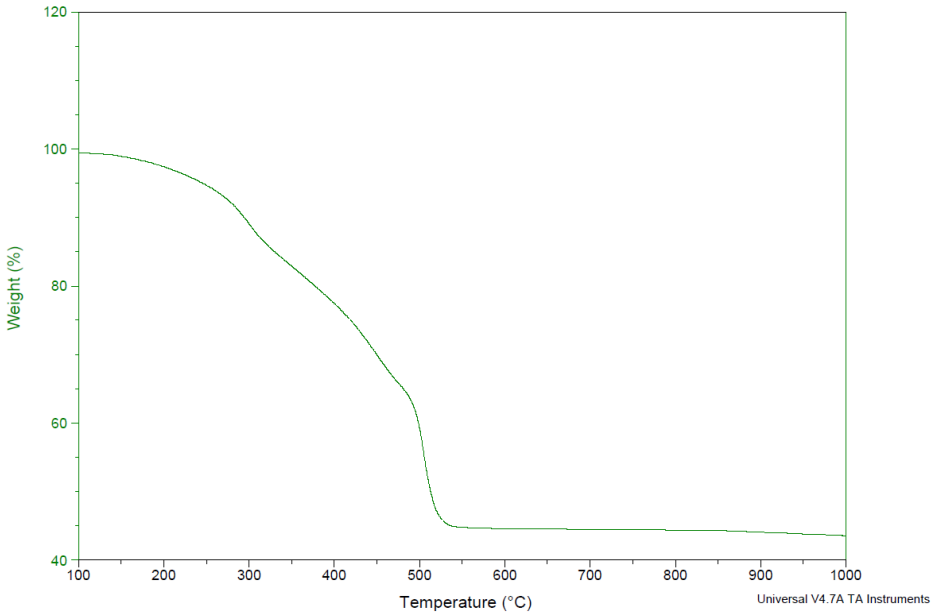

Figure 78. TGA analysis of a sample of $MPGN_4$ under air atmosphere.

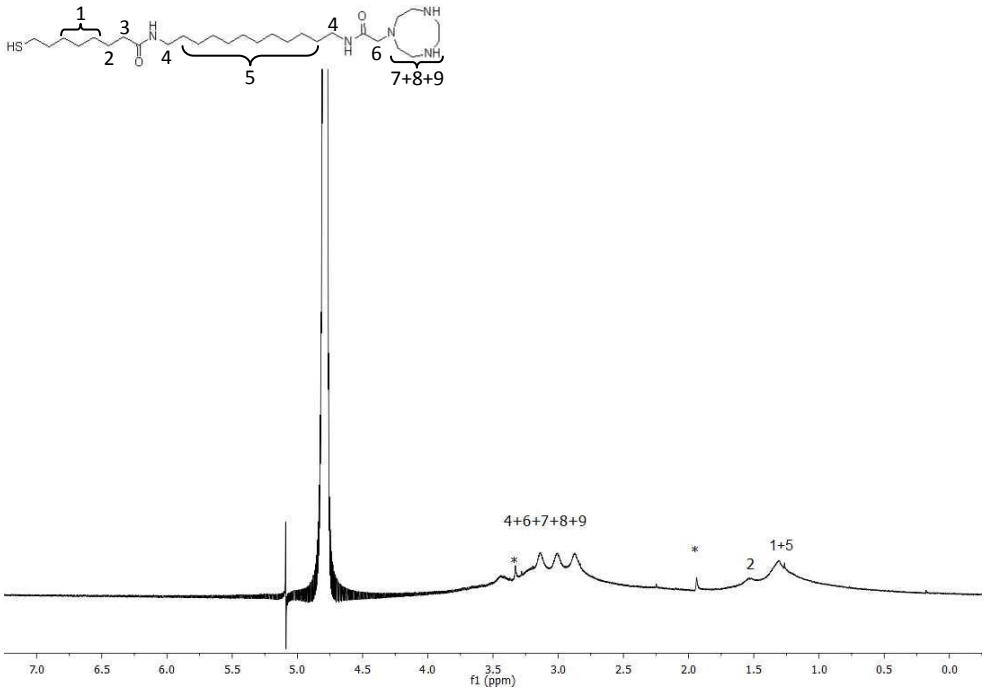

Figure 79.1H-NMR (300 MHz) spectrum of the $MPGN_4$ in D_2O.

3.4 Kinetics studies

3.4.1 Cooperativity

The reactivity of the systems $MPGN_{1-4}$ was tested towards the cleavage reaction of the RNA model 2'-hydroxy-*p*-nitrophenyl phosphate (HPNP). The first experiments were devoted to confirm the TACN units concentration in $MPGN_{\mathbf{1-4}}$ stock solutions. For this reason, Zn(II) dependent kinetic experiments (Figure 80) were performed at constant HPNP and nanoparticles concentration. Zn(II) concentrations values at which nanoparticles reactivity leveled off were considered the saturation concentrations of all the TACN units present in the nanoparticles. In all the cases, TACN concentration determined in this way were within 20% from what expected on the basis of the nanoparticles weight concentrations.

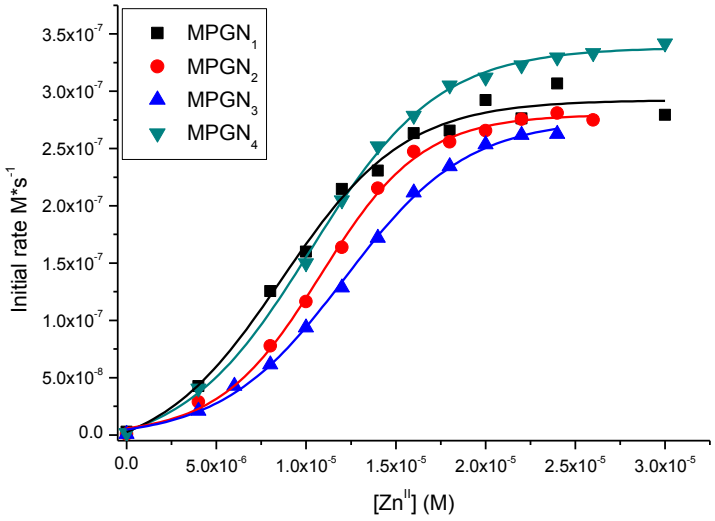

Figure 80. Zn^{II} dependence of the kinetics experiments for the reaction between HPNP and Zn(II) complexes of $MPGN_{\mathbf{1-4}}$. Conditions: [TACN] = 2.0×10^{-5} M, [HPNP] = 2.0×10^{-3} M, [buffer] = 1.0×10^{-2} M, pH = 7.5, T = 25 °C (for $MPGN_{\mathbf{2}}$ and $MPGN_{\mathbf{4}}$) and 40°C (for $MPGN_{\mathbf{1}}$ and $MPGN_{\mathbf{3}}$).

In addition, it must be noted that reactivity profiles in Figure 80 show a sigmoidal profile which can be considered as diagnostic of a cooperative system. Accordingly to the most commonly accepted reaction mechanism and in particular with the recent studies by Prins and coworkers[62] at least two TACN-Zn(II) units cooperate to accelerate the cleavage of

phosphate derivatives. Consequently, as soon as two neighbouring TACN units are populated by metal ions, the reactivity undergoes substantial, and more than additive, increase.

3.4.2. Enzyme-like behaviour

One of the most interesting characteristic of the nanozymes is their catalytic behaviour similar to enzymes which means that the eraction is preceded by the interaction of the substrate (S) with the nanozyme (N) forming the complex substrate-nanozyme (SN). The complex formation is then followed by the conversion of the substrate (S) into a product (P) and its release in the reaction medium to restore the nanozyme. This is confirmed by the observation that all MPGN$_{\mathbf{1\text{-}4}}$ follow saturation profiles when the HPNP concentration is increased (Figure 81).

These enzyme-like behaviour allows us to fit the reactivity profiles with Michaelis-Menten equation (23):

$$v = \frac{k_{max}[HPNP]}{\frac{1}{K_{HPNP}} + [HPNP]} \qquad (23)$$

where v is the reaction initial rate, k_{max} is the limiting reaction rate in the experimental conditions and and K_{HPNP} is the apparent binding constant of the substrate to the catalyst. k_{cat} values were obtained by dividing k_{max} by $[Zn^{II}]/2$ (half to the total Zn(II) concentration is used to account by the fact the reaction occurs in bimetallic sites).

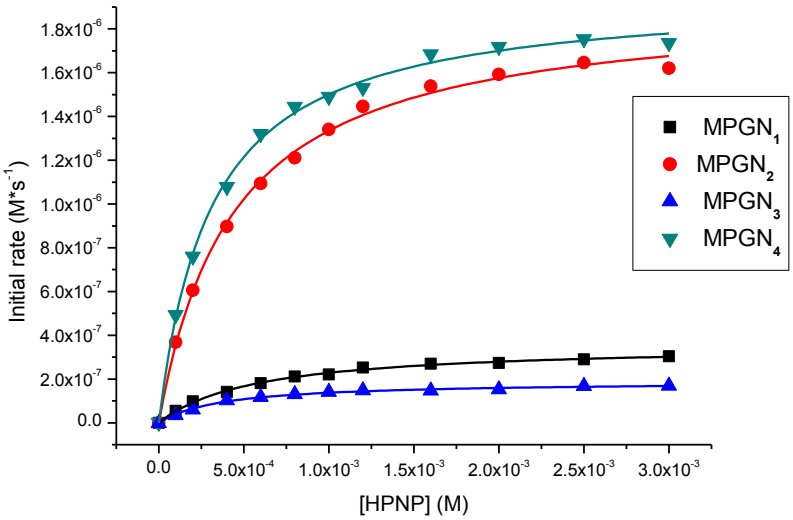

Figure 81. Rate of HPNP cleavage promoted by $MPGN_{1\text{-}4}$ and Zn(II) as a function of the concentration of HPNP. Conditions: [NP, in thiol units] = 2.0×10^{-5} M, [Zn(II)] = 2.0×10^{-5} M, [buffer] = 1.0×10^{-2} M, pH = 7.5, 40 °C.

Figure 81 displays the dependence of the HPNP cleavage rate as a function of substrate concentration. It is fascinating to see how small modifications in the spacer unit in thiols **1-4** produce remarkable effects on the nanozymes reactivity. A carefully examination of the plots shows that the reactivity of the nanoparticles coated with the longer alkyl-spaced, thiols **2** and **4**, is substantially higher than that of **1**-coated nanoparticles. By contrary, nanoparticles coated with thiols containing the oligoethylene glycol spacer (thiol **3**) are less reactive than those coated with thiol **1**. Fitting of the reactivity profiles reported in figure 81 with the Michaelis-Menten equation provides the kinetic parameters reported in Table 3.

Table 3. Michaelis-Menten parameters for HPNP cleavage in the presence of MPGN1-4 and Zn(II) in water at pH 7.5 and 40 °C. Errors are within ±5%

MPGN	k_{cat} [a] (s^{-1})	K_M [a] (mM)	k_2 [b] (M^{-1} s^{-1})	k_{rel} [c]
1	0.036	0.58	62	1.8×10^5
2	0.192	0.44	437	9.6×10^5
3	0.019	0.38	50	9.5×10^4
4	0.196	0.31	638	9.8×10^5

a) Normalized for the theoretical concentration of bimetallic sites, i.e. [Zn(II)/2]. b) $k_2 = k_{cat}/K_M$. c) $k_{rel} = k_{cat}/k_{uncat}$, $k_{uncat} = 2 \times 10\ s^{-1}$, ref [62]. (Conditions: [NP, in thiol units] = 2.0×10^{-5} M, [Zn(II)] = 2.0×10^{-5} M, [buffer] = 1.0×10^{-2} M).

Note that the affinity of the $MPGN_{1\text{-}4}$ for the substrate is similar in all cases, being the apparent dissociation constant K_M of the same order of magnitude, which means that the difference in reactivity between the systems is not due to a higher affinity of the nanoparticles for the substrate. Indeed, it is due to an increase in the intrinsic activity of the MPGN coated with thiols **2** and **4**, as highlighted by the values of k_{cat}.

3.4.3. pH dependence kinetic experiments

The study of the phosphate hydrolysis at difference pHs give us a bell profile (figure 82). The increase of the pH up to 8.5 accelerates the cleavage reaction but, once reached this maximum, the values of initial rate decrease with further pH increments.

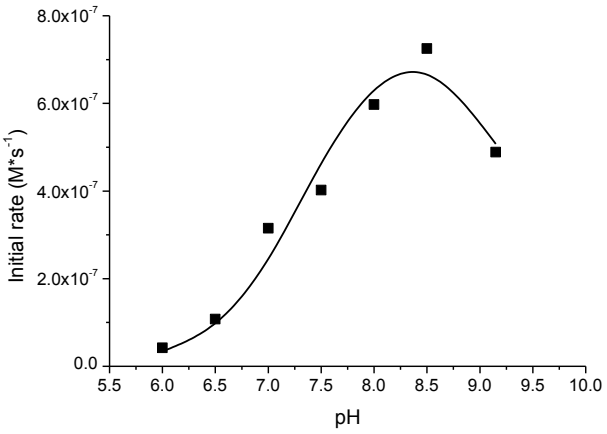

Figure 82. pH dependence of the maximum rate values from the Michaelis-Menten kinetics experimentes for the reaction between HPNP and Zn(II) complexes of **$MPGN_2$ (TACN-C8alkyl).**Conditions: [TACN-Zn^{II}] = 2.0×10^{-5} M, [HPNP]= 2.0×10^{-3} M, [buffer] = 1.0×10^{-2} M, T= 25°C.

This behaviour is quite common to others metal-based catalysts for phosphate cleavage and indicates that at least two acid species participate to the reaction. Indeed, to complete the coordination sphere of the Zn(II) ion once bound to TACN, at least two water molecules are needed. However, deprotonation of the first one generates a hydroxyl group bound to the metal ion, which can act as base and promote the deprotonation of the 2'-hydroxyl group of the substrate HPNP speeding up the system reactivity. On the other hand, the deprotonation of the second water molecule works against the formation of the complex substrate-nanozyme, since the two hydroxyl groups saturate the coordination sphere of the metal ion and there is not water molecule to be replace by the phosphate. Opposite influence of the two deprotonation events justifies the bell-shape of the pH-reactivity profiles.

There is a second kinetically equivalent mechanistic hypothesis to explain the pH dependence behaviour of these systems (figure 82). This hypothesis postulates the

deprotonation of the substrate HPNP before binding the catalyst, so the catalyst will work only as a Lewis acid. In this hypothesis, the active species is the di-acquo complex, which as the highest Lewis acidity (more positive) and can easily accommodate the substrate, and the following deprotonations have a negative effect on the complex ability to promote the reaction because they decrease the metal Lewis acidity and inhibit the formation of the substrate-nanozyme complex.

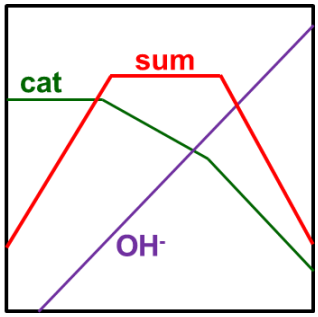

Figure 83. Schematic diagram of the second mechanistic hypothesis.

At pH 8.5, where the maximum of activity is reached for $MPGN_2$ catalyst, the Michaelis Menten kinetics experiment reveals that the binding affinity (K_M) is decreased by a factor of two while the activity of the system (k_{cat}) is doubled for an increase of one unit in pH (Table 4) at the same temperature. This behaviour process no changes in the overall reactivity of the system, since the higher activity is compensated with the lower affinity. This lower affinity can be understood if we consider that the formation of the active species of the catalyst is formed when a hydroxide molecule is bound to the metal ion, reducing the positive charged on the Zn(II) which will have less affinity for the negatively charged substrate. This behaviour is consistent with both proposed mechanism.

Table 4. Michaelis-Menten parameters for HPNP cleavage in the presence of **2**-coated AuNp and Zn(II) in water at 25 °C. Errors are within ±5%.

pH	k_{cat} [a] (s^{-1})	K_M [a] (mM)	k_2 [b] ($M^{-1}\ s^{-1}$)	k_{rel} [c]
7.5	0.043	0.30	144	2.2×10^5
8.5	0.076	0.54	143	3.8×10^5

a) Normalized for the theoretical concentration of bimetallic sites, i.e. [Zn(II)/2]. b) $k_2 = k_{cat}/K_M$. c) $k_{rel} = k_{cat}/k_{uncat}$, $k_{uncat} = 2 \times 10\ s^{-1}$, ref [62]. (Conditions: [NP, in thiol units] = 2.0×10^{-5} M, [Zn(II)] = 2.0×10^{-5} M, [buffer] = 1.0×10^{-2} M).

3.4.4. Temperature dependant kinetic experiments

For a further understanding of the systems, we have performed the Michaelis-Menten kinetics experiments with the $MPGN_{1-4}$ at different temperatures from 25 to 52 °C. Figure 84 is an illustration of the temperature dependence kinetics experiments of $MPGN_2$ with a 5°C interval and clearly shows that temperature has a strong influence in k_{cat}.

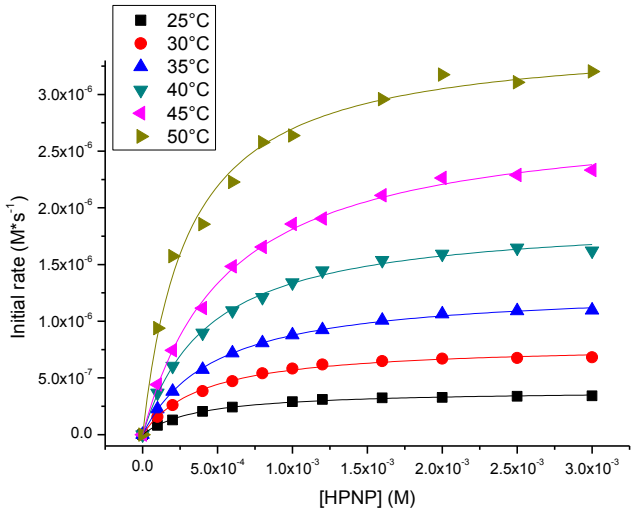

Figure 84. Temperature dependence of the Michaelis-Menten kinetics experiments for the reaction between HPNP and Zn(II) complexes of $MPGN_2$ (**TACN-C8alkyl**). Conditions: [TACN-Zn^{II}] = 2.0×10^{-5} M, [buffer] = 1.0×10^{-2} M, pH= 7.5, T = 25 - 50 °C.

A careful examination of the Michaelis-Menten parameters for the $MPGN_{1-4}$ at the different temperatures (tables 5, 6, 7 and 8) reveals the same behaviour for all the systems, a strong influence of the temperature in k_{cat} but less significant in K_M. Moreover, the second order rate constant increases up to 10-fold when temperature increase from 25 to 52°C.

Table 5. Temperature dependence of the Michaelis-Menten kinetics constants for the reaction between HPNP and Zn(II) complexes of **$MPGN_1$.**

T (°C)	k_{cat} [a] ($\times 10^{-2}$ s^{-1})	K_M [a] (mM)	k_2 [b] (M^{-1} s^{-1})
25	0.60 ± 0.01	0.45 ± 0.03	14±1
30	1.35 ± 0.03	0.50 ± 0.03	27 ± 2
32	1.36 ± 0.02	0.57 ± 0.04	24 ± 2
35	2.31 ± 0.05	0.54 ± 0.04	43 ± 3
37	2.51 ± 0.03	0.54 ± 0.02	46 ± 2
40	3.60 ± 0.07	0.58 ± 0.03	62 ± 4
42	4.32 ± 0.04	0.62 ± 0.03	70 ± 4
45	5.12 ± 0.11	0.74 ±0.04	69 ± 4
47	6.69 ± 0.06	0.64 ± 0.03	105 ± 5
50	7.36 ± 0.17	0.66 ± 0.04	112 ± 8
52	8.60 ± 0.13	0.62 ± 0.04	139 ± 9

a) Normalized for the theoretical concentration of bimetallic sites, i.e. [Zn(II)/2]. b) $k_2 = k_{cat}/K_M$. (Conditions: [NP, in thiol units] = 2.0×10^{-5} M, [Zn(II)] = 2.0×10^{-5} M, [buffer] = 1.0×10^{-2} M).

Table 6. Temperature dependence of the Michaelis-Menten kinetics constants for the reaction between HPNP and Zn(II) complexes of **$MPGN_2$.**

T (°C)	k_{cat} [a] **($\times 10^{-2}$ s^{-1})**	K_M [a] (mM)	k_2 [b] (M^{-1} s^{-1})
25	4.30 ± 0.09	0.30 ± 0.02	144 ± 12
30	8.85 ± 0.14	0.39 ± 0.02	230 ± 14
32	10.6 ± 0.2	0.38 ± 0.03	279 ± 23
35	13.4 ± 0.2	0.39 ± 0.02	347 ± 24
37	17.1 ± 0.3	0.45 ± 0.03	380 ± 26
40	21.2 ± 0.2	0.40 ± 0.02	525 ± 22
42	23.2 ± 0.4	0.48 ± 0.04	483 ± 41
45	30.8 ± 0.7	0.49 ± 0.04	627 ± 48
47	35.5 ± 0.7	0.44 ± 0.04	807 ± 75
50	44.9 ± 0.6	0.51 ± 0.02	876 ± 43
52	53.4 ± 1.4	0.48 ± 0.05	1113 ± 120

a) Normalized for the theoretical concentration of bimetallic sites, i.e. [Zn(II)/2]. b) $k_2 = k_{cat}/K_M$. (Conditions: [NP, in thiol units] = 2.0×10^{-5} M, [Zn(II)] = 2.0×10^{-5} M, [buffer] = 1.0×10^{-2} M).

Table 7. Temperature dependence of the Michaelis-Menten kinetics constants for the reaction between HPNP and Zn(II) complexes of **MPGN$_3$**.

T (°C)	k_{cat} [a] (×10^{-2} s^{-1})	K_M [a] (mM)	k_2 [b] (M^{-1} s^{-1})
25	0.36 ± 0.01	0.36 ± 0.02	10 ± 1
30	0.78 ± 0.01	0.37 ± 0.02	21 ± 2
32	1.01 ± 0.02	0.36 ± 0.03	28 ± 3
35	1.26 ± 0.02	0.37 ± 0.02	34 ± 2
37	1.49 ± 0.03	0.37 ± 0.03	40 ± 3
40	1.90 ± 0.04	0.38 ± 0.03	50 ± 4
42	2.25 ± 0.04	0.39 ± 0.03	58 ± 5
45	3.03 ± 0.03	0.45 ± 0.01	67 ± 2
47	3.39 ± 0.07	0.44 ± 0.04	77 ± 7
50	4.63 ± 0.05	0.74 ± 0.02	62 ± 2
52	5.32 ± 0.07	0.47 ± 0.03	113 ± 8

a) Normalized for the theoretical concentration of bimetallic sites, i.e. [Zn(II)/2]. b) $k_2 = k_{cat}/K_M$. (Conditions: [NP, in thiol units] = 2.0 × 10^{-5} M, [Zn(II)] = 2.0 × 10^{-5} M, [buffer] = 1.0 × 10^{-2} M).

Table 8. Temperature dependence of the Michaelis-Menten kinetics constants for the reaction between HPNP and Zn(II) complexes of MPGN$_4$.

T (°C)	k_{cat} [a] (×10^{-2} s^{-1})	K_M [a] (mM)	k_2 [b] (M^{-1} s^{-1})
25	3.73 ± 0.08	0.15 ± 0.02	255 ± 32
30	8.13 ± 0.15	0.23 ± 0.02	349 ± 31
32	9.96 ± 0.17	0.24 ± 0.02	415 ± 36
35	12.6 ± 0.3	0.23 ± 0.02	553 ± 53
37	13.8 ± 0.3	0.24 ± 0.02	575 ± 50
40	19.6 ± 0.2	0.30 ± 0.01	638 ± 30
42	21.8 ± 0.4	0.29 ± 0.02	752 ± 54
45	28.0 ± 0.7	0.29 ± 0.03	964 ± 98
47	33.8 ± 1.0	0.36 ± 0.04	939 ± 108
50	42.8 ± 0.7	0.36 ± 0.02	1204 ± 73
52	49.0 ± 1.1	0.39 ± 0.03	1256 ± 101

a) Normalized for the theoretical concentration of bimetallic sites, i.e. [Zn(II)/2]. b) $k_2 = k_{cat}/K_M$. (Conditions: [NP, in thiol units] = 2.0 × 10^{-5} M, [Zn(II)] = 2.0 × 10^{-5} M, [buffer] = 1.0 × 10^{-2} M).

3.5 Transition state studies

The explanation for the different reactivity of system as similar as $MPGN_{1-4}$ resides in the formation of more stable transition state complexes between the catalyst and the substrate in the most reactive nanozymes ($MPGN_2$ and $MPGN_4$). This is confirmed by the values of the thermodynamic parameters obtained by the fitting of the kinetic constant k_{cat} versus the temperature data to equation 25 (fittings shown in the appendix), a linearization of the Eyring-Polanyi equation (24):

$$k = \frac{k_B T}{h} e^{-\frac{\Delta G^{\neq}}{RT}} \quad (24) \longrightarrow \ln\frac{k}{T} = -\frac{\Delta H^{\neq}}{R}\cdot\frac{1}{T} + \ln\frac{k_B}{h} + \frac{\Delta S^{\neq}}{R} \quad (25)$$

Gold-nanoparticles coated with thiols **2** or **4** gives lower values for the free energy (ΔG) of the transition state at 40 °C (313 K) as reported in Table 9. It reveals that those systems are able to stabilize better the transition state which suggest a stronger interaction between the dianionic transition state and the metal complexes. The source of higher stability of the transition state arises from the decrease of polarity environment on the monolayer pseudophase as in line with Brown's observations. The small difference between the most reactive systems ($MPGN_2$ and $MPGN_4$) and the less ones ($MPGN_1$ and $MPGN_3$) is normal for accelerations spanning 1 order of magnitude.

Table 9. $\Delta H^{\ddagger}$, $\Delta S^{\ddagger}$ and $T\Delta S^{\ddagger}$ (T = 313 K) values obtained from the Eyring plots of $\boldsymbol{k_{cat}}$ values (see Tables 5 - 8) measured in the interval 30-52 °C for $MPGN_{1-4}$ and Zn(II).

MPGN	$\Delta\mathbf{H}^{\ddagger}$ (KJ*mol)	$\Delta\mathbf{S}^{\ddagger}$ ($J*mol^{-1}*K^{-1}$)	$\mathbf{T}*\Delta\mathbf{S}^{\ddagger}$ ($KJ*mol^{-1}$)	$\Delta\mathbf{G}^{\ddagger}_{40}$ ($KJ*mol^{-1}$)
1	69.7 ± 3.3	-51 ± 10	-15.9 ± 3.1	85.6 ± 6.4
2	63.4 ± 1.0	-56.0 ± 3.3	-17.5 ± 1.0	80.9 ± 2.0
3	67.7 ± 1.1	-61.8 ± 3.4	-19.4 ± 1.1	87.1 ± 2.1
4	64.4 ± 1.1	-53.4 ± 3.6	-16.7 ± 1.1	81.1 ± 2.2

Note: data at 25°C were not used in the fit since they appear outlier when residual analysis is applied.

Moreover, as highlighted in figure 85, the larger reactivity of $MPGN_2$ and $MPGN_4$ has a prevalent enthalpic origin, being the activation entropy quite similar in all cases.

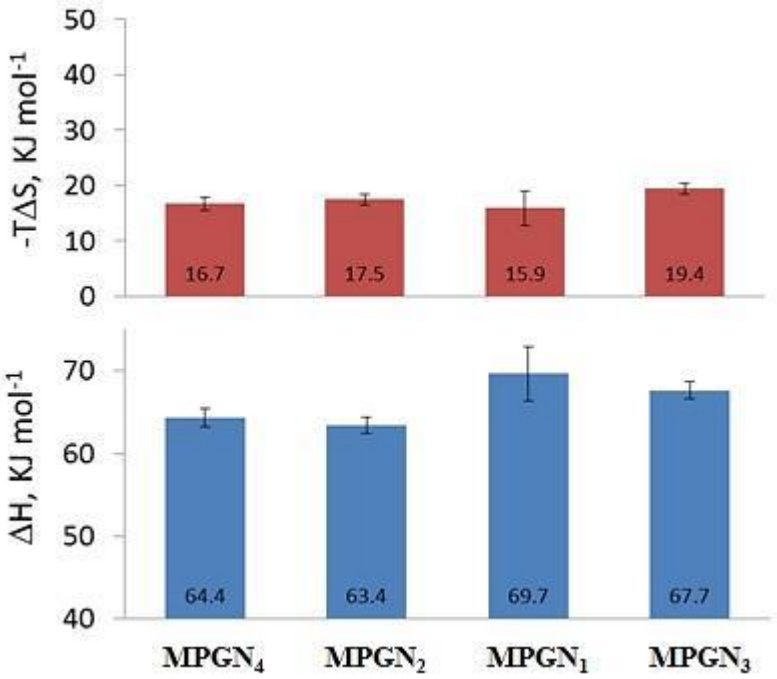

Figure 85. $\Delta H^{\ddagger}$ (blue) and $-T\Delta S^{\ddagger}$ (red, T = 313 K) values obtained from the Eyring plots of $\boldsymbol{k_{cat}}$ values measured in the interval 30-52 °C for $MPGN_{1\text{-}4}$ and Zn(II). Conditions: [AuNp, in thiol units] = 2.0×10^{-5} M, [Zn(II)] = 2.0×10^{-5} M, [buffer] = 1.0×10^{-2} M, pH = 7.5.

3.6 Measurements of the polarity environment

The differences in transition state stabilization could be explained by a stronger interaction between the dianionic transition state and the cationic metal ion. This stabilization is maximize in low polarity environments, as demonstrated by Brown and coworkers[25], and it is hence possible to suppose that nanozymes reactivity can be explained by the lower polarity of the monolayer pseudophase, which in turn enhances the metal-phosphate interaction and accelerates the reaction.

The measurement of the monolayer polarity was however not so trivial. First at all, fluorescence-based probes could not be used since the well-known characteristic of the

gold core of acting as a fluorescence quencher. Also solvatochromic probes proved to be ineffective since we cannot be sure that the polarity probe really goes into the monolayer and we do not measure the polarity of the bulk solution.

After trying with different polarity probes, we found a good compromise by using the polarity probe 6-nitrobenzisoxazole-3-carboxylate (6-NBIC)[63] generally used to measure the polarity of ionic liquid or micelles[64].

3.6.1. Polarity measurements with 6-NBIC

The 6-nitrobenzisoxazole-3-carboxylate (6-NBIC) is a polarity probe that undergoes a spontaneous decarboxylation reaction that occurs faster in low polarity environments. This behavior is due to the fact that the NBIC negative charge is delocalized over all molecule in the transition state but localized on the carboxylate in the starting material. Consequently, high polarity environments, like water, stabilize the reagent better than the transition state, making the reaction slower. Low polarity environments, on the other hand, stabilize the transition state better than the reagent, and the reaction becomes faster. The reaction is easy follow by absorbance since it produces a colorful product.

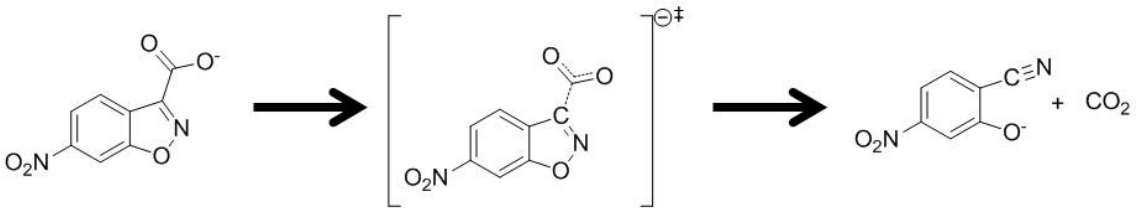

Figure 86. Reaction of decarboxylation of the 6-nitrobenzisoxazole-3-carboxylate.

6-NBIC decarboxylation rate experiments where started by adding the required amount of a freshly prepared 0.01 M solution of substrate (NBIC) in methanol to a 1-mL solution containing the appropriate buffer (0.01 M), $Zn(NO_3)_2$, and **MPGN$_{1\text{-}4}$** ([TACN-Zn^{II}] = 2.0 x 10^{-5} M). Substrate conversion was monitored by following the absorption of 2-cyano-5-nitrophenolate at 395 nm. Kinetic profiles (90% of substrate conversion) were fitted according to first order kinetic integrated law (26):

$$A = A_0 + A_\infty (1 - e^{-k_\psi t}) \qquad (26)$$

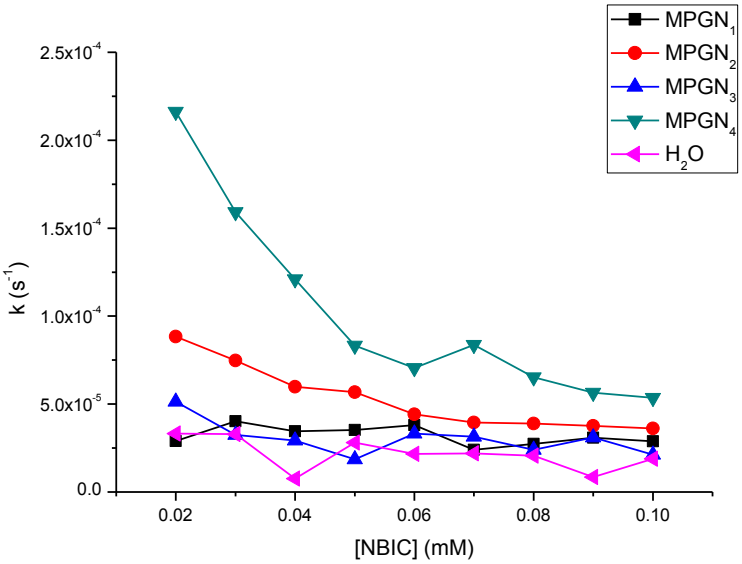

Figure 87. First order rate constants versus the concentration of NBIC for the reaction of decarboxylation of the NBIC in the presence of Zn(II) complexes of $MPGN_{1\text{-}4}$ and H_2O. Conditions: [TACN-Zn(II)] = 2.0×10^{-5} M, [buffer] = 1.0×10^{-2} M, pH 7.5, T = 25 °C.

A carefully investigation of figure 87 shows that as the NBIC concentration increases its decarboxylation rate converges to that observed in buffered water. As a consequence, the first order rate for the NBIC decarboxylation was extrapolated at [NBIC] = 0 in which we ensure that an infinitesimal amount of NBIC is on the nanoparticle surface and, hence, we remove the contribution to the decarboxylation rate of the unbound NBIC.

Table 10. First order rate for the NBIC spontaneous decarboxylation in the presence of $MPGN_{1\text{-}4}$ and Zn(II) in water at pH 7.5 and 25 °C, extrapolated at [NBIC] = 0.

MPGN	1	2	3	4	5
k_{NBIC} ($\times 10^{-5}$ s^{-1})	3.0 ± 0.9	10.8 ± 0.7	6.8 ± 0.8	29.8± 1.2	4.0 ± 2.2

Conditions: [TACN-Zn(II)] = 2.0×10^{-5} M, [buffer] = 1.0×10^{-2} M, pH 7.5, T = 25 °C.

3.7 Discussion

In the present chapter we have demonstrated how small modifications in the nanoparticles coating thiols produce remarkable accelerations in the nanoparticles reactivity by modifying the polarity environment where the phosphate cleavage reaction takes places.

Figure 88 summarized the reactivity data for the best performing bimetallic systems so far reported for HPNP cleavage. Richard and Morrow[21] bimetallic complex **4** is based on the same triazacyclononane metal chelating unit we used for our nanozymes. When its reactivity is compared with that of MPGN**1**, it appears evident that the higher activity of the nanoparticles arises substantially form higher substrate affinity. As recently demonstrated by Prins[65], such a decrease in K_M values is due to the multivalency of the nanoparticles. The number of potential bimetallic binding sites is statistically increased and this causes an apparent increase in binding affinity.

Beside increased affinity, the intrinsic reactivity (k_{cat}) of the two systems is similar indicating that in both the cases the optimal (or the best possible) reactive site organization is reached and that the reaction occurs in a similar environment. It should be noted that such an optimally preorganized active site is reached in the nanoparticle monolayer without the need of the bridging oxygen present in **4**. In methanol such structural element has a detrimental effect on the catalyst reactivity. In fact, complex **6** is 37000 times more reactive than the equivalent one comprising an alkoxy bridge[25]. The bridge may decrease the net charge of the catalyst (decreasing both Lewis acidity and transition state stabilization) or reduce the flexibility of the complex preventing its reorganization during the reaction. In water, the presence of such a bridging alkoxy group is necessary to keep the two metal ions in close proximity, as demonstrated by the fact that **6** becomes a rather poor catalyst in these conditions. It is, however, still unclear whether this gain in organization of the catalysts pays a reactivity cost also in this solvent. The fact that the k_{cat} value we here measured for MPGN**1** is similar to that of **4** indicates that the detrimental effect of the alkoxy bridge may be smaller in water than in methanol.

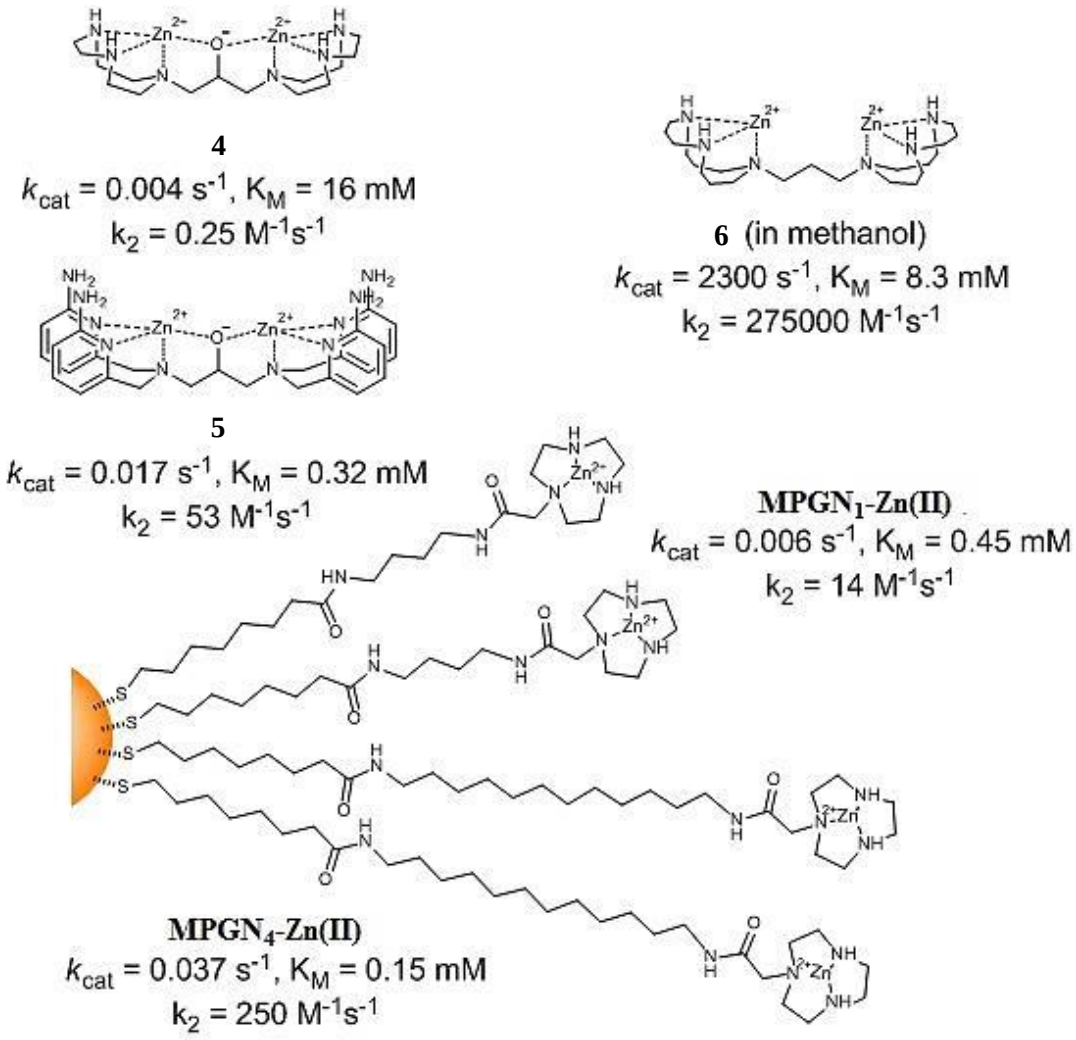

Figure 88. Structure and reactivity parameters (at 25°C) for different HPNP cleaving bimetallic systems reported in literature of studied in this work. But for catalyst 7, all the rest were studied in water.

Eventually, when the reactivity of $MPGN_4$ is examined, the advantage of nanozymes clearly emerges, as the decrease of medium polarity is awarded by a 10-fold increase of k_{cat}. Remarkably, the reactivity parameters of these nanoparticles are, although to not such a large extent, better also when compared with Williams' bimetallic complex **5**[22], the current benchmark for HPNP cleavage in water, where the reactivity arises from highly efficient cooperation between metal ions and H-bond donors.

Admittedly, when the comparison is made with Brown bimetallic complex **6** in methanol, as already pointed out, the reactivity of $MPGN_4$ is at least 3 orders of magnitude lower.

Interestingly, when Michaelis−Mentenparameters for **4** and **6** are compared, it appears quite evident that moving the reaction from water to methanol affects morereactivity (k_{cat}) than binding (K_M). The same occurs in the nanoparticles series MPGN**$_{1\text{-}4}$**, supporting the hypothesis that the activity increase observed is related to a decrease of local medium polarity at the reaction site. The huge difference observed between k_{cat} values of MPGN**$_4$** (in water) and catalyst **6** (in methanol) indicates that such a polarity decrease is quite small, as it may be expected since the reaction is still occurring at the monolayer/water interface, a still highly hydrated region.

In conclusion, we have demonstrated that nanoparticles can be used not only to easily assemble active units capable to cooperate in a reaction taking advantage of their multivalency, but also to modify the local medium in order to tune the reactivity. In this way, nanoparticles offer the possibility to create artificial "binding sites", something long sought in micellar catalysis and rarely found because of the very fast monomer exchange occurring in such aggregates. An analogous medium effect has been also observed with synzymes[66], metal based HPNP-cleaving polymers, but with far lower efficiency due probably to the lack of cooperativity between metal ions shown by these systems. The fact that the rate accelerations here observed in water, although very high, are lower than those reported by Brown while working in nonaqueous solvents indicates that there is still room for improvement of nanozymes reactivity.

3.7 Experimental part

3.8.1. Synthesis of $MPGN_{1-4}$

All the glassware used in the MPGN preparation was washed with aqua regia and rinsed with distilled water. $HAuCl_4$ is strongly hygroscopic and was weighted within a dry-box.

A solution of $HAuCl_4 \cdot 3H_2O$ (50 mg, 0.127 mmol) in water (2 mL) was extracted with a solution of tetraoctylammonium bromide (208 mg, 0.381 mmol) in N_2 purged toluene (125 mL divided in 3 portions). To the resulting reddish-orange organic solution, dioctylamine (0.77 mL, 2.54 mmol) is added (the amount of dioctylamine was calculated in order to obtain 2 nm nanoparticles). The mixture is vigorously stirred under N_2 for 30 min. During this period of time the color of the mixture fades. A solution of $NaBH_4$ (48 mg, 1.27 mmol) in H_2O (1 mL) is then rapidly added. The color of the solution turns rapidly to black due to nanoparticles formation. After 2 hours of stirring, the aqueous layer is removed. To the above nanoparticle solution, the desired thiol (0.059 mmol), dissolved in 2 mL of isopropanol, was rapidly added.

$MPGN_{1-4}$ are soluble in water (prolonged stirring may be required) and were purified by several extraction with organic solvents (2 x toluene, 3 x ethyl acetate, 1 x ethyl ether) and then by gel permeation chromatography with Sephadex G-25 resin.

3.8.1. Synthesis of thiols 1 - 4

Thiol **1-4** were prepared according to the following scheme:

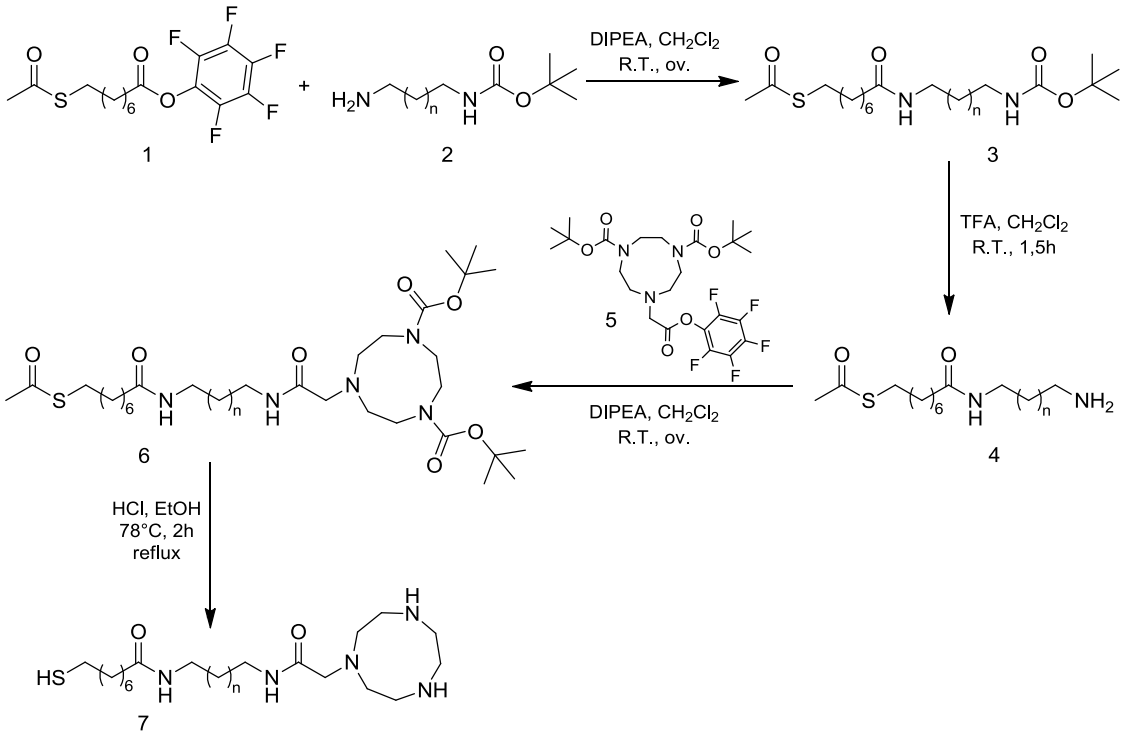

3.8.1.1 perfluorophenyl 8-(acetylthio)octanoate (1)

8-Bromooctanoic acid (2.00 g, 8.96 mmol) was dissolved in acetone (60 mL) and potassium thioacetate (1.33 g, 11.65 mmol) was added. The mixture was refluxed for 48 hours, the solvent was evaporated and the solid residue dissolved in CH_2Cl_2 (20 mL). The organic solution was extracted with water (5 x 20 mL) and dried with Na_2SO_4. After solvent evaporation 1.70 g (87%) of 8-(thioacetyl)-octanoic acidwere obtained as an orange oil. ^{1}H-NMR ($CDCl_3$,300 MHz), δ: 2.86 (t, 2H, 3 Hz, -S-*C*H_2-CH_2-), 2.35 (t, 2H, 3 Hz, -CH_2-*C*H_2-COOH), 2.32 (s, 3H, *C*H_3-CO-S-), 1.60 (m, 4H, -S-CH_2-*C*H_2-$(CH_2)_3$-*C*H_2-CH_2-COOH), 1.30 (m, 6H, -CH_2-(*C*H_2)$_3$-CH_2-).

8-(Thioacety)-octanoic acid (1.70 g, 7.79 mmol) and pentafluorophenol (1.86 g, 10.13 mmol)were dissolved in CH_2Cl_2 (30 mL) and*N*-(3-Dimethylaminopropyl)-*N′*-ethyl-carbodiimide hydrochloride (EDC, 1.94 g, 10.13 mmol) was added.The mixture was stirred for 12 hours under nitrogen. The organic solution was extracted with water (3 x 20 mL)

and dried with Na_2SO_4. After solvent evaporation, the crude product was purified by flash chromatography (silica gel, eluent: CH_2Cl_2/Petroleum Ether 3:7). 2.45 g (82%) of **1** were obtained as a yellow oil.

^{1}H-NMR ($CDCl_3$,300 MHz), δ: 2.86 (t, 2H, 3 Hz, CH_3-CO-S-*CH_2*-CH_2-), 2.65 (t, 2H, 3 Hz, -CH_2-*CH_2*-COOH), 2.32 (s, 3H, *CH_3*-CO-S-), 1.77 (qn, 2H, 3 Hz, -S-CH_2-*CH_2*-$(CH_2)_3$-), 1.58 (qn, 2H, 3 Hz, -$(CH_2)_3$-*CH_2*-CH_2-COOH), 1.37 (m, 6H, -CH_2-(*CH_2*)$_3$-CH_2-).

3.8.1.2 Synthesis of *tert*-butyl (4-aminobutyl)carbamate (n=2) **(2)**

1,4-Diaminobutane (5 g) was dissolved in 100 mL of methanol in a three-necked round-bottomflask. To this solution were slowly added, simultaneously, in a period of 2 h, a suspension of K_2CO_3 (10 g) in 50 mL of methanol and a solution of tert-butoxycarbonylanhydride (11 g, 0.9 equiv) in 25 mL methanol. The suspension was then kept under stirring overnight and filtered, and the solvent was evaporated. The crude oil was dissolved in CH_2Cl_2 (100 mL) and extracted with a 5% aqueous solution of K_2CO_3 (2 x 50 mL) and then with water (2 x 50 mL). The dried organic layer was evaporated, and the collected material was flash chromatography ($CHCl_3$) to give 7 g (65% yield) of *tert*-butyl (4-aminobutyl)carbamate as a colorless liquid. ^{1}H NMR (300 MHz, $CDCl_3$) δ: 3.05 (m, 2H, CH_2-*CH_2*-NH-CO-); 2.64 (t, 2H, 3 Hz, NH_2-*CH_2*-CH_2-); 1.45 (s, 9H, -O-C-*$(CH_3)_3$*); 1.15 (m, 4H, -CH_2-*$(CH_2)_2$*-CH_2-).

Same procedure to synthetize the *tert*-butyl (8-aminooctyl)carbamate (n=6). ^{1}H NMR (300 MHz, MeOD) δ: 3.01 (m, 2H, CH_2-*CH_2*-NH-CO-); 2.91 (t, 2H, 3 Hz, NH_2-*CH_2*-CH_2-); 1.65 (qn, 2H, 3 Hz, -CH_2-*CH_2*- CH_2-NH-CO-); 1.43 (s, 9H, -O-C-*$(CH_3)_3$*), 1.36 (m, 10H, -CH_2-*$(CH_2)_5$*-CH_2-).

Same procedure to synthetize the *tert*-butyl (12-aminododecyl)carbamate (n=10). ^{1}H NMR (300 MHz, $CDCl_3$) δ: 3.10 (m, 2H, CH_2-*CH_2*-NH-CO-); 2.68 (t, 2H, 2 Hz, NH_2-*CH_2*-CH_2-); 1.65 – 1.55 (m, 4H, -CH_2-*CH_2*- $(CH_2)_8$- *CH_2*-CH_2-); 1.45 (s, 9H, -O-C-*$(CH_3)_3$*); 1.35 – 1.20 (m, 16H, -CH_2-CH_2- *$(CH_2)_8$*-CH_2-).

Same procedure to synthetize the *tert*-butyl (2-(2-(2-aminoethoxy)ethoxy)ethyl)carbamate (TEG). ^{1}H NMR (300 MHz, $CDCl_3$) δ: 3.53 (m, 4H, -CH_2-*CH_2*-O-$(CH_2)_2$-O-*CH_2*-CH_2-);

3.44 (m, 4H, -O-*(CH$_2$)$_2$*-O-); 3.22 (m, 2H, -CH$_2$-*CH$_2$*-NH-CO-); 2.78 (t, 2H, NH$_2$-*CH$_2$*-CH$_2$-); 1.35 (s, 9H, -O-C-*(CH$_3$)$_3$*).

3.8.1.3 Synthesis of S-(8-((4-((tert-butoxycarbonyl)amino)butyl)amino)-8-oxooctyl) ethanethioate (n=2) (3)

The compound 2 (200 mg) was dissolved in 10 mL of dry dichloromethane and added dropwise to an ice cold suspension of 5 mL of dimethylformamide containing K_2CO_3 (150 mg) and perfluorophenyl 8-(acetylthio)octanoate (251 mg, 1 equiv).

After 2 h the suspension was filtered, and the solid was washed with dichloromethane. Evaporation of the dried dichloromethane gave 356 mg (86% yield) of S-(8-((4-((*tert*-butoxycarbonyl)amino)butyl)amino)-8-oxooctyl) ethanethioate. ^{1}H NMR (300 MHz, $CDCl_3$) δ: 3.24 (m, 2H, -S-*CH$_2$*-CH$_2$-), 3.11 (m, 2H, -CH$_2$-*CH$_2$*-NH-CO-), 2.83 (t, 2H, 3 Hz, -CO-NH-*CH$_2$*-CH$_2$-), 2.30 (s, 3H, *CH$_3$*-CO-S-), 2.14 (t, 2H, 3 Hz, -CH$_2$-*CH$_2$*-CO-NH-),1.6-1.5 (m, 8H, -S-CH$_2$-*CH$_2$*-(CH$_2$)$_3$-*CH$_2$*-CH$_2$-CO-NH- and -CH$_2$-*(CH$_2$)$_2$*-CH$_2$-), 1.45 (s, 9H, -O-C-*(CH$_3$)$_3$*), 1.3 – 1.1 (m, 6H, -S-CH$_2$-CH$_2$-*(CH$_2$)$_3$*-CH$_2$-CH$_2$-CO-NH-).

Same procedure to synthetize the S-(8-((8-((tert-butoxycarbonyl)amino)octyl)amino)-8-oxooctyl) ethanethioate (n=6). ^{1}H NMR (300 MHz, $CDCl_3$) δ: 3.20 (q, 2H, 3Hz, -S-*CH$_2$*-CH$_2$-), 3.05 (q, 2H, 3 Hz, -CH$_2$-*CH$_2$*-NH-CO-), 2.81 (t, 2H, 3 Hz, -CO-NH-*CH$_2$*-CH$_2$-), 2.28 (s, 3H, *CH$_3$*-CO-S-), 2.11 (t, 2H, 3 Hz, -CH$_2$-*CH$_2$*-CO-NH-),1.6-1.5 (m, 8H, -S-CH$_2$-*CH$_2$*-(CH$_2$)$_3$-*CH$_2$*-CH$_2$-CO-NH- and -CH$_2$-*CH$_2$*-(CH$_2$)$_4$-*CH$_2$* -CH$_2$-), 1.45 (s, 9H, -O-C-*(CH$_3$)$_3$*), 1.4 – 1.2 (m, 14H, -S-CH$_2$-CH$_2$-*(CH$_2$)$_3$*-CH$_2$-CH$_2$-CO-NH- and -CH$_2$-CH$_2$-*(CH$_2$)$_4$*-CH$_2$ -CH$_2$-).

Same procedure to synthetize the S-(8-((12-((tert-butoxycarbonyl)amino)dodecyl)amino)-8-oxooctyl) ethanethioate (n=10). ^{1}H NMR (300 MHz, $CDCl_3$) δ: 3.24 (q, 2H, 3Hz, -S-*CH$_2$*-CH$_2$-), 3.10 (q, 2H, 3 Hz, -CH$_2$-*CH$_2$*-NH-CO-), 2.85 (t, 2H, 3 Hz, -CO-NH-*CH$_2$*-CH$_2$-), 2.32 (s, 3H, *CH$_3$*-CO-S-), 2.15 (t, 2H, 3 Hz, -CH$_2$-*CH$_2$*-CO-NH-),1.6-1.5 (m, 8H, -S-CH$_2$-*CH$_2$*-(CH$_2$)$_3$-*CH$_2$*-CH$_2$-CO-NH- and -CH$_2$-*CH$_2$*-(CH$_2$)$_8$-*CH$_2$* -CH$_2$-); 1.44 (s, 9H, -O-C-*(CH$_3$)$_3$*); 1.4 – 1.2 (m, 22H, , -S-CH$_2$-CH$_2$-*(CH$_2$)$_3$*-CH$_2$-CH$_2$-CO-NH- and -CH$_2$-CH$_2$-*(CH$_2$)$_8$*-CH$_2$ -CH$_2$-).

Same procedure to synthetize the S-(2,2-dimethyl-4,15-dioxo-3,8,11-trioxa-5,14-diazadocosan-22-yl) ethanethioate (TEG). ^{1}H NMR (300 MHz, $CDCl_3$) δ: 3.60 (m, 4H, -CH_2-*CH_2*-O-$(CH_2)_2$-O-*CH_2*-CH_2-); 3.55 (t, 4H, 2 Hz, -O-*$(CH_2)_2$*-O-); 3.46 (t, 2H, 2 Hz, CO-NH-*CH_2*-CH_2-); 3.30 (q, 2H, 2 Hz, -S-*CH_2*-CH_2-); 2.84 (t, 2H, 3 Hz, -O-CH_2-*CH_2*-NH-CO-); 2.31 (s, 3H, *CH_3*-CO-S-); 2.17 (t, 2H, 3 Hz, -CH_2-*CH_2*-CO-NH-); 1.70 – 1.50 (m, 4H, -S-CH_2-*CH_2*-$(CH_2)_3$-*CH_2*-CH_2-CO-NH-); 1.44 (s, 9H, -O-C-*$(CH_3)_3$*); 1.35 – 1.20 (m, 6H, -S-CH_2-CH_2-*$(CH_2)_3$*-CH_2-CH_2-CO-NH-).

3.8.1.4 Synthesis of S-(8-((4-aminobutyl)amino)-8-oxooctyl) ethanethioate (n=2) (4)

The compound was dissolved in CH2Cl2 (5 mL) and 3 mL of trifluoroacetic acid (TFA) were added. The reaction mixture was stirred at R.T. for 1.30h. The solvent was evaporated and the crude of the reaction was obtain as a white salt used in the following step without puritification. ^{1}H NMR (300 MHz, $CDCl_3$) δ: 3.38 (q, 2H, 2 Hz, -S-*CH_2*-CH_2-), 3.24 (m, 2H, -CH_2-*CH_2*-NH-CO-), 2.88 (t, 2H, 3 Hz, -CO-NH-*CH_2*-CH_2-), 2.39 (s, 3H, *CH_3*-CO-S-), 2.36 (t, 2H, 3 Hz, -CH_2-*CH_2*-CO-NH-),1.6-1.5 (m, 8H, -S-CH_2-*CH_2*-$(CH_2)_3$-*CH_2*-CH_2-CO-NH- and -CH_2-*$(CH_2)_2$*-CH_2-), 1.3 – 1.1 (m, 6H, -S-CH_2-CH_2-*$(CH_2)_3$*-CH_2-CH_2-CO-NH-).

Same procedure to synthetize the S-(8-((8-aminooctyl)amino)-8-oxooctyl) ethanethioate (n=6). ^{1}H NMR (300 MHz, MeOD) δ: 3.16 (t, 2H, 3 Hz, -S-*CH_2*-CH_2-); 2.95 – 2.80 (m, 4H, -CO-NH-*CH_2*-CH_2- and -CH_2-*CH_2*-NH_2); 2.29 (s, 3H, *CH_3*-CO-S-); 2.17 (t, 2H, -CH_2-*CH_2*-CO-NH-);1.70 – 1.45 (m, 8H, -S-CH_2-*CH_2*-$(CH_2)_3$-*CH_2*-CH_2-CO-NH- and -CH_2-*CH_2*-$(CH_2)_4$-*CH_2* -CH_2-); 1.40 – 1.25 (m, 14H, -S-CH_2-CH_2-*$(CH_2)_3$*-CH_2-CH_2-CO-NH- and -CH_2-CH_2-*$(CH_2)_4$*-CH_2 -CH_2-).

Same procedure to synthetize the S-(8-((12-aminododecyl)amino)-8-oxooctyl) ethanethioate (n=10).^{1}H NMR (300 MHz, MeOD) δ: 3.20 (q, 2H, 3 Hz, -S-*CH_2*-CH_2-); 2.95 – 2.80 (m, 4H, -CO-NH-*CH_2*-CH_2- and -CH_2-*CH_2*-NH_2); 2.32 (s, 3H, *CH_3*-CO-S-); 2.17 (t, 2H, -CH_2-*CH_2*-CO-NH-);1.70 – 1.45 (m, 8H, -S-CH_2-*CH_2*-$(CH_2)_3$-*CH_2*-CH_2-CO-NH- and -CH_2-*CH_2*-$(CH_2)_4$-*CH_2* -CH_2-); 1.40 – 1.20 (m, 22H, -S-CH_2-CH_2-*$(CH_2)_3$*-CH_2-CH_2-CO-NH- and -CH_2-CH_2-*$(CH_2)_8$*-CH_2 -CH_2-).

Same procedure to synthetize the S-(8-((2-(2-(2-aminoethoxy)ethoxy)ethyl)amino)-8-oxooctyl) ethanethioate (TEG).[1]H NMR (300 MHz, $CDCl_3$) δ: 3.76 (t, 2H, 2 Hz, -O-*CH_2*-CH_2-NH_2); 3.70 – 3.60 (m, 6H, CH_2-*CH_2*-O-*$(CH_2)_2$*-O-); 3.50 (m, 2H, -O-CH_2-*CH_2*-NH_2); 3.27 (q, 2H, 2 Hz, -S-*CH_2*-CH_2-); 2.85 (t, 2H, 3 Hz, -CO-NH-*CH_2*-CH_2-O-); 2.33 (s, 3H, *CH_3*-CO-S-); 2.30 (t, 2H, 3 Hz, -CH_2-*CH_2*-CO-NH-); 1.65 – 1.45 (m, 4H, -S-CH_2-*CH_2*-$(CH_2)_3$-*CH_2*-CH_2-CO-NH-); 1.40 – 1.20 (m, 6H, -S-CH_2-CH_2-*$(CH_2)_3$*-CH_2-CH_2-CO-NH-).

3.8.1.5 Synthesis of di-*tert*-butyl 7-(2-oxo-2-(perfluorophenoxy)ethyl)-1,4,7-triazonane-1,4-dicarboxylate (5)

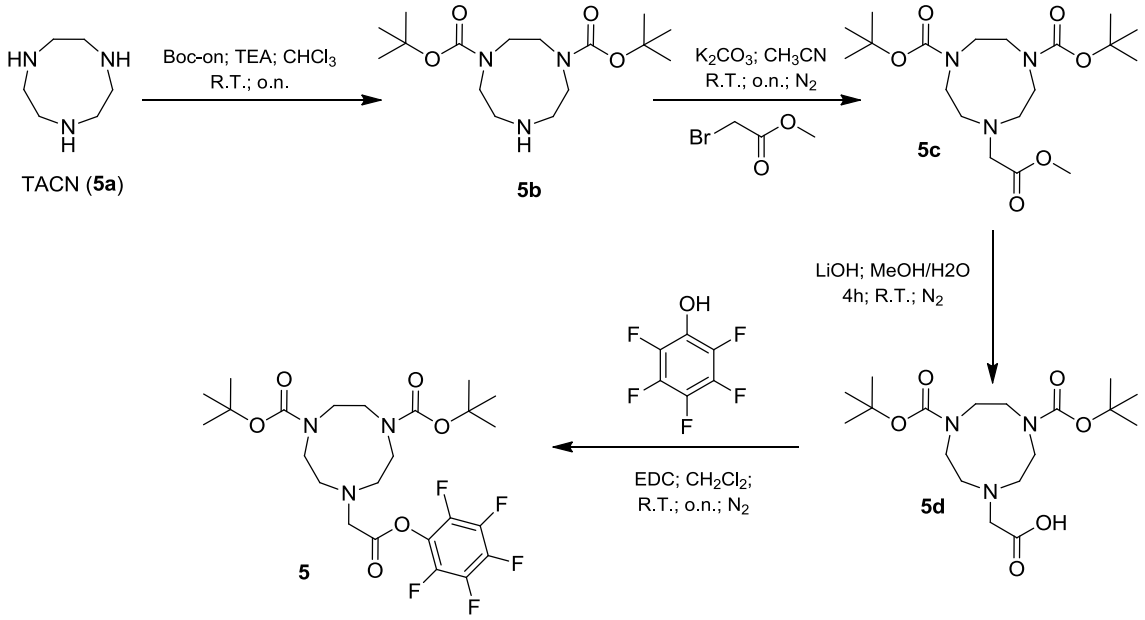

[2-(tert-butoxycarbonyloxyimino)-2-phenylacetonitrile] (Boc-on, 5.7 g, 23.2 mmol) dissolved in anhydrous $CHCl_3$ (20 mL) was injected by syringe pump (1 mL/h, 20 h, RT) in a solution of 1,4,7-triazaciclononane **5a** (TACN, 1.5 g, 11.6 mmol) with triethylamine (TEA, 4.8 mL, 34.5 mmol) in anhydrous $CHCl_3$ (50 mL). Solution was stirred for 2 extra hours, solvent was evaporated. The residue was washed with 3 x 10 mL $NaCO_3$ 5% aqueous solution. Then 2 x 20 mL brine, then 3 x 10 mL citric acid 10% aqueous solution. The aqueous phase (acidic) was treated with NaOH aqueous solution to pH 11, then extracted with $CHCl_3$. The organic phase was evaporated and the *di-tert-butyl 1,4,7-triazonane-1,4-dicarboxylate***5b** (60%) was collected pure. [1]H-NMR ($CDCl_3$,300 MHz), δ:

3.45 (m, 4H, -CO-N-*CH_2*-*CH_2*-N-CO-), 3.25 (m, 4H, -CH_2-*CH_2*-N-(CH_2)-N-*CH_2*-CH_2-), 2.90 (m, 4H, -CH_2-*CH_2*-NH-*CH_2*-CH_2-), 1.45 (s, 18H, 2 x -O-C-*$(CH_3)_3$*).

The previous compound **5b** (350 mg, 1.06 mmol) was dissolve in 30 mL CH_3CN containing K_2CO_3 (176 mg, 1.27 mmol). Methyl bromoacetate (0.10mL, 1.06 mmol) was added. The mixture was stirred overnight at R.T. under N_2 atmosphere. The solvent was evaporated and the crude oil was purified by flash chromatography (Petroleum ether/ Ethyl acetate 80:20) to give 300 mg (70% yield) of *di-tert-butyl 7-(2-methoxy-2-oxoethyl)-1,4,7-triazonane-1,4-dicarboxylate***5c** as a colorless oil. ^{1}H-NMR ($CDCl_3$,300 MHz), δ: 3.65 (t, 3H, 2Hz, -CO-O-*CH_3*), 3.45 (t, 2H, 2 Hz, -N-*CH_2*-CO-); 3.40 (m, 4H, -CO-N-*CH_2*-*CH_2*-N-CO-), 3.25 (m, 4H, -CH_2-*CH_2*-N-(CH_2)-N-*CH_2*-CH_2-), 2.90 (m, 4H, -CH_2-*CH_2*-N-*CH_2*-CH_2-), 1.45 (s, 18H, 2 x -O-C-*$(CH_3)_3$*).

The previous compound **5c** (300 mg, 0.75 mmol) was dissolved in 10 mL of MeOH and a solution of LiOH (71.85 mg, 3.00 mmol) in 4 mL of H_2O was added. The reaction was stirred for 4h at R.T. under N_2. The methanol was evaporated and the aqueous phase was treated with $KHSO_4$ 10% aqueous solution to pH 3. The product precipitated was extracted with ethyl acetate 3 x 15 mL. The organic phase was dried with $MgSO_4$ and evaporated. The compound 2-(4,7-bis(tert-butoxycarbonyl)-1,4,7-triazonan-1-yl)acetic acid **5d** was obtained as a white solid (>95%).^{1}H-NMR ($CDCl_3$,300 MHz), δ: 3.60 – 3.20 (m, 10H, -N-*CH_2*-CO- and -CO-N-*CH_2*-*CH_2*-N-CO- and -CH_2-*CH_2*-N-(CH_2)-N-*CH_2*-CH_2-), 2.70 (m, 4H, -CH_2-*CH_2*-N-*CH_2*-CH_2-), 1.45 (s, 18H, 2 x -O-C-*$(CH_3)_3$*).

The previous compound **5d** (280 mg, 0.72 mmol) and pentafluorophenol (213 mg, 1.16 mmol)were dissolved in CH_2Cl_2 (5 mL) and*N*-(3-Dimethylaminopropyl)-*N′*-ethyl-carbodiimide hydrochloride (EDC, 222 mg, 1.16 mmol) was added.The mixture was stirred for 12 hours under nitrogen. The organic solution was extracted with a mixture of $KHSO_4$/Brine 1:1 (4 x 5 mL) and dried with $MgSO_4$. The compound **5** di-tert-butyl 7-(2-oxo-2-(perfluorophenoxy)ethyl)-1,4,7-triazonane-1,4-dicarboxylate (80%) was obtained as a brown oil. %).^{1}H-NMR ($CDCl_3$,300 MHz), δ: 3.84 (s, 2H, -N-*CH_2*-CO-), 3.45 (m, 4H, -CO-N-*CH_2*-*CH_2*-N-CO-), 3.30 (m, 4H, -CH_2-*CH_2*-N-(CH_2)-N-*CH_2*-CH_2-), 2.90 (m, 4H, -CH_2-*CH_2*-N-*CH_2*-CH_2-), 1.45 (s, 18H, 2 x -O-C-*$(CH_3)_3$*).

3.8.1.6 Synthesis of di-*tert*-butyl 7-(2-((4-(8-(acetylthio)octanamido)butyl)amino)-2-oxoethyl)-1,4,7-triazonane-1,4-dicarboxylate (n=2) (6)

Compound **4** (-, 0.45 mmol) was dissolved in 10 mL of CH_2Cl_2 to which were added di-tert-butyl 7-(2-oxo-2-(perfluorophenoxy)ethyl)-1,4,7-triazonane-1,4-dicarboxylate (compound 5, 250 mg, 0.45 mmol) dissolved in 2 mL of CH_2Cl_2. Under a N_2 stream, N,N-Diisopropylethylamine was added (DIPEA, 470μL, 2.7 mmol). The reaction was left to stir overnight at R.T. After this time, the solvent was evaporated and the crude product was purified by flash chromatography ($CHCl_3$/MeOH 98:2) to give 230 mg of the compound **6** (yield 70%). ^{1}H NMR (300 MHz, $CDCl_3$) δ:) δ: 3.50 – 3.10 (m, 14H, -CO-NH-*CH_2*-$(CH_2)_4$-*CH_2*-NH-CO- and -N-*CH_2*-CO- and -CH_2-*CH_2*-N-*$(CH_2)_2$*-N-*CH_2*-CH_2-), 2.80 (t, 2H, 2Hz, -S-*CH_2*-CH_2-), 2.61 (br, 4H, CH_2-*CH_2*-N-*CH_2*-CH_2-), 2.27 (s, 3H, *CH_3*-CO-S-), 2.11 (t, 2H, 2Hz, -CH_2-*CH_2*-CO-NH-), 1.55 – 1.35 (m, 26H, -S-CH_2-*CH_2*-$(CH_2)_3$-*CH_2*-CH_2-CO- and -NH-CH_2-*$(CH_2)_2$*-CH_2-NH- and 2 x -O-C-*$(CH_3)_3$*), 1.35 – 1.20 (m, 6H, -S-CH_2-CH_2-*$(CH_2)_3$*-CH_2-CH_2-CO-).^{13}C-NMR ($CDCl_3$, 75.5 MHz, ^{1}H decoupled), δ: 196.2, 173.7, 172.2, 156.7, 155.9, 80.5, 80.1, 63.3, 63.0, 55.0, 54.1, 51.4, 50.7, 50.1, 48.9, 48.2, 39.2, 38.7, 36.6, 30.7, 29.5, 29.1, 28.8, 28.6, 27.4, 26.3, 25.1.

ESI-MS (m/z): 659 [100%, M^++H^+]; 680 [97%, M^++Na^+]

Same procedure to synthetize the di-*tert*-butyl 7-(2-((8-(8-(acetylthio)octanamido)octyl)amino)-2-oxoethyl)-1,4,7-triazonane-1,4-dicarboxylate (n=6). ^{1}H NMR (300 MHz, $CDCl_3$) δ: 3.45 (br, 2H, -N-*CH_2*-CO-), 3.40 – 3.10 (m, 12H, -CO-NH-*CH_2*-$(CH_2)_6$-*CH_2*-NH-CO- and -CH_2-*CH_2*-N-*$(CH_2)_2$*-N-*CH_2*-CH_2-), 2.81 (t, 2H, 2Hz, -S-*CH_2*-CH_2-), 2.62 (br, 4H, CH_2-*CH_2*-N-*CH_2*-CH_2-), 2.28 (s, 3H, *CH_3*-CO-S-), 2.11 (t, 2H, 2Hz, -CH_2-*CH_2*-CO-NH-), 1.57 (q, 2H, 2Hz, -S-CH_2-*CH_2*-CH_2-), 1.50 – 1.35 (m, 24H, -CH_2-*CH_2*-CH_2-CO- and -NH-CH_2-*CH_2*-$(CH_2)_4$-*CH_2*-CH_2-NH- and 2 x -O-C-*$(CH_3)_3$*), 1.35 – 1.20 (m, 14H, -S-CH_2-CH_2-*$(CH_2)_3$*-CH_2-CH_2-CO-NH- and -CH_2-CH_2-*$(CH_2)_4$*-CH_2 -CH_2-). ^{13}C-NMR (CH_3OD, 75.5 MHz, ^{1}H decoupled), δ: 196.2, 173.3, 171.7, 156.5, 155.9, 80.4, 80.1, 62.9, 54.9, 54.0, 50.8, 50.2, 49.0, 48.4, 39.6, 39.3, 36.8, 30.7, 29.9, 29.6, 29.5, 29.2, 29.1, 29.0, 28.8, 28.6, 28.5, 26.9, 26.8, 25.6.

ESI-MS (m/z): 715 [100%, M^++H^+]; 737 [40%, M^++Na^+]

Same procedure to synthetize the di-*tert*-butyl 7-(2-((12-(8-(acetylthio)octanamido)dodecyl)amino)-2-oxoethyl)-1,4,7-triazonane-1,4-dicarboxylate (n=10). ^{1}H NMR (300 MHz, $CDCl_3$) δ: 3.45 (br, 2H, -N-*CH_2*-CO-), 3.40 – 3.10 (m, 12H, -CO-NH-*CH_2*-$(CH_2)_6$-*CH_2*-NH-CO- and -CH_2-*CH_2*-N-*$(CH_2)_2$*-N-*CH_2*-CH_2-), 2.81 (t, 2H, 2Hz, -S-*CH_2*-CH_2-), 2.62 (br, 4H, CH_2-*CH_2*-N-*CH_2*-CH_2-), 2.27 (s, 3H, *CH_3*-CO-S-), 2.10 (t, 2H, 2Hz, -CH_2-*CH_2*-CO-NH-), 1.57 (q, 2H, 2Hz, -S-CH_2-*CH_2*-CH_2-), 1.50 – 1.35 (m, 24H, -CH_2-*CH_2*-CH_2-CO- and -NH-CH_2-*CH_2*-$(CH_2)_8$-*CH_2*-CH_2-NH- and 2 x -O-C-*$(CH_3)_3$*), 1.35 – 1.20 (m, 22H, -S-CH_2-CH_2-*$(CH_2)_3$*-CH_2-CH_2-CO-NH- and -CH_2-CH_2-*$(CH_2)_8$*-CH_2 -CH_2-). ^{13}C-NMR (CH_3OD, 75.5 MHz, ^{1}H decoupled), δ: 196.1, 173.1, 171.4, 156.5, 155.7, 80.4, 80.0, 62.8, 54.8, 54.0, 50.8, 50.2, 49.0, 48.3, 39.6, 36.8, 30.7, 30.0, 29.7, 29.6, 29.5, 29.4, 29.3, 29.3, 29.1, 29.0, 28.8, 28.6, 27.1, 27.0, 25.8.
ESI-MS (m/z): 771 [100%, M^++H^+]; 792 [20%, M^++Na^+].

Same procedure to synthetize the di-*tert*-butyl 7-(2,13,22-trioxo-6,9-dioxa-21-thia-3,12-diazatricosyl)-1,4,7-triazonane-1,4-dicarboxylate(TEG). ^{1}H NMR (300 MHz, $CDCl_3$) δ: 3.65 – 3.10 (m, 22H, -NH-(*CH_2*)-O-*$(CH_2)_2$*-O-*$(CH_2)_2$*-NH- and -N-*CH_2*-CO- and -CH_2-*CH_2*-N-*$(CH_2)_2$*-N-*CH_2*-CH_2-), 2.83 (t, 2H, 2Hz, -S-*CH_2*-CH_2-), 2.62 (br, 4H, CH_2-*CH_2*-N-*CH_2*-CH_2-), 2.30 (s, 3H, *CH_3*-CO-S-); 2.18 (t, 2H, 2Hz, -CH_2-*CH_2*-CO-NH-), 1.60 (q, 2H, 2Hz, -S-CH_2-*CH_2*-CH_2-), 1.54 (q, 2H, 2Hz, -CH_2-*CH_2*-CH_2-CO-), 1.50 – 1.40 (br, 18H, 2 x -O-C-*$(CH_3)_3$*), 1.35 – 1.25 (m, 6H, -S-CH_2-CH_2-*$(CH_2)_3$*-CH_2-CH_2-CO-). ^{13}C-NMR (CH_3OD, 75.5 MHz, ^{1}H decoupled), δ: 196.2, 173.6, 172.0, 156.4, 155.9, 80.4, 70.4, 70.3, 70.2, 69.8, 62.7, 54.0, 50.1, 49.2, 39.3, 39.2, 39.0, 36.6, 30.8, 29.8, 29.3, 29.2, 29.0, 28.8, 28.7, 28.6, 28.5, 25.7.
ESI-MS (m/z): 719 [60%, M^++H^+]; 741 [100%, M^++Na^+].

3.8.1.7 Synthesis of N-(4-(2-(1,4,7-triazonan-1-yl)acetamido)butyl)-8-mercaptooctanamide (n=2) (7)

0.027 g (0.059 mmol) of **6** were dissolved in ethanol (1.5 mL). A 6 M HCl aqueous solution (1.5 mL) was added and the mixture was stirred at 78 °C for 1.5 hours. The reaction mixture was allowed to cool and the solvent evaporated to obtain 0.026 g (<95%) of **7** ^{1}H NMR (300 MHz, MeOD) δ:3.45 (s, 2H, -N-*CH$_2$*-CO-); 3.30 – 3.10 (m, 12 H, -NH-*CH$_2$*-(CH$_2$)$_2$-*CH$_2$*-NH- and –N-CH$_2$-*CH$_2$*-NH-*(CH$_2$)$_2$*-NH-*CH$_2$*-CH$_2$-N-);2.95 (t, 4H, 3Hz, -CH$_2$-*CH$_2$*-N-*CH$_2$*-CH$_2$-); 2.35 (t, 2H, 3Hz, HS-*CH$_2$*-CH$_2$-); 2.29 (t, 2H, 3Hz, -CH$_2$-*CH$_2$*-CO-NH-); 1.60 – 1.35 (m, 8H, -S-CH$_2$-*CH$_2$*-(CH$_2$)$_3$-*CH$_2$*-CH$_2$-CO- and -NH-CH$_2$-*(CH$_2$)$_2$*-CH$_2$-NH-); 1.30 – 1.15 (m, 6H , -S-CH$_2$-CH$_2$-*(CH$_2$)$_3$*-CH$_2$-CH$_2$-CO-).

Same procedure to synthetize the N-(8-(2-(1,4,7-triazonan-1-yl)acetamido)octyl)-8-mercaptooctanamide (n=6). ^{1}H NMR (300 MHz, MeOD) δ:3.45 (s, 2H, -N-*CH$_2$*-CO-); 3.30 – 3.10 (m, 12 H, -NH-*CH$_2$*-CH$_2$-(CH$_2$)$_4$-CH$_2$-*CH$_2$*-NH- and –N-CH$_2$-*CH$_2$*-NH-*(CH$_2$)$_2$*-NH-*CH$_2$*-CH$_2$-N-);2.95 (t, 4H, 3Hz, -CH$_2$-*CH$_2$*-N-*CH$_2$*-CH$_2$-); 2.40 (t, 2H, 3Hz, HS-*CH$_2$*-CH$_2$-); 2.30 (t, 2H, 3Hz, -CH$_2$-*CH$_2$*-CO-NH-); 1.60 – 1.35 (m, 8H, -S-CH$_2$-*CH$_2$*-(CH$_2$)$_3$-*CH$_2$*-CH$_2$-CO- and -NH-CH$_2$-*CH$_2$*-(CH$_2$)$_4$-*CH$_2$*-CH$_2$-NH-); 1.35 – 1.10 (m, 14H, -S-CH$_2$-CH$_2$-*(CH$_2$)$_3$*-CH$_2$-CH$_2$-CO- and -NH-CH$_2$-CH$_2$-*(CH$_2$)$_4$*-CH$_2$ -CH$_2$-NH-).

Same procedure to synthetize the N-(12-(2-(1,4,7-triazonan-1-yl)acetamido)dodecyl)-8-mercaptooctanamide (n=10). ^{1}H NMR (300 MHz, MeOD) δ:3.42 (s, 2H, -N-*CH$_2$*-CO-); 3.30 – 3.10 (m, 12 H, -NH-*CH$_2$*-CH$_2$-(CH$_2$)$_8$-CH$_2$-*CH$_2$*-NH- and –N-CH$_2$-*CH$_2$*-NH-*(CH$_2$)$_2$*-NH-*CH$_2$*-CH$_2$-N-);2.95 (t, 4H, 3Hz, -CH$_2$-*CH$_2$*-N-*CH$_2$*-CH$_2$-); 2.38 (t, 2H, 3Hz, HS-*CH$_2$*-CH$_2$-); 2.30 (t, 2H, 4Hz, -CH$_2$-*CH$_2$*-CO-NH-); 1.65 – 1.35 (m, 8H, -S-CH$_2$-*CH$_2$*-(CH$_2$)$_3$-*CH$_2$*-CH$_2$-CO- and -NH-CH$_2$-*CH$_2$*-(CH$_2$)$_8$-*CH$_2$*-CH$_2$-NH-); 1.35 – 1.10 (m, 22H, -S-CH$_2$-CH$_2$-*(CH$_2$)$_3$*-CH$_2$-CH$_2$-CO- and -NH-CH$_2$-CH$_2$-*(CH$_2$)$_8$*-CH$_2$ -CH$_2$-NH-).

Same procedure to synthetize the N-(2-(2-(2-(2-(1,4,7-triazonan-1-yl)acetamido)ethoxy)ethoxy)ethyl)-8-mercaptooctanamide (teg). ^{1}H NMR (300 MHz, MeOD) δ: 3.40 – 2.90 (s, 22H, -NH-(*CH$_2$*)-O-*(CH$_2$)$_2$*-O-*(CH$_2$)$_2$*-NH- and -N-*CH$_2$*-CO- and -CH$_2$-*CH$_2$*-N-*(CH$_2$)$_2$*-N-*CH$_2$*-CH$_2$-); 2.74 (t, 4H, 2Hz, -CH$_2$-*CH$_2$*-N-*CH$_2$*-CH$_2$-); 2.15 (t, 2H, 3 Hz, -CH$_2$-*CH$_2$*-CO-NH-); 2.04 (t, 2H, 3Hz, HS-*CH$_2$*-CH$_2$-); 1.40 – 1.15 (m, 4H, -S-CH$_2$-*CH$_2$*-(CH$_2$)$_3$-*CH$_2$*-CH$_2$-CO-); 1.10 – 0.95 (m, 6H, -S-CH$_2$-CH$_2$-*(CH$_2$)$_3$*-CH$_2$-CH$_2$-CO-).

3.9 Appendix

Linear fitting of the ln (k_{cat}/T) vs 1/T applying equation (4) revealed large errors in the parameters determined that could be ascribed to the point at 298.15 K, which appeared to behave as an outlier, as evidenced by Figure 23 where the data relative to AuNp2 is reported.

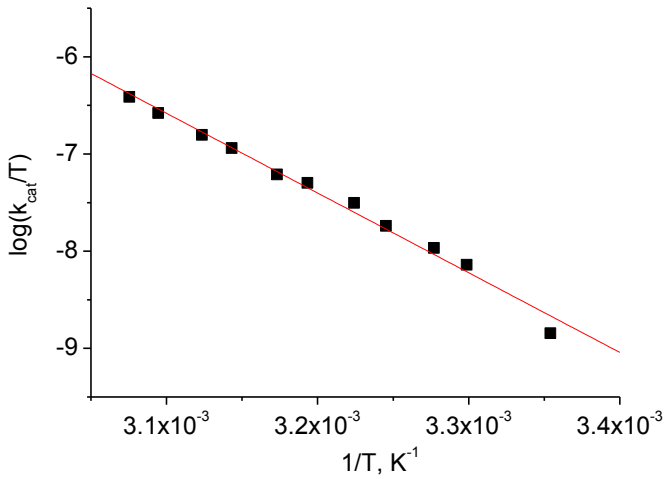

Figure 89. Eyring plot for kcat versus temperature data for the HPNP cleavage by MPGN-2 and Zn(II).

Such suspect is apparently confirmed by residual analysis (Figure 24) that shows that residuals distribution is not randomly scattered and the 25 °C point behave quite differently from the others.

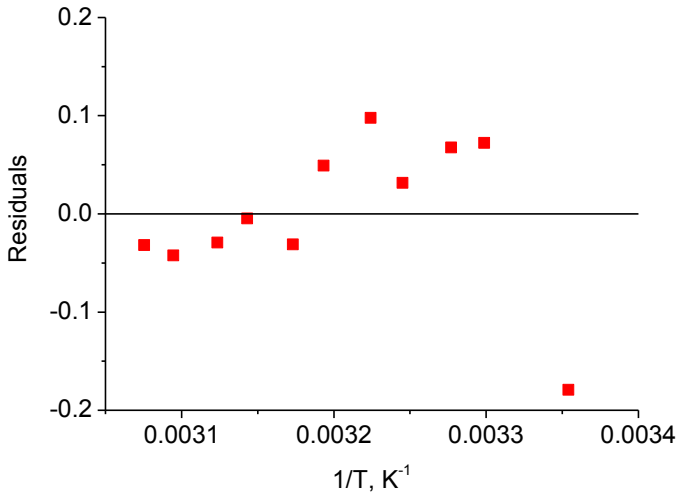

Figure 90. Residual analysis for the data fit reported in Figure 23.

Similar observation can be made for each set of nanoparticles. We have investigated the reason of this behavior, that could be related to an inefficient temperature control. It should be noted that an outlier at one side of the data interval has a substantial effect on the fitting results (this is an intrinsic limitation of the linear fitting with the least squares method). Moreover, the remaining point are numerous enough to allow a good estimation of the thermodynamic parameters. For these reasons, we decided for the exclusion of the 25 °C point from the fitting.

Figure 25 highlights how the exclusion of the 25°C point substantially improves both the quality of the fitting (and fitting parameters errors) and the residuals distribution.

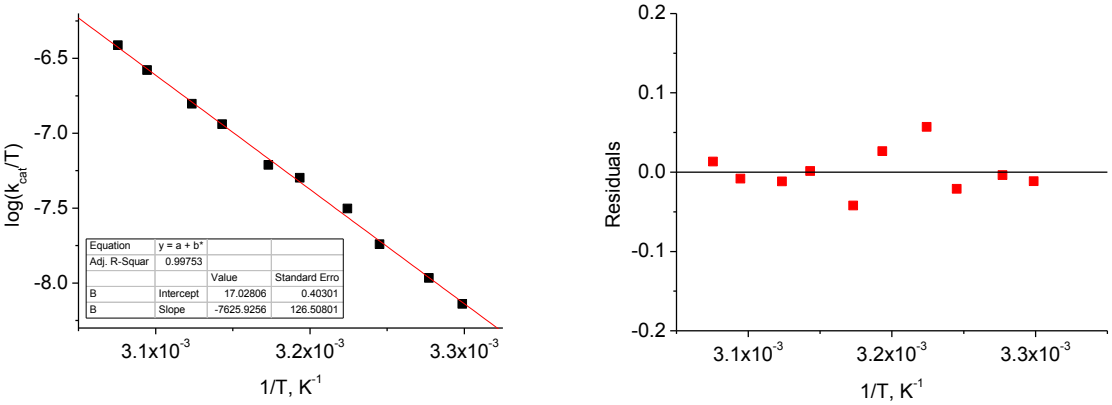

Figure 91. Eyring plot and residual analysis for kcat versus temperature data for the HPNP cleavage by MPGN-2 and Zn(II) without the 25°C point.

The same procedure was applied to all the other nanoparticles with similar results.

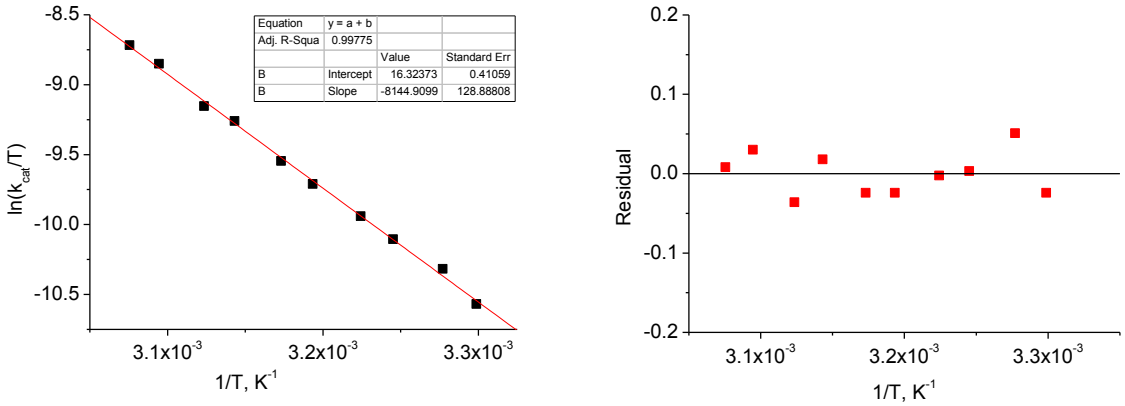

Figure 92. Eyring plot and residual analysis for kcat versus temperature data for the HPNP cleavage by MPGN-3 and Zn(II) without the 25°C point.

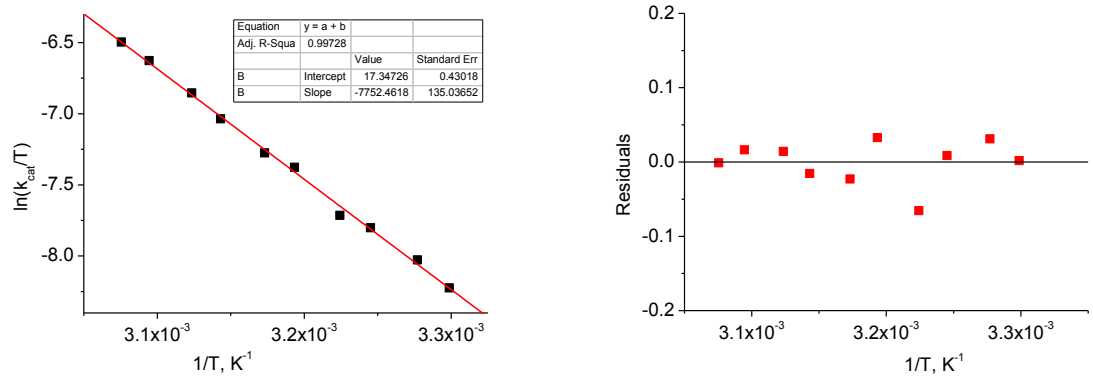

Figure 93. Eyring plot and residual analysis for kcat versus temperature data for the HPNP cleavage by MPGN-4 and Zn(II) without the 25°C point.

The only difference was found in the case of the AuNp1 nanoparticles, where addition of new data and removal of the 25° point did not decrease the errors of the calculated parameters. Residual analysis moreover indicates relatively large residues for most of the points. As a consequence we decided to report data and errors obtained in the 30-52° range for homogeneity with the other nanoparticles.

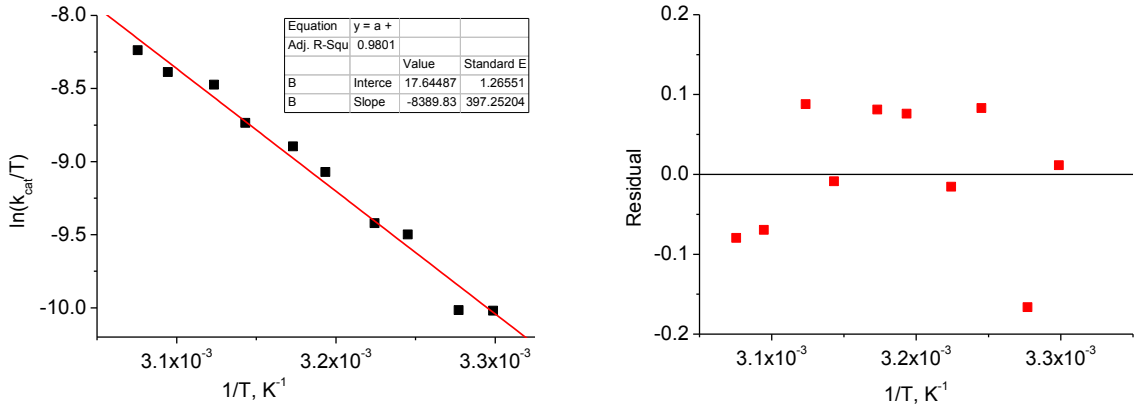

Figure 94. Eyring plot and residual analysis for kcat versus temperature data for the HPNP cleavage by MPGN-1 and Zn(II) without the 25°C point.

At the end of the analysis, the values reported in Table 7 were obtained and were submitted to the Welch's test of significance (which applies to samples of different size and variance) using the (propagated) standard errors obtained from the fittings as variance values. The test yields a probability higher than 99.9% that ΔH values for MPGN-2 and MPGN-4 are different from ΔH values for MPGN-3 and even MPGN-1. On the other hand, when the same score is set in the test for the ΔS values, no significant difference is found between the values.

Chapter 4

MIXED-MONOLAYER NANOZYMES

4.1 Overview

The monolayer protecting gold nanoparticles can be made by several different molecules. Such mixed monolayer are easily formed by using mixture of thiols during the systhesis or by exchanging part of the nanoparticle coating thiol with different ones. The possibility to form mix monolayer on the nanoparticle surface opens great opportunities to create smart nanosystems with different functionalities. Indeed, different functional groups inserted in the coating monolayer could perform different tasks or cooperate to improve the nanoparticles efficiency in a specific task. Moreover, increasing literature evidences indicate that the coating molecules can self-organize to form patterns like patches or stripes[67]. The driving forces for such self-organization are still unclear[68,69] and depend probably by the individual chemical properties of the molecules used.

In the case of nanozymes, as those reported in the previous chapter, the possibility to organize the active molecules in defined surface structures, as small patches or janus distributions, could be quite important. Indeed, while the cleavage of HPNP occurs without problems because of the relatively low affinity of this substrate for the particles, the cleavage of substrates endowed with larger hydrophobic moieties, as BNP, or greater negative charge, as RNA or DNA oligonucleotides, is often affected by relevant nanoparticles aggregation or precipitation problems. When the nanoparticles surface is saturated with the substrate, its charge is neutralized and the surface properties are changed in such a way that the nanoparticles are no more soluble in the reaction buffer.

Dilution of the positively charged active Zn(II)-TACN units with a neutral hydrophilic molecule could help preventing such problems, but could also decrease the systems reactivity. However, in the case of random mixing of the thiols, the nanoparticles would maintain its nature of polycation and interact with high affinity with polyanions. Moreover, the formation of bimetallic site would become less favorable because of the larger distance between the TACN units. On the other hand, in case of formation of patches, the catalytic activity should be maintained due to the local crowding of the TACN units, while binding of the substrates would scarcely affect the overall surface properties of the particles.

This considerations moved us to study how the distribution of the Zn(II)-binding thiol will affect the catalysis of these nanozymes in the cleavage reaction of HPNP.

Recently, L.J. Prins and coworkers[62] have studied the reactivity of nanoparticles coated by mixed monolayers made with the previously described Zn(II)-binding thiol, TACN-C4alkyl (thiol **1**), and the neutral thiol TEG (Figure 95). They could elegantly demonstrate that different distribution of the molecules on the monolayer should lead to different reactivity in particular when the catalytic thiol **1** is present in low amounts on the particles surface. In their study, no evidence of clustering was observed and the reactivity behavior was better explained by a random distribution.

In the present chapter, we report the synthesis of nanozymes coated with mixed monolayers made of thiol **1**, and either the zwitterionic thiol (ZW), which bears a phosphorylcholine moiety, or the triethilenglycol-thiol (TEG). Their only function of the latter is to improve water solubility to the nanozymes.

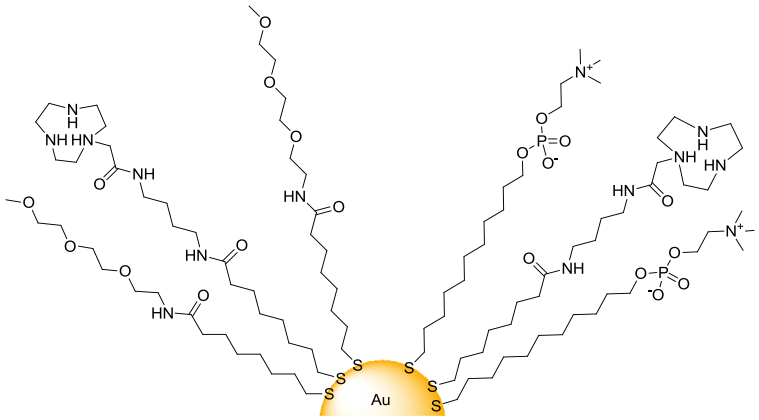

Figure 95. Representation of TEG and ZW coating TACN-C4alkyl nanoparticles.

The choice of the coating thiols was not by chance. They were carefully selected to take advantage of their structure to have the possibility to form different patterns on the particle surface.

In a recent paper published by our group[70], a NMR method based on the use of Gadolinium(III) ions was developed to investigate the distribution of thiols on the nanoparticles surface. Basically, the random and janus distributions can be distinguished by observing which signals are cancelled by the nanoparticles NMR spectra upon the surface binding of Gd(III) ions. The lanthanide ion strongly enhances the relaxation of spins located within a certain distance, and such relaxation results in a strong signal broadening up to disappearance. If the thiols are clustered and only one of the two binds the metal, exclusive or prevalent broadening of its signal will be observed. Otherwise, completed broadening of all the signals will be the outcome of a random distribution.

In that study, we could demonstrate that nanoparticles coated by TEG and octyl-thiol have a janus distribution, while particles coated by ZW and dodecyl-thiol have a random distribution. In following and still unpublished experiments, also nanoparticles coated by TEG and ZW thiols showed a janus distribution.

A tentative interpretation of such results is that thiols which can form an effective intermolecular interaction, as the H-bonds between the amides of the TEG thiol, cluster, while the molecules which form less effective interactions, as the dispersion and dipolar interaction available to ZW and alkyl-thiols, do not cluster. If this is true, a mixed monolayer made by thiols TACN-C4 and TEG would not cluster, as observed by Prins, simply because the H-bond interaction is available to both the molecules. On the other hand a mixed monolayer made by thiols TACN-C4 and ZW should cluster because the H-bonding interaction is available only to TACN-C4.

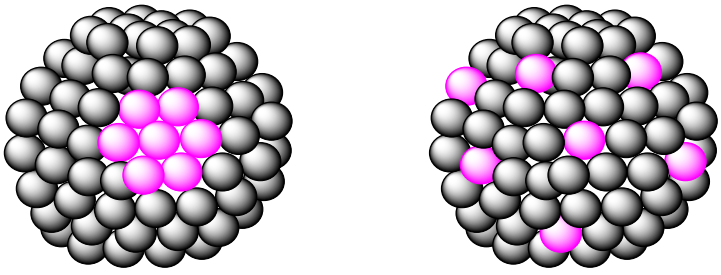

Figure 96. Representation of a clustered (right) and random (left) distribution.

4.2 Gold nanoparticles synthesis and characterization

To investigate the hypothesis discussed in the previous paragraph, we synthetized some nanozyme samples featuring with different proportions of coating molecules. The 2-steps procedure previously reported by us[48] was used:

- $MPGN_5$: AuNPs 15% TACN-C4/85% ZW
- $MPGN_6$:AuNPs 35% TACN-C4/65% ZW
- $MPGN_7$:AuNPs 30% TACN-C4/70% TEG
- $MPGN_8$:AuNPs 100% TACN-C4

All nanoparticles batches have been characterized by: 1) TEM (Figures 97, 102, 107 and 112). TEM imagines were analyzed with the software Pebbles; 2) TGA (Figures 98, 103, 108 and 113) and 3) NMR spectroscopy. NMR spectroscopy is used in three different modalities: standard monodimensional 1H-NMR (Figures 99, 104, 109 and 114), monodimensional diffusion-filtered (Figures 100, 105, 110, 115) (the comparison between these two spectra allows for the detection of impurities) and monodimensional 1H-NMR after I_2 addition (Figures 101, 106 and 111). I_2 caused the detaching of the thiols and allows the precise determination of the ratio between the thiols.

Table 11. Monolayer composition of MPGN5-8 determined by 1H-NMR.

MPGN	x_1			
	NMR	**NMR diff. filter**	**NMR after I_2**	**av[a]**
5	13.4	10.9	16.4	15
6	35.9	29.8	33.2	35
7	34.5	22.8	32.1	30
8	-	-	-	100

a) Average number was round to the closes 5-units interval.

$MPGN_5$ (AuNPs 15% TACN-C4/85% ZW)

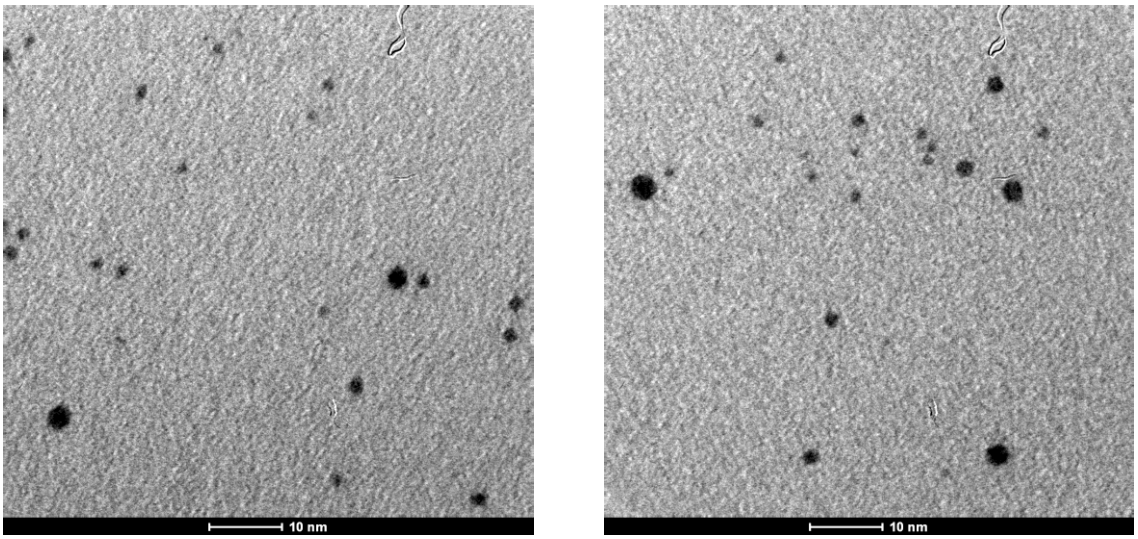

Figure 97. Sample TEM image of $MPGN_5$. Size distribution: average diameter = 2.5 (σ = 0.7 nm).

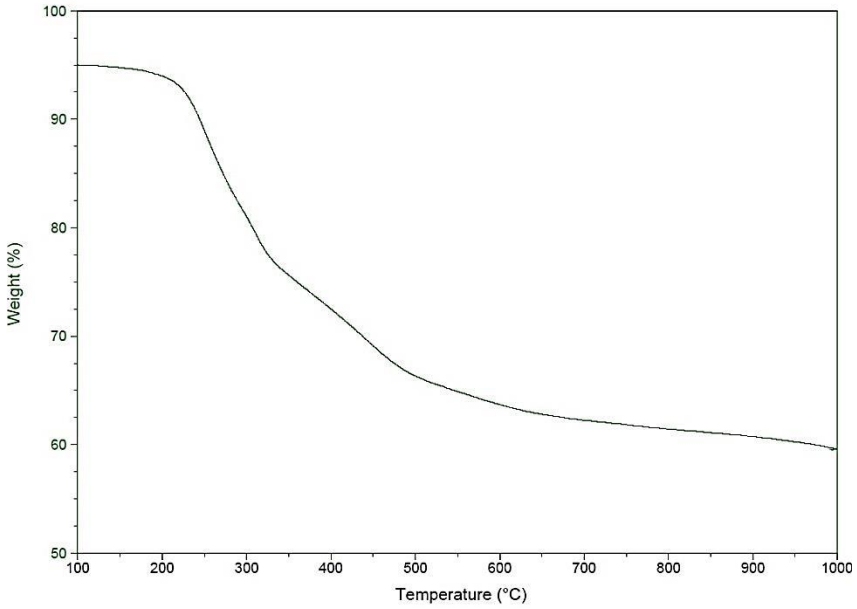

Figure 98. TGA analysis of $MPGN_5$ under air atmosphere.

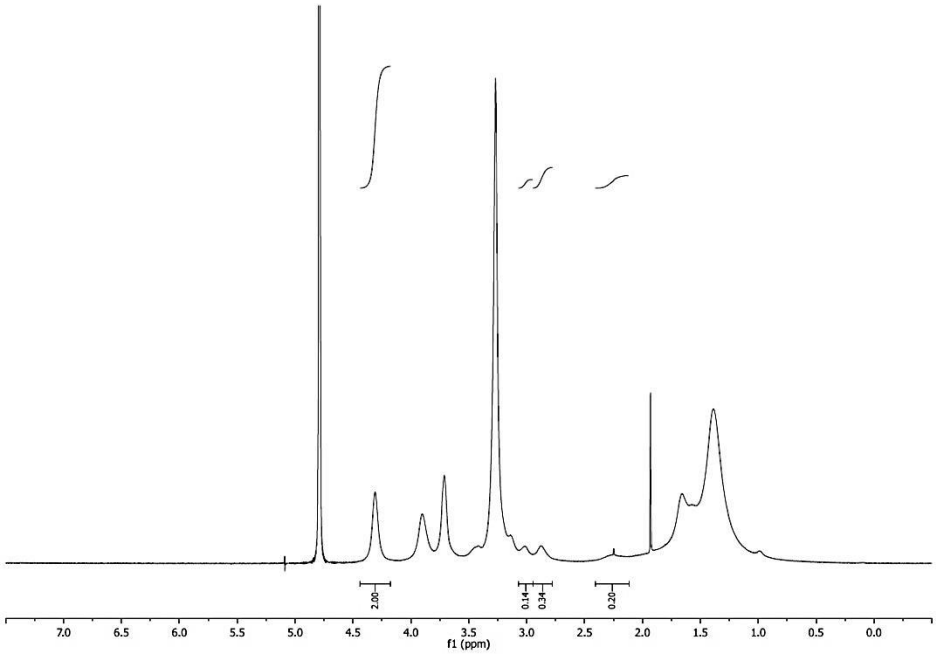

Figure 99. 1H-NMR (300 MHz) spectrum of the $MPGN_5$ in D_2O.

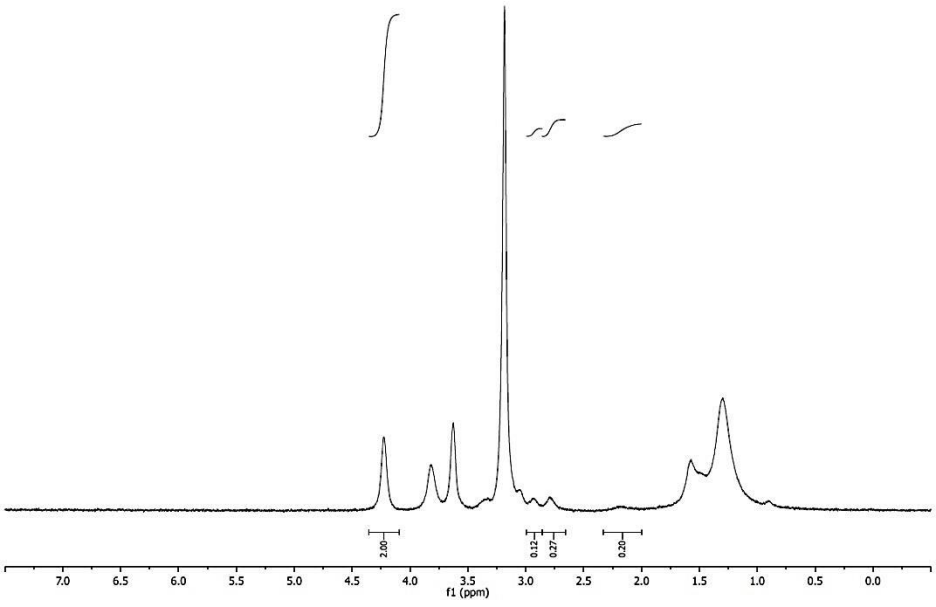

Figure 100. Diffussion-filtered 1H-NMR (300 MHz) spectrum of the $MPGN_5$ in D_2O.

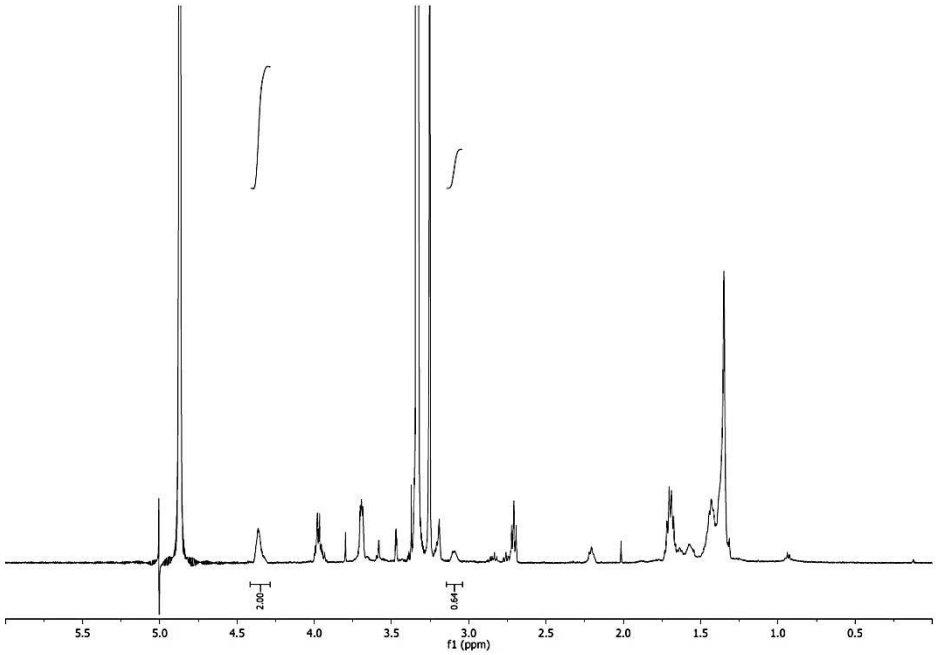

Figure 101. 1H-NMR (300 MHz) spectrum after I_2 treatment of the $MPGN_5$ in MeOD.

$MPGN_6$ (AuNPs 35% TACN-C4/65% ZW)

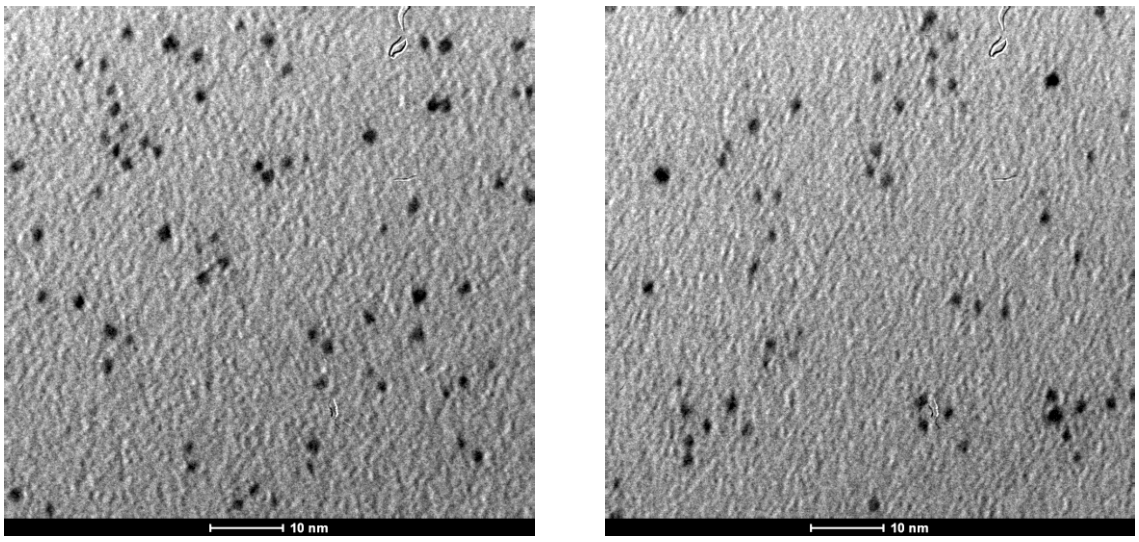

Figure 102. Sample TEM image of $MPGN_6$. Size distribution: average diameter = 2.0 (σ = 0.3 nm).

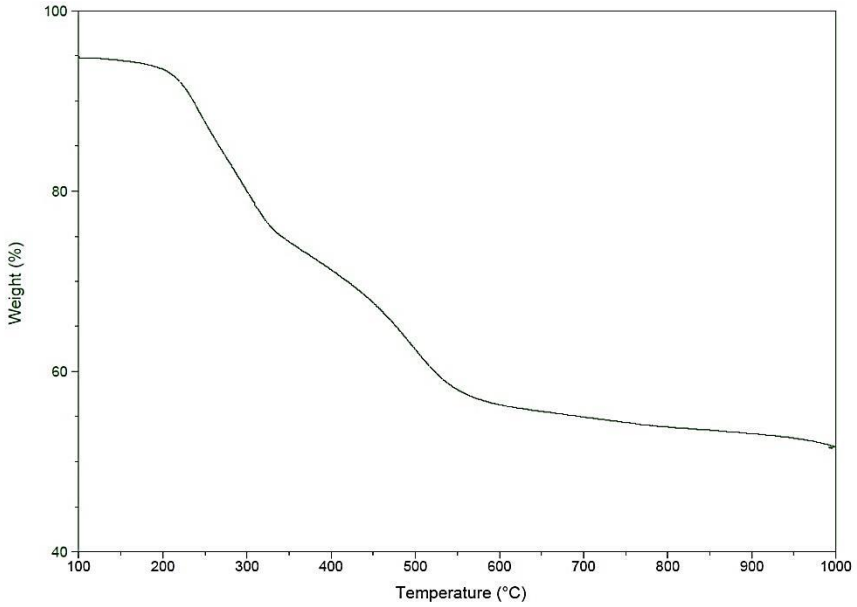

Figure 103. TGA analysis of $MPGN_6$ under air atmosphere.

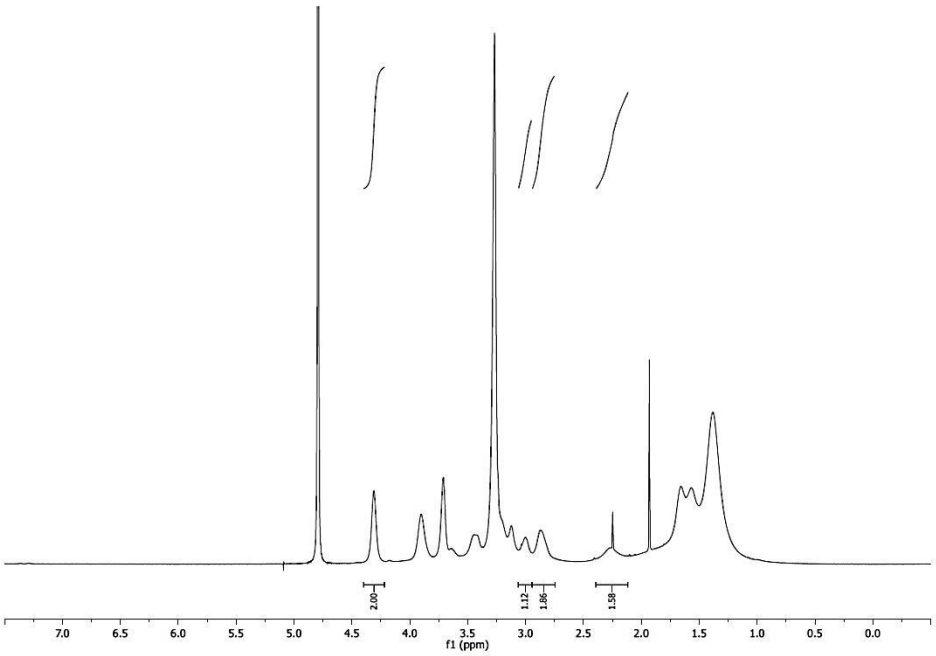

Figure 104. 1H-NMR (300 MHz) spectrum of the $MPGN_6$ in D_2O.

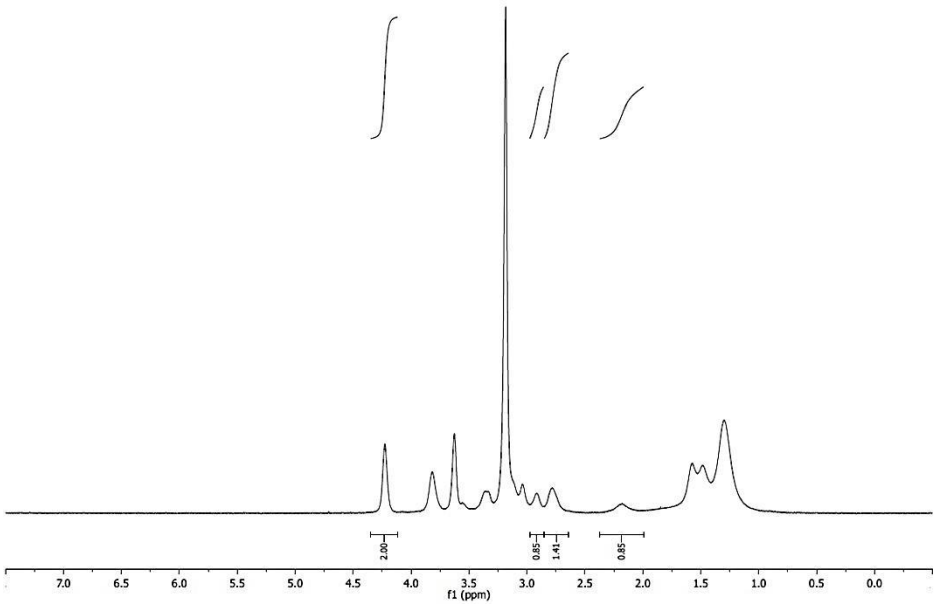

Figure 105. Diffussion-filtered 1H-NMR (300 MHz) spectrum of $MPGN_{\mathbf{6}}$ in D_2O.

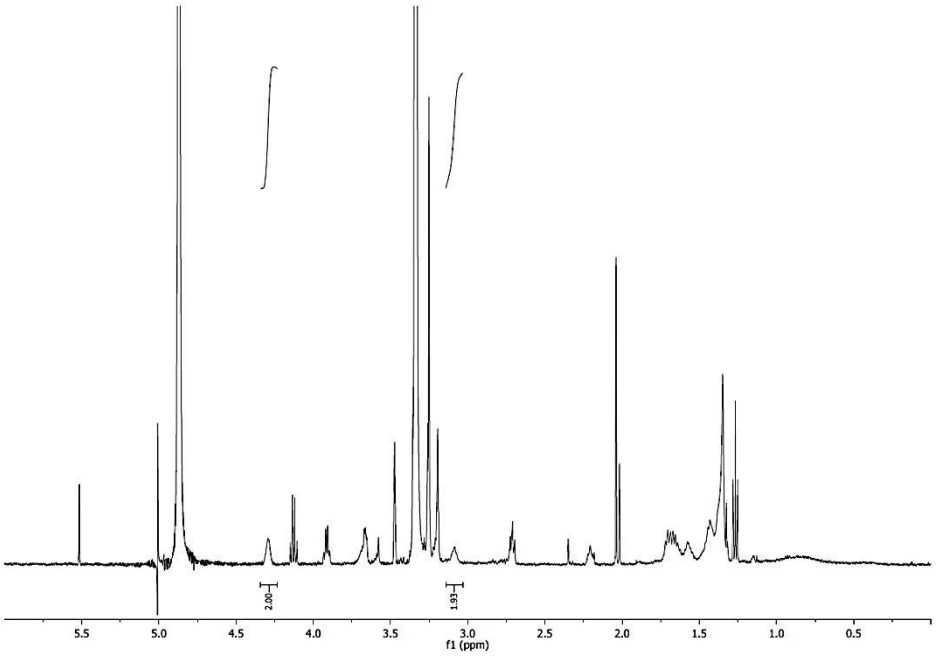

Figure 106. 1H-NMR (300 MHz) spectrum after I_2 treatment of the $MPGN_{\mathbf{6}}$ in MeOD.

$MPGN_7$ (AuNPs 30% TACN-C4/70% TEG)

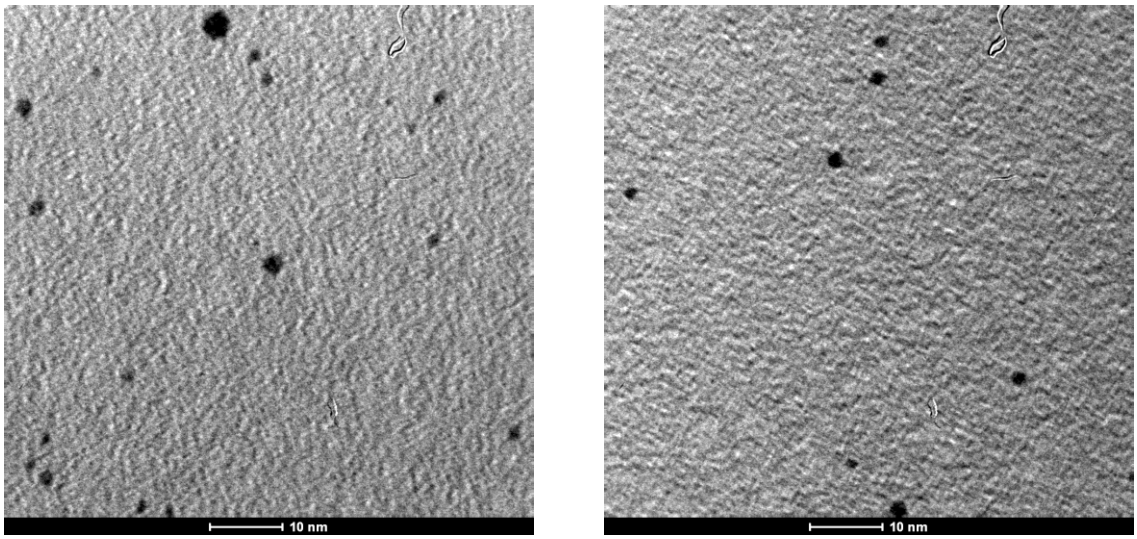

Figure 107. Sample TEM image of $MPGN_7$. Size distribution: average diameter = 2.4 (σ = 0.7 nm).

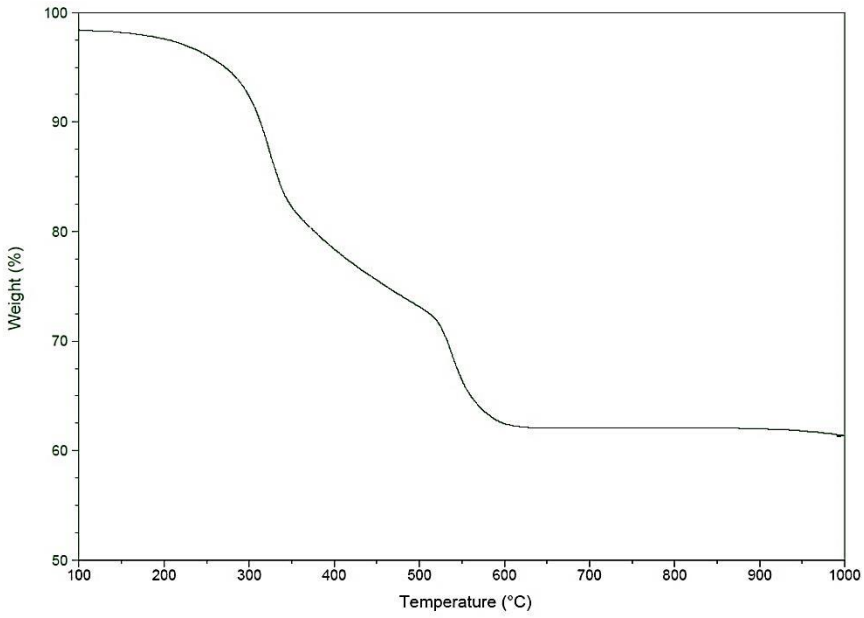

Figure 108. TGA analysis of $MPGN_7$ under air atmosphere.

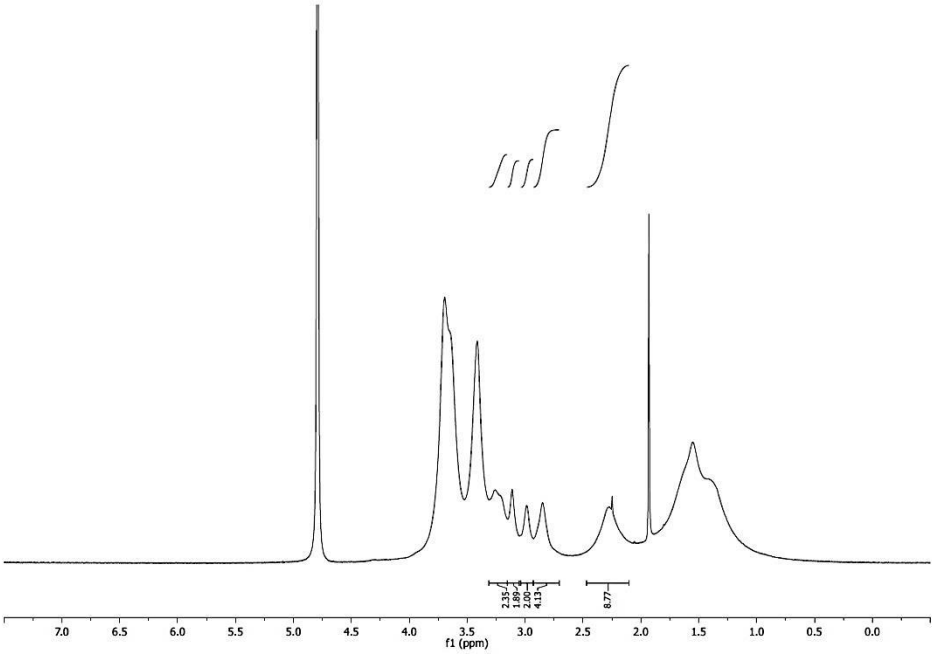

Figure 109. 1H-NMR (300MHz) spectrum of the $MPGN_7$ in D_2O.

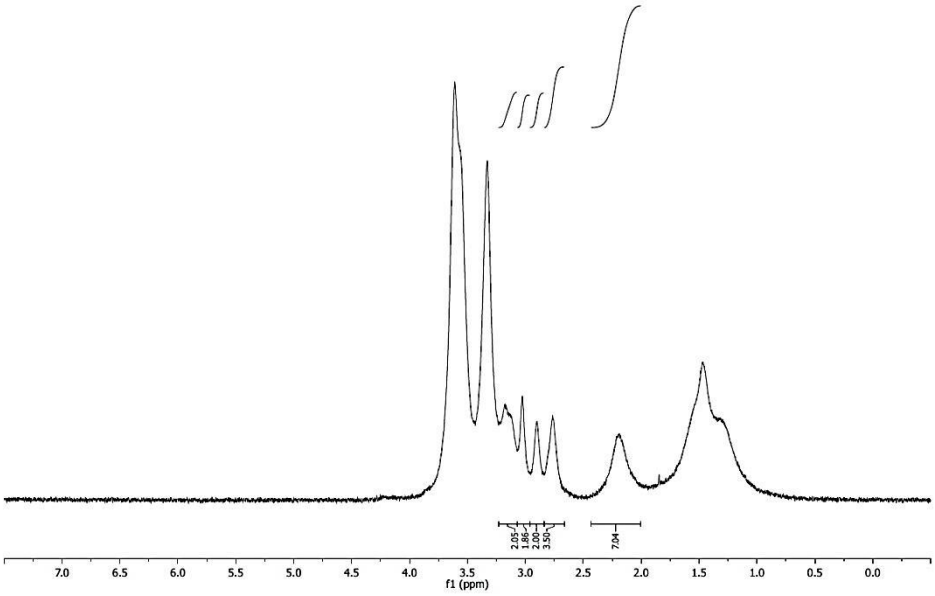

Figure 110. Diffussion-filtered 1H-NMR (300 MHz) spectrum of the $MPGN_7$ in D_2O.

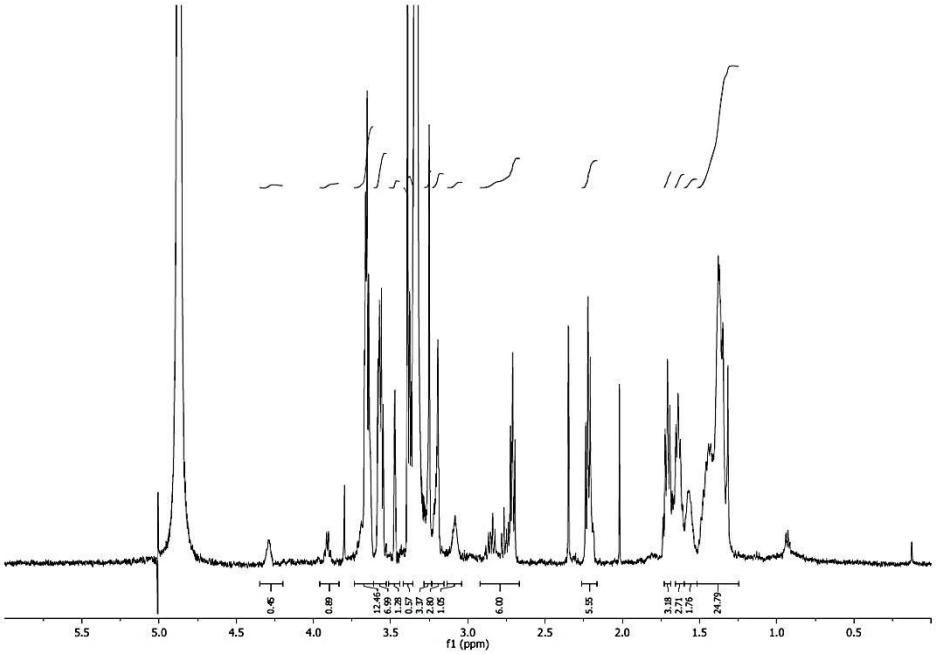

Figure 111. 1H-NMR (300 MHz) spectrum after I_2 treatment of the $MPGN_7$ in MeOD.

$MPGN_8$ (AuNPs 100% TACN-C4)

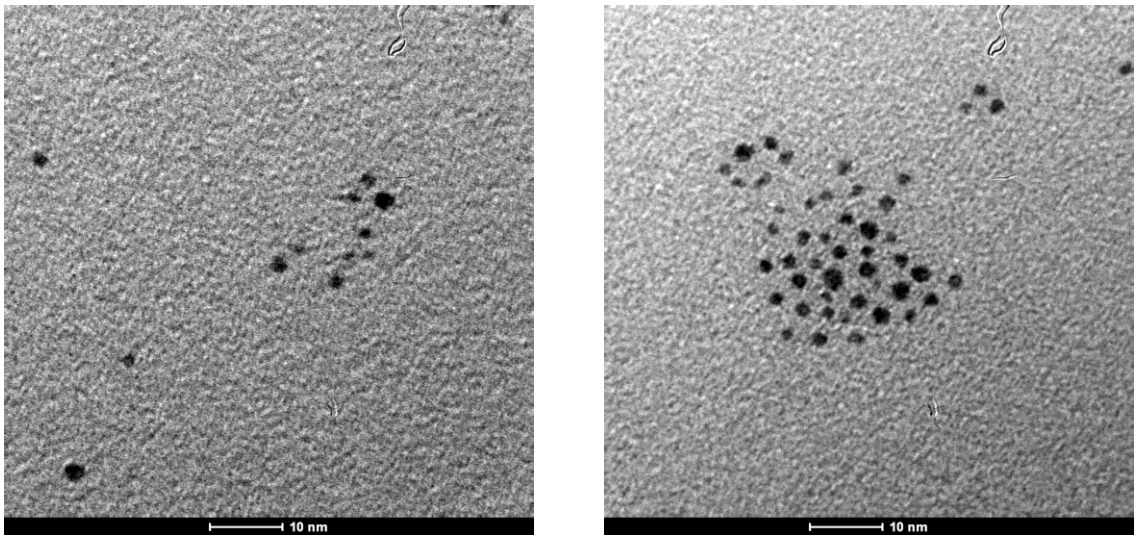

Figure 112. Sample TEM image of $MPGN_8$. Size distribution: average diameter = 2.2 (σ = 0.4 nm).

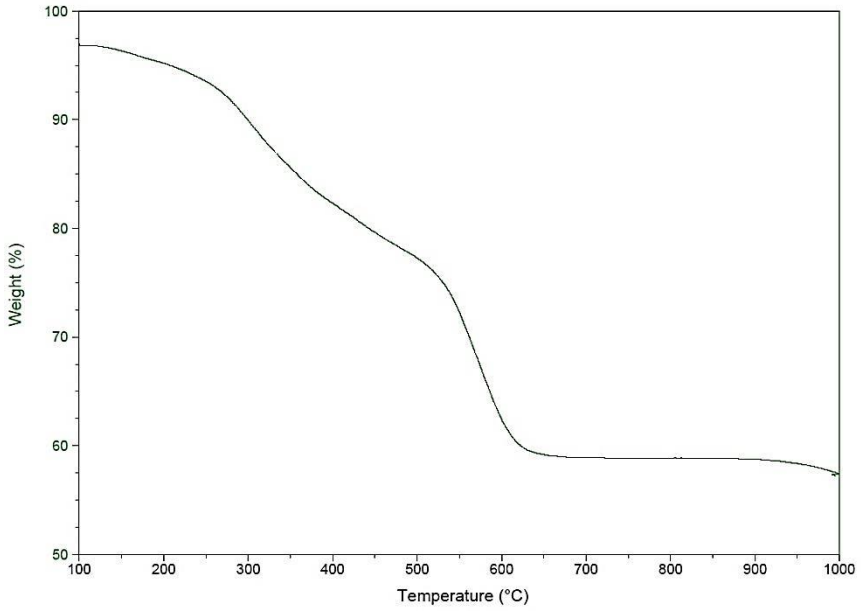

Figure 113. TGA analysis of $MPGN_8$ under air atmosphere.

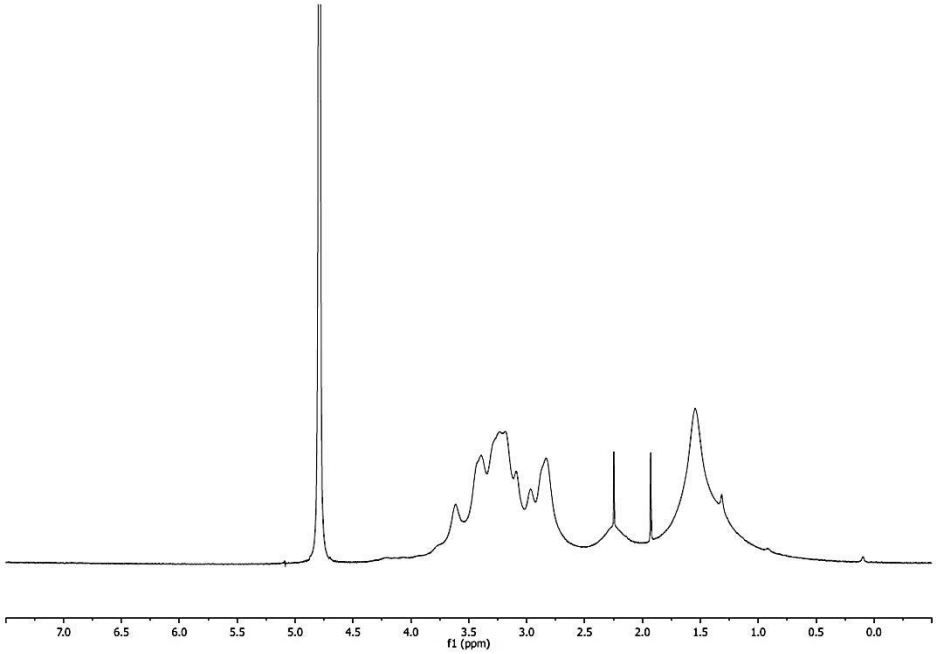

Figure 114. 1H-NMR (300 MHz) spectrum of the $MPGN_8$ in D_2O.

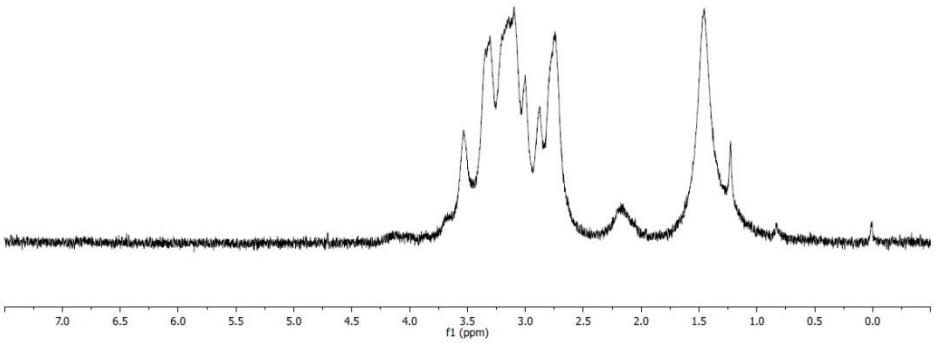

Figure 115. Diffussion-filtered 1H-NMR (300 MHz) spectrum of the $MPGN_{\mathbf{8}}$ in D_2O.

4.3 Kinetics studies

The reactivity of the systems $MPGN_{5-8}$ was studied using the cyclization of HPNP as test reaction. As already explained in the previous chapter, the first experiments are devoted to confirm the calculated concentration of TACN units in $MPGN_{5-8}$ stock solutions. This objective was achieved by performing Zn(II) dependent kinetic experiments. As already shown, sigmoidal profiles are obtained confirming the cooperative action of at least two metal ions.

Subsequently, we performed Michaelis-Menten kinetic experiments on HPNP cleavage. The reactions were followed in same condition used by Prins to allow comparison: 40 ºC in aqueous solution, buffered at pH 7,5 with HEPES 0,01 M. Reaction mixtures were prepared by mixing a solution of nanoparticles, a solution of $Zn(NO_3)_2$ and the buffer. The reactions were started by injection of a solution of HPNP in water.

The cleavage of the phosphodiester was monitored by measuring the absorbance of *p*-nitrophenolate at 400 nm. Initial rates were calculated by a linear fitting of the initial part (5% substrate cleavage) of the product concentration versus time profiles.

The experimental rate data were fitted according to the Michaelis-Menten equation (23):

$$v = \frac{k_{max}[HPNP]}{\frac{1}{K_{HPNP}} + [HPNP]} \qquad (23)$$

where v is the reaction initial rate, k_{max} is the limiting reaction rate in the experimental conditions and and K_{HPNP} is the apparent binding constant of the substrate to the catalyst.k_{cat} values were obtained by dividing k_{max} by $[Zn^{II}]/2$(half to the total Zn(II) concentration is used to account by the fact the reaction occurs in bimetallic sites).

The Michalis-Menten profiles obtained are shown in figure 116. The first conclusion that maybe drawn is that by increasing the loading of catalytic species, i.e. TACN-Zn(II) complexes, on the nanoparticles surface the nanozymes activity is enhanced. Moreover, the nanozymes with ZW thiols ($MPGN_5$ and $MPGN_6$) reach faster than the other the maximum reaction rate, as suggested by the higher slope of the Michaelis-Menten profile at low

substrate concentration. This is confirmed by the values of K_M reported in table 12, which are lower than the values of K_M obtained for MPGN**8** and MPGN**7**

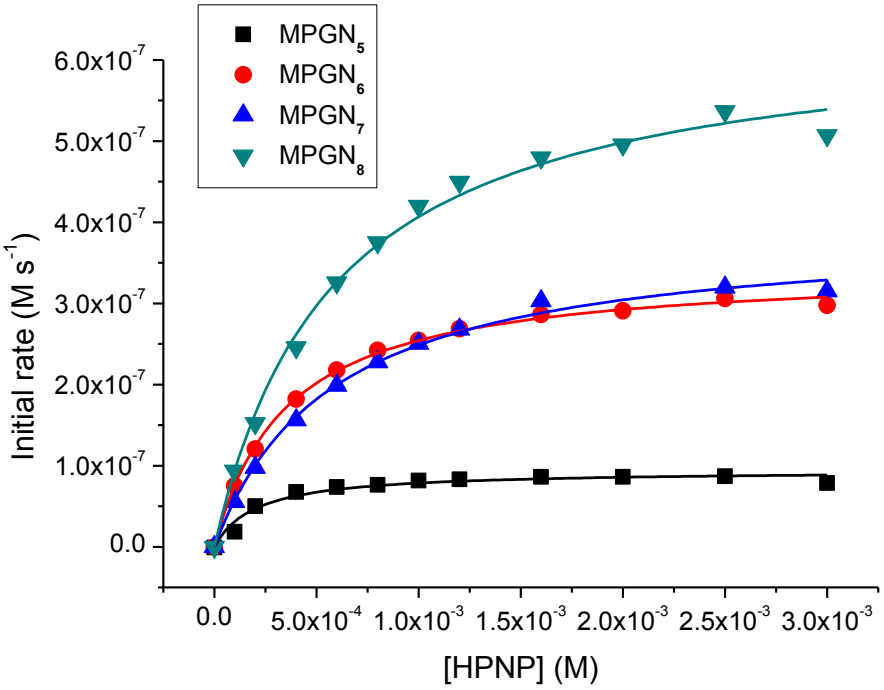

Figure 116. Rate of HPNP cleavage promoted MPGN**5-8** and Zn(II) as a function of the concentration of HPNP: Conditions: [NP, in thiol units] = 2.0 × 10^{-5} M, [Zn(II)] = 2.0 × 10^{-5} M, [buffer] = 1.0 × 10^{-2} M, pH = 7.5, 40 °C.

In the case of MPGN **6** and **7** although the different nature of the Zn(II)-binding thiols, the reactivity is quite similar as shown in table 12 (values of k_{cat}). However, MPGN**6** need less amount of substrate to reach the maximum reactivity than MPGN**7**, as supported by the lower value of K_M in MPGN**6** than in MPGN**7**. The source of this difference in the nanozymes affinity for the substrate will be explained later on.

The Michaelis-Menten parameters obtained for $MPGN_{5-8}$ are reported in table 12.

Table 12. Michaelis-Menten parameters for HPNP cleavage in the presence $MPGN_{5-8}$ and Zn(II) in water at pH 7.5 and 40 °C. Errors are within ±5%.

MPGN	k_{cat}[a] ($\times 10^{-3}$ s^{-1})	K_M[a] (mM)	k_2[b] (M^{-1} s^{-1})	k_{rel}[c]
5	9.81 ± 0.36	0.23 ± 0.04	43 ± 7	$4.91 \pm 0.18 \times 10^4$
6	34.4 ± 0.4	0.35 ± 0.02	98 ± 4	$1.72 \pm 0.02 \times 10^5$
7	39.2 ± 0.9	0.58 ± 0.04	68 ± 5	$1.96 \pm 0.05 \times 10^5$
8	64.4 ± 1.8	0.58 ± 0.05	110 ± 10	$3.22 \pm 0.09 \times 10^5$

a) Normalized for the theoretical concentration of bimetallic sites, i.e. [Zn(II)]/2. b) $k_2 = k_{cat}/K_M$. c) $k^{rel} = k_{cat}/k_{uncat}$, $k_{uncat} = 2 \times 10^{-7}$ s^{-1}, ref [62]. (Conditions: [NP, in thiol units] = 2.0×10^{-5} M, [Zn(II)] = 2.0×10^{-5} M, [buffer] = 1.0×10^{-2} M).

4.4 Discussion

In principle, the data previously shown could appear not enough to characterized such a complex system. However, as alredy mentioned, the TACN-C4/TEG systems have been previously investigated by Prins and his data can be used as a reference. Figure 117 reports both the values of k_{cat} and K_M obtained by Prins for the TACN-C4/TEG system (red), by me for the TACN-C4/ZW system (black) and, as a reference, for the TACN-C4 system (at the 30% of TACN-C4 loading). Inspection of the two plots reveals the following features: 1) the reactivity of $MPGN_{5-8}$ is similar to the Prins data, with some very relevant difference. At first, the reactivity of the 30% TACN-C4/TEG particles is perfectly in line from that expected on the basis of Prins data. Second behaviour is very similar in both systems characterized by different coating thiols (TEG and ZW). Third, behaviour is remarkably different between the two systems with the nanoparticles with ZW displaying much higher substrate binding at low TACN loadings.

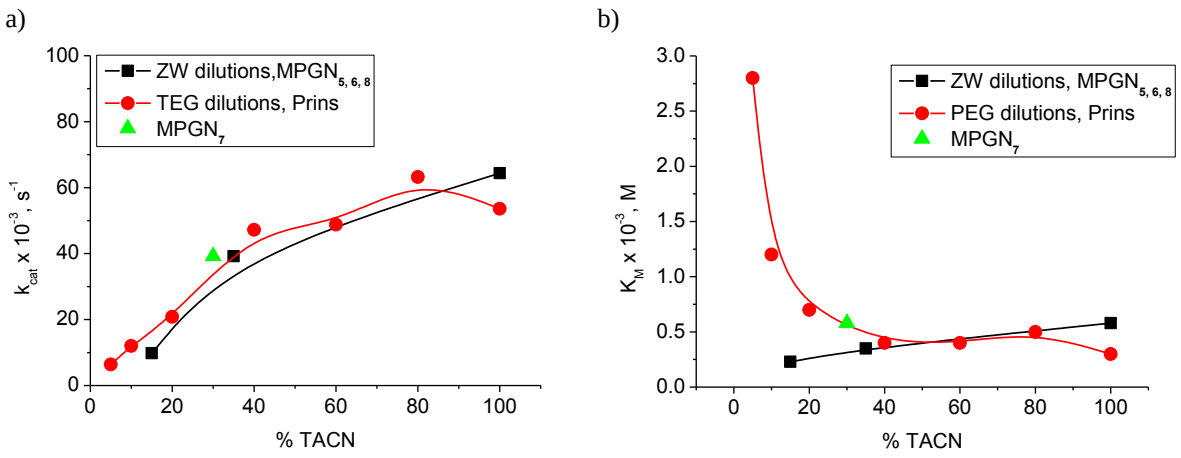

Figure 117. a) $\boldsymbol{k_{cat}}$ and b) $\boldsymbol{K_M}$ as a function of the TACN dilution on the nanoparticles surface. Data in red, reported in*. Conditions: [NP, in thiol units] = 2.0 × 10^{-5} M, [Zn(II)] = 2.0 × 10^{-5} M, [buffer] = 1.0 × 10^{-2} M, at pH 7.5 and 40°C.

Such behavior could be explained by supposing a clustered distribution of the TACN thiols in these nanoparticles. Figure 117 is a partial representation of a gold nanoparticle surface with the molecules represented by hexagons. In this simulation every single molecule can be surrounded by six molecules. The aim of these illustration is to represent the possible situation of Zn(II)-binding thiols (in yellow) in a clustered or a random distribution. Since two TACN-Zn(II) complexes are needed to bind one molecule of substrate, the possibilities to find binding sites increase in a clustered distribution rather than in a random one, although the number of TACN-Zn(II) complexes are the same.

Higher number of binding sites means higher affinity of the nanozymes for the substrate which is translate to lower values of K_M (see figure 118b). Hence, K_M is expected to remain constant, independently from nanoparticles composition. The maximum difference between a clustered and a random system is expected at low TACN units. In this case, indeed, the K_M should dramatically increase for a random distribution, where the possibility to find a bimetallic site is very low, but not for a cluster distribution, where the number of potential binding sites is still quite relevant.

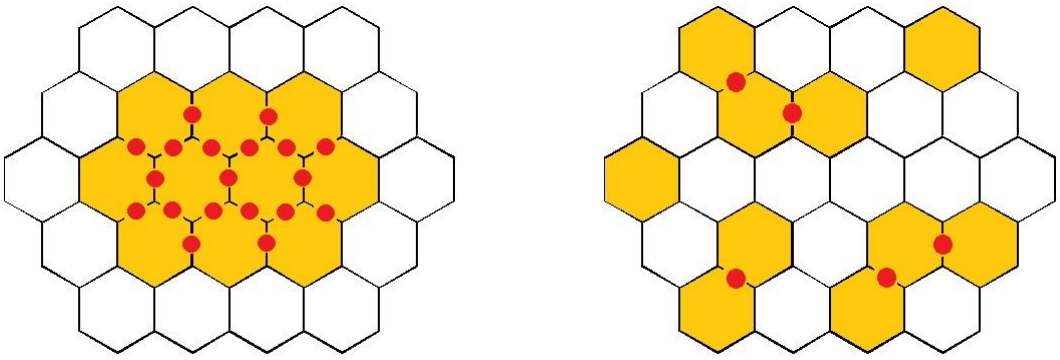

Figure 118. Representation of the possible binding sites (in red) in a clustered (left) or ramdon distribution(right).

Remarkably, the distribution of the catalytic units in the nanoparticles surface affects the affinity of the system for the substrate but not its activity. Indeed, for the same loading of TACN in different distribution we obtain similar values of k_{cat}. This may be explained by considering that k_{cat} is a measure of the reactivity when the complex substrate-catalyst is formed.

The results here reported apparently suggest that the use of ZW thiols as coating molecules is preferred than the use of TEG ones, since only with the first thiol clustered distributions were obtained.

Bibliography

1. Westheimer FH. Nature Chose Phosphates The Role of Phosphates The Importance of Being Ionized. (1).

2. Nature THE, Of A, Obtained R, The F, Mechanics Q. Bond of. 1931;455(1927).

3. Gamoke B, Neff D, Simons J. Nature of PO bonds in phosphates. *J Phys Chem A*. 2009;113(19):5677–84. doi:10.1021/jp810014s.

4. Schroeder GK, Lad C, Wyman P, Williams NH, Wolfenden R. The time required for water attack at the phosphorus atom of simple phosphodiesters and of DNA. *Proc Natl Acad Sci U S A*. 2006;103(11):4052–5. doi:10.1073/pnas.0510879103.

5. Jrirvinen P, Oivanen M, Liinnberg H. Monophosphates : Kinetics and Mechanisms. 1991;5401(5):5396–5401.

6. Perreault DM, Anslyn E V. REVIWS Unifying the Current Data on the Mechanism of Cleavage - Transesterification of RNA.

7. Korhonen H, Koivusalo T, Toivola S, Mikkola S. There is no universal mechanism for the cleavage of RNA model compounds in the presence of metal ion catalysts. *Org Biomol Chem*. 2013;11(48):8324–39. doi:10.1039/c3ob41554f.

8. Korhonen H, Mikkola S, Williams NH. The mechanism of cleavage and isomerisation of RNA promoted by an efficient dinuclear Zn2+ complex. *Chemistry*. 2012;18(2):659–70. doi:10.1002/chem.201100721.

9. Wilcox DE. Binuclear Metallohydrolases. *Chem Rev*. 1996;96(7):2435–2458. Available at: http://www.ncbi.nlm.nih.gov/pubmed/11848832.

10. Strater N, Lipscomb WN, Klabunde T, Krebs B. Two-Metal Ion Catalysis in Enzymatic Acyl- and Phosphoryl-Transfer Reactions.

11. Williams NH, Takasaki B, Wall M, Chin J. Structure and Nuclease Activity of Simple Dinuclear Metal Complexes: Quantitative Dissection of the Role of Metal Ions. *Acc Chem Res*. 1999;32(6):485–493. doi:10.1021/ar9500877.

12. Hegg EL, Burstyn JN. Toward the development of metal-based synthetic nucleases and peptidases: a rationale and progress report in applying the principles of coordination chemistry. *Coord Chem Rev*. 1998;173(1):133–165. doi:10.1016/S0010-8545(98)00157-X.

13. Williams NH, Cheung W, Chin J, V SU, Sheffield S. Reactivity of Phosphate Diesters Doubly Coordinated to a Dinuclear Cobalt (III) Complex : Dependence of the Reactivity on the Basicity of the Leaving Group. 1998;7863(Iii):8079–8087.

14. Lönnberg H. Cleavage of RNA phosphodiester bonds by small molecular entities: a mechanistic insight. *Org Biomol Chem*. 2011;9(6):1687–703. doi:10.1039/c0ob00486c.

15. Mancin F, Tecilla P. Zinc(ii) complexes as hydrolytic catalysts of phosphate diester cleavage: from model substrates to nucleic acids. *New J Chem*. 2007;31(6):800. doi:10.1039/b703556j.

16. Mancin F, Scrimin P, Tecilla P. Progress in artificial metallonucleases. *Chem Commun (Camb)*. 2012;48(45):5545–59. doi:10.1039/c2cc30952a.

17. Morrow JR, Iranzo O. Synthetic metallonucleases for RNA cleavage. *Curr Opin Chem Biol*. 2004;8(2):192–200. doi:10.1016/j.cbpa.2004.02.006.

18. Mathews RA, Rossiter CS, Morrow JR, Richard JP. A minimalist approach to understanding the efficiency of mononuclear Zn (II) complexes as catalysts of cleavage of an RNA analog †. 2007:3804–3811. doi:10.1039/b707409c.

19. Aôt-haddou H, Sumaoka J, Wiskur SL, Folmer-andersen JF, Anslyn E V. as Nachahmen der Kooperativit‰t zwischen Metallzentren und Aminos‰ureresten in Enzymen kann zu hoch aktiven, multifunktionellen Katalysato- ren f¸hren. 2002;(21):4185–4188.

20. Feng G, Mareque-Rivas JC, Williams NH. Comparing a mononuclear Zn(II) complex with hydrogen bond donors with a dinuclear Zn(II) complex for catalysing phosphate ester cleavage. *Chem Commun (Camb)*. 2006;2(17):1845–7. doi:10.1039/b514328d.

21. Iranzo O, Kovalevsky AY, Morrow JR, Richard JP. Physical and kinetic analysis of the cooperative role of metal ions in catalysis of phosphodiester cleavage by a dinuclear Zn(II) complex. *J Am Chem Soc*. 2003;125(7):1988–93. doi:10.1021/ja027728v.

22. Feng G, Natale D, Prabaharan R, Mareque-Rivas JC, Williams NH. Efficient phosphodiester binding and cleavage by a ZnII complex combining hydrogen-bonding interactions and double Lewis acid activation. *Angew Chem Int Ed Engl*. 2006;45(42):7056–9. doi:10.1002/anie.200602532.

23. Mohamed MF, Sánchez-Lombardo I, Neverov A a, Brown RS. Solvent induced cooperativity of Zn(II) complexes cleaving a phosphate diester RNA analog in methanol. *Org Biomol Chem*. 2012;10(3):631–9. doi:10.1039/c1ob06482g.

24. Neverov A a, Lu Z-L, Maxwell CI, et al. Combination of a dinuclear Zn2+ complex and a medium effect exerts a 10(12)-fold rate enhancement of cleavage of an RNA

and DNA model system. *J Am Chem Soc*. 2006;128(50):16398–405. doi:10.1021/ja0651714.

25. Liu CT, Neverov A a, Brown RS. Enzyme-like acceleration for the hydrolysis of a DNA model promoted by a dinuclear Zn(II) catalyst in dilute aqueous ethanol. *J Am Chem Soc*. 2008;130(42):13870–2. doi:10.1021/ja805801j.

26. Molenveld P, Engbersen JFJ, Reinhoudt DN. Specific RNA Dinucleotide Cleavage by a. 1999:3189–3192.

27. Wang Q, Lo H. Simultaneous Interaction with Base and Phosphate Moieties Modulates the Phosphodiester Cleavage of Dinucleoside 3 ′ , 5 ′ -Monophosphates by Dinuclear Zn 2 + Complexes of Di (azacrown) Ligands. 2006;(7):10716–10728.

28. Sissi C, Rossi P, Felluga F, et al. Dinuclear Zn(2+) complexes of synthetic heptapeptides as artificial nucleases. *J Am Chem Soc*. 2001;123(13):3169–70. Available at: http://www.ncbi.nlm.nih.gov/pubmed/11457042.

29. Yamada K, Takahashi Y, Yamamura H, Araki S, Kawai M, Saito K. Phosphodiester bond cleavage mediated by a cyclic β-sheet peptide-based dinuclear zinc(ii) complex. *Chem Commun*. 2000;2(14):1315–1316. doi:10.1039/b003370g.

30. Manea F, Houillon FB, Pasquato L, Scrimin P. Nanozymes: gold-nanoparticle-based transphosphorylation catalysts. *Angew Chem Int Ed Engl*. 2004;43(45):6165–9. doi:10.1002/anie.200460649.

31. Murtola M, Wenska M, Strömberg R. PNAzymes that are artificial RNA restriction enzymes. *J Am Chem Soc*. 2010;132(26):8984–90. doi:10.1021/ja1008739.

32. Bonfá L, Gatos M, Mancin F, Tecilla P, Tonellato U. The ligand effect on the hydrolytic reactivity of Zn(II) complexes toward phosphate diesters. *Inorg Chem*. 2003;42(12):3943–9. doi:10.1021/ic034139x.

33. Livieri M, Mancin F, Tonellato U, Chin J. Multiple functional group cooperation in phosphate diester cleavage promoted by Zn(II) complexes. *Chem Commun (Camb)*. 2004;(24):2862–3. doi:10.1039/b412111b.

34. Tirel EY, Bellamy Z, Adams H, Duarte F, Williams NH. Catalytic Zinc Complexes for Phosphate Diester Hydrolysis. *Angew Chem Int Ed Engl*. 2014:1–6. doi:10.1002/anie.201400335.

35. Breslow R, Guo T. Diels-Alder Reactions in Nonaqueous Polar Solvents . Kinetic Effects of Chaotropic and Antichaotropic Agents and of P-C yclodext rin. 1988:5613–5617.

36. Leivers M, Breslow R. Concerning two-metal cooperativity in model phosphate hydrolysis. *Bioorg Chem*. 2001;29(6):345–56. doi:10.1006/bioo.2001.1221.

37. He C, Lippard SJ. Modeling Carboxylate-Bridged Dinuclear Active Sites in Metalloenzymes Using a Novel Naphthyridine-Based Dinucleating Ligand. 2000;(17):12165–12166.

38. Phosphate PPD, Bazzicalupi C, Bencini A, et al. Carboxy and Phosphate Esters Cleavage with Mono- and Dinuclear Zinc (II) Macrocyclic Complexes in Aqueous Solution . Crystal Structure of [Zn 2 L1 (μ -PP) 2 (MeOH) 2](ClO 4) 2 (L1. 1997;1(Ii):2784–2790.

39. Fitzsimons MP, Barton JK, Rh-p A. Design of a Synthetic Nuclease : DNA Hydrolysis by a Zinc-Binding Peptide Tethered to a Rhodium Intercalator Di V ision of Chemistry and Chemical Engineering California Institute of Technology substantial interest . 1 While many reagents have been success. 1997;7863(23):3379–3380.

40. Boseggia E, Gatos M, Lucatello L, et al. Toward Efficient Zn (II) -Based Artificial Nucleases to hydrolysis under uncatalyzed physiological conditions . At. 2004;(Ii):4543–4549.

41. Bonomi R, Selvestrel F, Lombardo V, et al. Phosphate diester and DNA hydrolysis by a multivalent, nanoparticle-based catalyst. *J Am Chem Soc*. 2008;130(47):15744–5. doi:10.1021/ja801794t.

42. Gruber B, Kataev E, Aschenbrenner J, Stadlbauer S, König B. Vesicles and micelles from amphiphilic zinc(II)-cyclen complexes as highly potent promoters of hydrolytic DNA cleavage. *J Am Chem Soc*. 2011;133(51):20704–7. doi:10.1021/ja209247w.

43. Yamamoto Y, Mori M, Aiba Y, et al. Chemical modification of Ce(IV)/EDTA-based artificial restriction DNA cutter for versatile manipulation of double-stranded DNA. *Nucleic Acids Res*. 2007;35(7):e53. doi:10.1093/nar/gkm052.

44. Lönnberg T, Aiba Y, Hamano Y, Miyajima Y, Sumaoka J, Komiyama M. Oxidation of an oligonucleotide-bound Ce(III)/multiphosphonate complex for site-selective DNA scission. *Chemistry*. 2010;16(3):855–9. doi:10.1002/chem.200902169.

45. Stevenson C, Hillier J, Hillier J. The formation of colloidal gold. 1969:670–673.

46. Brust M, Walker M, Bethell D, Schiffrin DJ, Whyman R. Synthesis of Thiol-derivatised Gold Nanoparticles in. 2000:801–802.

47. Jana NR, Peng X. Single-phase and gram-scale routes toward nearly monodisperse Au and other noble metal nanocrystals. *J Am Chem Soc*. 2003;125(47):14280–1. doi:10.1021/ja038219b.

48. Manea F, Bindoli C, Polizzi S, Lay L, Scrimin P. Expeditious synthesis of water-soluble, monolayer-protected gold nanoparticles of controlled size and monolayer composition. *Langmuir*. 2008;24(8):4120–4. doi:10.1021/la703558y.

49. Cobley CM, Xia Y. Gold and Nanotechnology. *Elements*. 2009;5(5):309–313. doi:10.2113/gselements.5.5.309.

50. Grzelczak M, Pérez-Juste J, Mulvaney P, Liz-Marzán LM. Shape control in gold nanoparticle synthesis. *Chem Soc Rev*. 2008;37(9):1783–91. doi:10.1039/b711490g.

51. Häkkinen H. The gold-sulfur interface at the nanoscale. *Nat Chem*. 2012;4(6):443–55. doi:10.1038/nchem.1352.

52. Han G, You C-C, Kim B, et al. Light-Regulated Release of DNA and Its Delivery to Nuclei by Means of Photolabile Gold Nanoparticles. *Angew Chemie*. 2006;118(19):3237–3241. doi:10.1002/ange.200600214.

53. Dubertret B, Calame M, Libchaber a J. Single-mismatch detection using gold-quenched fluorescent oligonucleotides. *Nat Biotechnol*. 2001;19(4):365–70. doi:10.1038/86762.

54. Achtung C, Iii RE, Immobilized C, Colloids G. Cooperative Catalysis in the Hydrolytic Kinetic Resolution of. 2008;(III):967–971. doi:10.1002/adsc.200800028.

55. Lönnberg T. Understanding catalysis of phosphate-transfer reactions by the large ribozymes. *Chemistry*. 2011;17(26):7140–53. doi:10.1002/chem.201100009.

56. Rossi P, Felluga F, Tecilla P, et al. A Bimetallic Helical Heptapeptide as a Transphosphorylation Catalyst in Water The realization of synthetic catalysts or molecular devices using properly assembled R -amino acid sequences to take advantage a more facile synthetic access to a wide variety o. 1999;6:6948–6949.

57. Fry FH, Jensen P, Kepert CM, Spiccia L. Macrocyclic copper(II) and zinc(II) complexes incorporating phosphate esters. *Inorg Chem*. 2003;42(18):5637–44. doi:10.1021/ic026091d.

58. Scaramuzzo F a, Licini G, Zonta C. Determination of amino acid enantiopurity and absolute configuration: synergism between configurationally labile metal-based receptors and dynamic covalent interactions. *Chemistry*. 2013;19(49):16809–13. doi:10.1002/chem.201302721.

59. Zaramella D, Scrimin P, Prins LJ. Self-assembly of a catalytic multivalent peptide-nanoparticle complex. *J Am Chem Soc*. 2012;134(20):8396–9. doi:10.1021/ja302754h.

60. Hostetler MJ, Wingate JE, Zhong C, et al. Alkanethiolate Gold Cluster Molecules with Core Diameters from 1 . 5 to 5 . 2 nm : Core and Monolayer Properties as a Function of Core Size. 2008;7463(c):17–30.

61. Nimmala PR, Yoon B, Whetten RL, Landman U, Dass A. Au(67)(SR)(35) nanomolecules: characteristic size-specific optical, electrochemical, structural

properties and first-principles theoretical analysis. *J Phys Chem A*. 2013;117(2):504–17. doi:10.1021/jp311491v.

62. Zaupa G, Mora C, Bonomi R, Prins LJ, Scrimin P. Catalytic self-assembled monolayers on Au nanoparticles: the source of catalysis of a transphosphorylation reaction. *Chemistry*. 2011;17(17):4879–89. doi:10.1002/chem.201002590.

63. Ferris DC, Drago RS. Rate of Decarboxylation of Benzisoxazole-3-Carboxylate Ions as a Probe of Solvation in Biological and Other Media. *J Am Chem Soc*. 1994;116(17):7509–7514. doi:10.1021/ja00096a006.

64. Brinchi L, Germani R, Savelli G, Marte L. Decarboxylation of 6-nitrobenzisoxazole-3-carboxylate in aqueous cationic micelles: kinetic evidence of microinterface property changes. *J Colloid Interface Sci*. 2003;262(1):290–3. doi:10.1016/S0021-9797(02)00086-3.

65. Zaupa G, Scrimin P, Prins LJ. Origin of the dendritic effect in multivalent enzyme-like catalysts. *J Am Chem Soc*. 2008;130(17):5699–709. doi:10.1021/ja7113213.

66. Avenier F, Hollfelder F. Combining medium effects and cofactor catalysis: metal-coordinated synzymes accelerate phosphate transfer by 10(8). *Chemistry*. 2009;15(45):12371–80. doi:10.1002/chem.200802616.

67. Jackson AM, Myerson JW, Stellacci F. Spontaneous assembly of subnanometre-ordered domains in the ligand shell of monolayer-protected nanoparticles. *Nat Mater*. 2004;3(5):330–6. doi:10.1038/nmat1116.

68. Gentilini C, Pasquato L. Morphology of mixed-monolayers protecting metal nanoparticles. *J Mater Chem*. 2010;20(8):1403. doi:10.1039/b912759c.

69. Shaw CP, Fernig DG, Lévy R. Gold nanoparticles as advanced building blocks for nanoscale self-assembled systems. *J Mater Chem*. 2011;21(33):12181. doi:10.1039/c1jm11945a.

70. Guarino G, Rastrelli F, Scrimin P, Mancin F. Lanthanide-based NMR: a tool to investigate component distribution in mixed-monolayer-protected nanoparticles. *J Am Chem Soc*. 2012;134(17):7200–3. doi:10.1021/ja211030y.